The Dissertation Committee for Ye Tian
certifies that this is the approved version of the following dissertation:

Leading Edge Vortex Modeling and its Effect on Propulsor Performance

Committee:

Spyros A. Kinnas, Supervisor

Howard M. Liljestrand

Ben R. Hodges

Hamn-Ching Chen

Venkat Raman

Leading Edge Vortex Modeling and its Effect on Propulsor Performance

by

Ye Tian, B.E., M.E.

DISSERTATION

Presented to the Faculty of the Graduate School of

The University of Texas at Austin

in Partial Fulfillment

of the Requirements

for the Degree of

DOCTOR OF PHILOSOPHY

THE UNIVERSITY OF TEXAS AT AUSTIN

December 2015

Acknowledgments

First of all, I would like to express my sincere appreciation to my supervisor, Professor Spyros A. Kinnas for his guidance and encouragement throughout my graduate studies at the University of Texas at Austin. His endeavor, wisdom, enthusiasm and patience as a teacher and researcher always inspire me to do my best in my research and future career.

I would also like to thank the other committee members: Professor Howard M. Liljestrand, Professor Ben R. Hodges and Professor Venkat Raman from the University of Michigan, Professor Hamn-Ching Chen from Texas A&M University. They reviewed the draft of my dissertation and gave me invaluable comments.

I am very grateful to Dr. Lei He and Dr. Shuhao Chang, for their help and encouragements. I want to give my thanks to the staff and fellows in the Computational Hydrodynamics Laboratory (CHL) and the Offshore Technology Research Center (OTRC) for their precious help and advice. Specially, Ms. Dori Eubank helped me in many administrative processes and saved me tons of time during my preparation of this dissertation. Her support is greatly appreciated. I also enjoyed sharing my life experience and ideas with Mr. Yiran Su, Mr. Hongyang Fan, Mr. Guangyao Wang and Mr. Weikang Du in CHL. It is a memorable experience to work with them.

I collaborated with Mr. Xiangming Yu and Mr. David Menéndez Arán during the first two years of my doctoral study. I still remember the hard working before deadlines of conferences with them. To them, best wishes for the long long journey towards PH.D.

Many thanks are extended to Dr. James Uhlman, for sharing his ideas and experiences with the author.

This work supported by by the U.S. Office of Naval Research (Contract No. N00014-07-1-0616, Contract N00014-10-1-0931 and N00014-14-1-0303) and Phases V, VI and VII of the "Consortium on Cavitation Performance of High Speed Propulsors" with the following members: American Bureau of Shipping, Daewoo Shipbuilding and Marine Engineering Co. Ltd., Kawasaki Heavy Industry Ltd., Rolls-Royce Marine AB, Rolls-Royce Marine AS, Samsung Heavy Industries Co. Ltd., SSPA AB, Andritz Hydro GmbH, Wärtsilä Netherlands B.V., Wärtsilä Norway AS, Wärtsilä Lips Defense S.A.S., and Wärtsilä CME Zhenjiang Propeller Co. Ltd.

Leading Edge Vortex Modeling and its Effect on Propulsor Performance

Publication No. _____

Ye Tian, Ph.D.
The University of Texas at Austin, 2015

Supervisor: Spyros A. Kinnas

A novel numerical method solves the VIScous Vorticity Equation (VISVE) in 3D in order to model the Leading Edge Vortex (LEV) of propellers is proposed and implemented in this dissertation. The spatial concentration of the vorticity is exploited in the method, which is designed to be spatially compact and numerically efficient, in the meantime, capable of modeling complicated vorticity/solid boundary interaction in 2D and 3D. The numerical model can work as a viscous correction on top of the traditional Boundary Element Method (BEM) results.

The proposed method is first applied in the case of a 2D hydrofoil at high angle of attack. The results are correlated with those from Navier-Stokes (N-S) simulation. The method is then used to model the LEV and tip vortex of a 3D swept wing. The results of the 3D simulation show great similarity to

those from NS. In the end, the method is applied in the case of propellers at low advance ratios. All the essential flow characteristics (LEV and tip vortex) are predicted.

The objective of this dissertation is not developing a mathematically equivalent numerical method to the full-blown Reynolds-Averaged Navier-Stokes (RANS) solver, but inventing an accurate and computationally efficient tool to model the effects of the LEV on the propeller performance for engineering's purpose.

Table of Contents

List of Tables

List of Figures

Chapter 1

Introduction

1.1 Background

In recent years, the off-design performance of propellers has drawn more and more attention in the ocean engineering community. However, as a prevailingly used tool on predicting propeller performance, the panel method usually tends to under-estimate the thrust and torque of the propellers at high loading. As the loading increases, the advance ratio becomes smaller, the pitch of the wake sheets becomes smaller. Consequently, the wake shed from one blade could be close to the consequent blade and, thus, strongly affect the pressure distribution on the consequent blade. Tian and Kinnas (2012)[41] developed a full wake alignment model which improves the results from the panel method significantly in the cases of propellers at moderate high loading.

Nonetheless, improved wake model is not a silver bullet on ameliorating the panel method. At very high loading, the predicted thrust and torque from the panel method are still non-negligibly lower than the experimental measurements. At very high loading, a vortex sheet separates from the leading edge region of a propeller blade. This vortex sheet passes over the propeller blade and significantly changes the pressure distribution. The leading edge

vortex (LEV) is connected with the trailing edge wake, forming complicated roll-up geometry. In experiments, the LEV can be visualized by lowering the operating pressure to trigger cavitation, as shown in figure 1.1.

Figure 1.1: Cavitating leading edge vortices emanating from the leading edge of a propeller blade.

1.2 Motivation

Greeley (1982)[10] proposed a LEV model based on the Vortex Lattice Method (VLM). Due to limited computational resources at the time, the model is mainly empirical. Nowadays, even a laptop is much more powerful than the supercomputers in the 80's. It is natural to seek a more rational way to model the LEV other than using empirical formula.

At a glance, there are many similarities between the LEV and the trailing edge free wake, which can be successfully modelled as a distinct shear layer. Thus intuitively we want to directly apply the techniques of modeling the trailing edge wake to model the LEV. Indeed, modeling the LEV as a distinct thin shear layer gained some success in certain cases, such as bi-convex hydrofoils in 2D, and thin delta-wings with sharp leading edge in 3D. But many difficulties, such as finding the detachment point, setting the proper boundary condition at the detachment point, handling the non-smooth velocity close to the solid surface and introducing viscous dissipation, arouse when implementing a LEV model for a general 2D hydrofoil or a 3D propeller blade using the same method for modeling the trailing edge free wake.

In order to overcome the difficulties with the distinct thin shear layer model, a more powerful tool is absolutely necessary.

1.3 Objectives

The objective of the research in this dissertation is to develop an accurate and computationally efficient numerical tool based on the panel method to model the effects of the LEV on the propeller performance for the purpose of engineering.

Reynolds-Averaged Navier-Stokes (RANS) simulation is amenable to model the LEV. However, RANS is considered to be computationally too expensive to be applied in the design stage. For the prediction of propeller performance, the panel method shows great advantages over other numerical

tools. On the one hand, the panel method recovers the real blade geometry as much as possible, instead of simplifying the propeller blades into lifting surfaces as the Vortex Lattice Method (VLM) does. On the other hand, the panel method is much more efficient than RANS simulation, not only in a computational sense, but also on grid generation. Generally panel method strikes a good balance between accuracy and efficiency. Near the design condition, results from the panel method are usually in good agreement with either experimental measurement and or RANS simulation.

Given the fact that the effect of the LEV on the pressure distribution of the propeller blade is significant but also local, *a model which can locally correct the results from the panel method is the goal of this study.*

The model can be semi-empirical, as long as the modeling parameters come with logic and do not scatter from case to case too much. Intensive computation in a local sense is affordable, but in a global sense, the computational cost has to be controlled. The full-blown Reynolds-Averaged Navier-Stokes (RANS) solver is NOT the goal that we are after.

As mentioned in the motivation section, we first modeled the LEV as a distinct thin shear layer and later encountered inevitable numerical difficulties. In order to overcome the difficulties with the distinct thin shear layer model, a spatially distributed LEV model which solves the VIScous Vorticity Equation (VISVE) is proposed and implemented. The spatial concentration of the vorticity is exploited in the VISVE method, which is designed to be spatially compact and numerically efficient, in the meantime, capable of modeling

complicated vorticity/solid boundary interaction in 2D and 3D.

The method is applied in the cases of a 2D hydrofoil at a high angle of attack, a 3D swept wing at a moderate angle of attack, and a model propeller at low advance ratios. In all these cases the VISVE method is able to simulate the formation of the LEV. The predicted vorticity fields for those cases agree reasonably well with the results from Naiver-Stokes (N-S) simulation.

1.4 Overview

This dissertation is organized into five main chapters:

Chapter 1 contains the background, motivation and objectives of this research.

Chapter 2 reviews the existing literature on the LEV modeling, and more generally, the related studies on modeling vortical flows.

Chapter 3 introduces the thin shear layer LEV model and its applications. Although the thin shear layer LEV model eventually does not function well, it still plays an important role to help the author understand the numerical difficulties of modeling the LEV.

Chapter 4 presents the VISVE method in 2D and 3D. This chapter is the most important part in this dissertation. The mathematical formulation and the solving techniques for the 2D VISVE method is first explained. The method is then applied in the case of a 2D hydrofoil at a high angle of attack. The results are correlated with those from a Navier-Stokes solver. After

illustrating the 2D VISVE method, the mathematical formulation, numerical discretization, and solving techniques of the 3D VISVE are systematically presented. The 3D VISVE method is then applied in the cases of a swept wing at inclined inflow and a model propeller at low advance ratios.

Chapter 5 summarizes the conclusions and contributions of this dissertation. Recommendations for future research are also mentioned.

Chapter 2

Literature Review

This chapter reviews the existing literature on the LEV modeling. Literature on general vortex dynamics is also covered selectively.

2.1 Discrete vortex methods in 2D

The success of simulating the unsteady trailing edge wake in 2D through vortex tracing attracted researchers to study the leading edge separated flows using the same method. Katz (1981)[16] applied a discrete vortex method in the case of an airfoil at high angles of attack in order to study the post-stall aerodynamic behavior of the airfoil. The foil was modeled through a 2D vortex lattice approach, and Kutta conditions were imposed at both the trailing edge and also the separation point. Katz suggested that the method could be applied to model foils with round leading edge by multiplying a circulation reduction factor on the strength of shed vortices. The numerical results were largely in good agreement with the experimental data on lifts and drags. The LEV model was turned on and off manually according to the experimental data. At moderate high angles of attack (14DEG $<$ AOA $<$ 20 DEG), the separation point was also chosen to fit the experimental observation.

Spalart and Leonard (1981)[38] presented a more general vortex tracking approach for separated flows. This approach did not have any prescribed separation points. All the vortices created on the solid surface were allowed to enter the fluid domain. The vorticity equation in 2D was then solved in a Lagrangian frame: discrete vortices were traced individually in time, and these vortices form vorticity clouds in the fluid domain. Vortex merging algorithm was designed in order to collapse pairs of close vortices and therefore control the number of unknowns. A second-degree polynomial vortex core was introduced to smooth out the velocity field. Large Reynolds number was assumed, and boundary layer calculation was necessary to create the Reynolds number dependency of the results. The vortex method by Spalart and Leonard (1981)[38] was developed continuously by the second author. Koumoutsakos and Leonard (1995)[18] applied the improved vortex method in the case of an impulsively started cylinder with high-resolution over a wide range of Reynolds numbers (Re=40 to 9500). The viscosity in the improved method was treated more rigorously so that the boundary layer calculation was no long necessary. In the simulations by Koumoutsakos and Leonard (1995)[18], no turbulence model was introduced and thus they classified their study as a Direct Numerical Simulation (DNS) of the Navier-Stokes equations in 2D.

A major emphasis in the past of the discrete vortex methods in 2D was their applications in predicting the vortex induced alternating forces on bluff bodies rather than lifting bodies. For instance, Clements (1973)[4] and Sarpkaya (1975)[36] simulated the inviscid vortex shedding over a square and an

inclined plate respectively. Lewis (1991)[26] summarized different approaches to incorporate viscous effects into the discrete vortex methods, such as random walk and vortex core.

Chorin and Bernard(1973)[3] simulated the roll-up of a 2D vortex sheet. In their simulation, the singular induced velocity due to a discrete vortex was regularized by a smooth function. The follow-up studies carried out by Krasny (1987, 1991)[19][20] showed that the method was simple and powerful for simulating the evolution of 2D vortex sheets. The method using regularized vortex induced velocity, namely the *vortex blob method* was widely applied to model the evolution of free wakes, because of the simplicity of implementation.

A common problem with these discrete vortex methods is that great spatial resolution is usually necessary. In order to have a smooth velocity field, the distance between two discrete vortex has to be smaller than the size of the vortex core. This constrain could be difficult to achieve when extending the methods into 3D.

It is worthwhile to point out that in 2D, the streamfunction-vorticity approach, which solves the vorticity equaiton, is a well-established technique. The method is easy to be implemented and was popular in the past. According to White (2006)[43],it was even used in the first (hand-calculated) CFD solution by Thom (1933)[39]. The method has been seen less in recent years because it is difficult to be extended to 3D. Still it is occasionally used in academia for different purposes, for instance, benchmarking (Erturk et al. 2005)[7].

2.2 LEV and vortex sheet models in 3D

In the 1970s and 1980s, the aerodynamic community devoted great efforts to analyzing delta wings with sharp leading edge at high angles of attack. Kandil et al (1976)[30] proposed a Vortex Lattice Method (VLM) for delta wings with LEV. The LEV geometry was represented by a horseshoe vortex system similar to that of the tailing edge wake. An iterative alignment procedure was applied to adjust the vortex segments in the same direction of the local flow velocity. Gordon and Rom (1985)[9] presented a similar approach for delta wings with a different arrangement of the surface singularities. Both methods led to good correlation with experimental measurements on global forces such as the lift and the pitching moment. Yet the correlations on pressure distribution were not emphasized.

At the same time, a team in the Boeing Company invented a different approach to treat the LEV and also the wake system for wings. The method was summarized by Johnson et al (1980)[15]. In their method, the free LEV/wake sheets were treated as non-penetrating surfaces. A few geometric parameters, such as panel length and roll-up angles were used to describe the LEV and the roll-up part of the wake sheets. After evaluating the pressure jump across the LEV and wake panels, the geometric parameters of the rolling up vortex sheets were adjusted iteratively in order to enforce the force free condition in a least-square sense. A relaxation core panel, namely the 'fed sheet' was introduced in order to terminate the rolling up sheet. Obviously the Boeing's method was based on the velocity type panel method, which

could handle lifting surfaces. In the numerical implementation by Johnson et al.(1980)[15], hyperboloidal dipole and source panels were adopted. With the Boeing's method, reasonable prediction on the pressure distribution on wings can be obtained as well.

However, these methods for delta wings with sharp leading edge more or less suffer from numerical difficulties at low to moderate angles of attack. The smoothness of the induced velocities due to the wing start to deteriorate as the LEV sheet approaches close to the wing. At the same time, the LEV induced velocities on the wing could also be inaccurate. A numerical fence is usually necessary to keep the code from crashing. The Beoing's method using high order singularities might get smooth velocity near the wing, but the way in the method to update the LEV geometry seems to be only suitable for problems with simple flow conditions, such as a delta wing at uniform inflow. Moreover, the method is difficult to be incorporated into any low order potential based panel code. Another problem with these methods is that they are all designed for wings with sharp leading edge, at which a Kutta condition can be applied to determine the strength of the singularities on the LEV sheets. For wings or propeller blades having round leading edge, it is difficult to either find the detachment point, or set up proper boundary conditions at the detachment point.

An early study on propeller tip flow was conducted by Greeley (1982)[10]. In his study, based on the Vortex Lattice Method (VLM), a LEV model combining empirical formula and numerical methods was proposed. The model set

up a LEV sheet suspending over all chord-wise strips having leading edge separation. An empirical equation was introduced to relate the height of the LEV sheet with the thickness of the blade and the boundary layer thickness on the suction side. No iteration was required to determine the LEV geometry. The whole vortex system was solved by applying the kinematic boundary condition on both the mean camber surface of the propeller and the LEV sheet. An implicit Kutta condition was used at the leading edge. This model could predict increased forces on the propeller. Considering the trivial numerical cost, the model is really a practical improvement over the plain VLM. However, this model has little chance to get the correct pressure distribution on the blade because the "following-the-chord" LEV sheet does not include the chord-wise vorticity.

A problem that has not been addressed by the mentioned methods to model the LEV as a distinct sheet layer, is that the pressure were all calculated via the Bernoulli's equation, which is valid for irrotational flow. Considering a point on the wall surface underneath the LEV, it is impossible to find a path connecting this point to a reference point in the irrotational flow region without cutting any vorticity. Thus it is inappropriate to apply the Bernoulli's equation in this case.

Numerical treatment of the 3D trailing edge wake has a close relation to the LEV modeling. Lee et al (2002, 2004)[21][22] developed a 3-D wake model based on a low order panel method for marine propellers. The model was able to predict developed tip vortex cavity, which was treated as a cylin-

drical tube. L. He (2010)[14] extended Lee's wake model in order to take into account some viscous effects. In He's study, different viscous cores were tested. Singh (2009)[37] applied He's algorithm in the case of 2D hydrofoils with LEV separation, and obtained some preliminary results.

2.3 Vortex Methods in 3D

The general topic of vortex methods, or vortex dynamics is related to the LEV modeling. A brief review is given here.

The vorticity in 3D can be modeled using particles, filaments, sheets and volumetric cells. Obviously filaments and sheets have been extensively used in the potential flow methods, such as VLM and BEM, for simulating the flow around lifting bodies. The benefit of using filaments and sheets is that the discrete divergence-free condition of the vorticity field can be represented through the geometric connectivity of the vortex filaments and sheets. The vortex stretching can also be modeled naturally as the geometric change of the filaments or sheets. However, both geometric representations suffer from difficulties when the coherent structure of the flow becomes complicated, especially when contacting and merging happen. Usually re-meshing or point-insertion using spline or Lagrange interpolation is needed as the vortex filaments or sheets evolve, but eventually the number of representing points and the geometric connectivity could become unmanageable and the simulation has to be stopped at a relatively early stage. For example, Lindsay and Krasny (2001) [27] simulated the merging of two inclined vortex rings, the

simulation stopped when the top of the two vortex rings just contacted. In a real flow, the two vortex rings will be connected topologically, whereas in their paper the two rings were still topologically separated, since they were treated as material surfaces. Other examples of using the vortex filaments or sheets can be found in Leonard(1980, 1985)[23][24], Ashurst and Meiburg(1988)[1], Knio and Ghoniem(1990)[17]. These studies were mainly with simplified initial configurations, such as vortex rings/membranes in unbounded domain in favor of theoretical understanding of the early stage of the evolution of a vortex system and the resulting chaotic behavior. Thus the treatment of the vortex filaments and sheets in the proximity to walls were not addressed.

Modelling the vorticity in 3D as particles is counter-intuitive, since a "3D vortex particle" cannot be easily associated with physical significance. However, once the topological connectivity is given up, the evolution of the vorticity field can easily go beyond the early stage. Winckelmans and Leonard (1993)[44] simulated the fusion of two vortex rings using the vortex particle method. In the method the vorticity field was represented by clouds of vortex particles, or so called *vortons*. Each vorton is associated with a position vector and a strength vector. Without bothering book-keeping the connectivity of the particles, the simulation successfully went to the fully merged stage of two vortex rings. Ploumhans et al (2002)[33] greatly extended the method proposed by Winckelmans and Leonard (1993)[44], by including many modern fast solving techniques, such as velocity evaluation using Fast Multipole Method (FMM) with a tree code. The unsteady flow past a sphere at Reynolds

number up to 2000 was simulated.

Most users of the vortex particle methods claim that the methods are mesh-free, but the methods usually use some mesh-like arrangement. For example, in the simulation by Ploumhans et al (2002)[33], the vortons near the wall must be aligned with the surface discretization of the wall. Also the spatial accuracy of the vortex particle methods deteriorates as the distance between two particles grows. Usually re-meshing is required in order to keep the vortons densely distributed in the vortical flow region. Mesh-like structure may also be used in the re-meshing algorithm. A typical idea is that at a certain time step, calculate the vorticity distribution in the flow field, and relocate all vortons at the centers of the background cells. The methods also need a cut-off threshold, in order to remove particles when the vorticity magnitude at certain flow region is too small.

When mesh is used, some researchers solve the VIScous Vorticity Equation (VISVE) using Finite Difference Method (FDM). In order to solve the VISVE, the velocity field must be computed from a given vorticity field. The vector Poisson's equation for the velocity (with a source term $-\nabla \times \boldsymbol{\omega}$) is often used. This category of methods is called vorticity–velocity formulation. The vector Poisson's equation for the velocity was solved by Wu et al (1995)[46] using FDM on a Cartesian grid. Fast Fourier Transform (FFT) was applied to solve the resulting linear algebraic system efficiently. The boundary condition for the Poisson's equation was also discussed. Hansen et al (2003)[13] presented a FDM for solving the VISVE in cylindrical co-ordinates. The vec-

tor Poisson's equation for the velocity, which was an over-determined system in the paper, was solved using least-square method. Because of the cylindrical co-ordinate formulation, only axisymmetric geometric configurations were simulated. Lo et al (2005)[28] proposed a FDM solver for the VISVE. The lid-driven cavity flow was simulated. Artificial compressibility was used to relax the vector Poisson's equation for the velocity. Therefore only steady state solutions were shown. All the mentioned methods with the vorticity-velocity formulation used staggered arrangement of variables.

Alternatively, the stream function in 3D, sometimes called vector potential of the velocity can be used. In order to determine the stream function, a vector Poisson's equation again has to be solved, with boundary conditions containing mixed derivatives. The benefit of this type of methods is that one can construct numerical schemes with collocated arrangement of variables. E and Liu (1997)[5] simulated the lid-driven cavity flow problem with the vorticity–stream function formulation. Collocated grid was used in their calculation. Elshabka and Chung (1999)[6] eliminated the presence of the velocity from the VISVE, and obtained a fourth order time-dependent partial differential equation for the stream function only. Finite Element Method was adopted to solve the equation. Again, the method was applied only in the case of lid-driven cavity flow.

No matter which velocity solver was used, the applications of the VISVE solvers in literature were mainly in simple computational domains, such as rectangular or cylindrical domains. The limited application of those solvers

may be because of the complexity of implementing the boundary condition, which has mixed derivatives.

Chapter 3

Distinct thin shear layer LEV model

3.1 Introduction

There are at least two similarities between LEV and trailing edge wake. First, both LEV and trailing edge wake carry vorticity shed from solid surface. Second, both LEV and trailing edge wake are highly related to strong surface curvature. In the inviscid fluid flow theory, trailing edge wake is the direct outcome of the infinite surface curvature at a sharp trailing edge. The same argument holds for a sharp leading edge — the presence of the LEV at the sharp leading edge leads to finite velocity and pressure. For a round leading edge, the argument of finite velocity and pressure is weakened. However, we can still claim that the foil sections with smaller leading edge radius are more likely to develop LEV, and the LEV brings down the suction peak in pressure distribution. Given the similarities between LEV and trailing edge wake, it is natural to try to model the LEV in the same way as modeling the trailing edge wake. The primary assumption behind this intuitive analogy is that a LEV sheet is a distinct thin shear layer.

3.2 Distinct thin shear layer LEV model in 2D

Before going to 3D, the thin shear layer LEV model in 2D is first discussed here. The 2D investigation is important for the author to understand the capabilities and limitations of the existing numerical tools, as well as the difficulties of modeling LEV.

3.2.1 Formulation of a low order panel method

The formulation of a low order panel method is presented in this section. The method is used to model potential flows around lifting bodies. It is also adopted later in the VIScous Vorticity Equation (VISVE) model to specify the wall boundary condition. More details about the panel method can be found in (Lee et al 2002, 2004)[21][22].

3.2.1.1 Governing Equations

The LEV model is based on a low order panel method. The method gives the vorticity strength on the LEV and also the velocity field due to the presence of the solid wall. We decompose the total velocity into an inflow velocity, which is the velocity in the absence of the body, and a perturbation velocity, which is due to the presence of the body.

$$\mathbf{q} = \mathbf{U}_\infty + \mathbf{u} \tag{3.1}$$

where $\mathbf{q}$ is the total velocity,$\mathbf{U}_\infty$ is the inflow velocity, and $\mathbf{u}$ is the perturbation velocity. The perturbation velocity can be thereby expressed through a

perturbation potential:

$$\mathbf{u} = \nabla\phi \tag{3.2}$$

where ϕ is the perturbation potential. The perturbation velocity field therefore is governed by the Laplace Equation:

$$\nabla^2\phi = 0 \tag{3.3}$$

Applying Green's second identity, the Laplace equation can be written in the following boundary integrated form:

$$2\pi\phi_p = \iint_{S_H}\left[\phi_p\frac{\partial G(p,p')}{\partial n_{p'}} - \frac{\partial\phi_p}{\partial n_{p'}}G(p,p')\right]ds + \iint_{S_V}\phi_V(y_{p'})\frac{\partial G(p,p')}{\partial n_{p'}}ds \tag{3.4}$$

where S_H represents the surface of a hydrofoil or propeller blades and S_V represents the surface of shear layers such as LEV and trailing edge wake. $G(p,p')$ is the Green's function, which is defined as $1/R(p;p')$ in 3D, and $2\ln R(p;p')$ in 2D.

3.2.1.2 Boundary Conditions

Kinematic boundary condition

All solid surfaces are impermeable, therefore the normal velocity has to vanish on the wall, where n denotes the normal vector of a surface.

$$\frac{\partial\phi}{\partial n} = -\mathbf{U}_\infty\cdot\mathbf{n} \tag{3.5}$$

Kutta condition

In the thin shear layer model for LEV and trailing edge wake, the Kutta condition plays a critical role to determine the strength of the shed vorticity, and limit pressure and velocity to be finite. For steady flows, Morino type Kutta condition is widely used. For unsteady flows, the pressure Kutta condition which ensures the smoothness of the pressure field is more general:

$$p_W^+ = p_W^- \tag{3.6}$$

$$p_{LEV}^+ = p_{LEV}^- \tag{3.7}$$

The p_W^+ and p_{LEV}^+ are the pressure at the positive sides of the wake and the LEV; the p_W^- and p_{LEV}^- are the pressure at the negative sides of the wake and the LEV. The positive and negative sides of the wake and the LEV are defined in Figure 3.1: the solid surface clockwise before a wake/LEV sheet is in the positive side, the solid surface clockwise after a wake/LEV sheet is in the negative side. Because pressure is related to velocity through the Bernoulli's equation, the pressure Kutta condition is usually imposed iteratively by solving a system of quadratic equations.

3.2.2 Formulation of the vortex blob method

In the early studies of vortex dynamics, discrete vortices were often used to represent thin vortex layers. The induced velocity due to a discrete vortex with strength Γ can be written as

$$\mathbf{u}_\Gamma = \frac{\Gamma}{2\pi}\frac{\mathbf{r}}{r^2} \times \mathbf{k}, \tag{3.8}$$

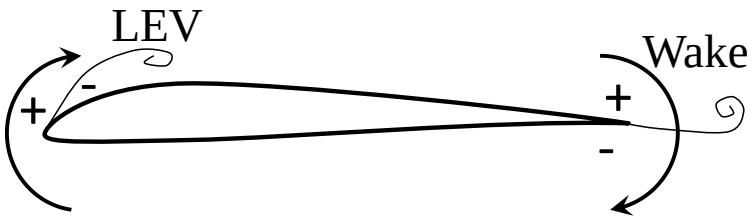

Figure 3.1: Definition of the positive and negative sides of a trailing edge wake or leading edge vortex.

where **r** denotes the vector from the vortex to the field point, and **k** is the unit vector normal to the 2D plane. Clearly the velocity evaluated from (3.8) is unbounded. As the field point approaches the vortex, the induced velocity is singular. In the late stage of the evolution of a shear layer, two discrete vortices could be close to each other. In this case the simulation often crashes because of the unbounded induced velocity. Another problem with the discrete vortex method is that the thin shear layer is intrinsically unstable. The Kelvin-Helmholtz instability can easily develop kinks on the shear layer and eventually lead to chaotic flow patterns. Later on, different vortex cores were introduced by many researchers to improve the numerical stability of the discrete vortex method. Krasny (1987)[19] singled out the Rosenhead-Moore kernel when modelling the roll-up of the trailing edge wake in the Trefftz plane shed from a wing with elliptic loading. The regularized discrete vortex method with a smoothing kernel was given a name the 'vortex blob method'. The vortex blob method is easy to implement and computationally efficient. The regularized

kernel can effectively suppress the Kelvin-Helmholtz instability triggered by numerical discretization, and produce smooth geometry of the shear layer even if the flow pattern is significantly entangled. Due to these merits, the vortex blob method became popular in many 2D applications.

In the vortex blob method using the Rosenhead-Moore kernel, the induced velocity due to a discrete 'vortex blob' is calculated as follows:

$$\mathbf{u}_{\Gamma,\delta} = \frac{\Gamma}{2\pi} \frac{\mathbf{r}}{r^2 + \delta^2} \times \mathbf{k}, \tag{3.9}$$

where δ is the filtering parameter, or the radius of the vortex blob.

In our study, the vortex blob method is adopted to model the distinct thin LEV and the trailing edge wake as well.

3.2.3 Application: a 2D bi-convex hydrofoil at a high angle of attack

In order to avoid the ambiguousness of the boundary condition at the detachment point of the LEV at a round leading edge, a biconvex foil with a sharp leading edge is first investigated. In this case, the detachment point of the LEV is right at the leading edge. A pressure Kutta condition is explicitly applied. This investigation can be seen as a 'panel method version' of Katz (1981)[16]'s study. Several details in the implementation distinguish this investigation from Katz's. Instead of using velocity VLM, a perturbation potential panel method is adopted. On modeling the thin shear layers (LEV and wake), the vortex blob method substitutes the discrete vortex method.

Detailed information of the geometric and numerical configuration is listed in Table 3.1. A simulation using the Finite Volume Method(FVM) for inviscid fluid is also carried out with the same geometry and inflow. On the same grid a Reynolds-Averaged Navier-Stokes (RANS) simulation is performed as well. The settings of the inviscid FVM and the RANS simulations are shown in Table 3.2.

Table 3.1: Geometric and numerical configuration for the biconvex foil with LEV model.

Thickness	t_{max}/c	Time marching	$\Delta t[c/U_\infty]$	δ/c	AOA
parabolic	10%	RK-4	0.000125	3E-4,5E-4	15°

Table 3.2: Settings of the FVM simulations (inviscid/RANS).

Cells	$\Delta t[c/U_\infty]$	Turbulence model	y+
500k, structured	0.000125	SST $k-\omega$	< 5

The results of the numerical simulation of the LEV shed from a biconvex foil have been published in a conference paper (Tian and Kinnas 2011)[40]. Here the author shows the results for the sake of completeness. Figure 3.2 shows the comparison of the LEV geometry at a very early stage predicted by the thin LEV model and the inviscid FVM. A re-paneling scheme is adopted in the LEV model — if the length of a panel is longer than a threshold, a new point will be inserted into the panel using a local cubic Lagrangian interpolation. Clearly, the result from the smaller δ agrees better with the FVM result, but is less smooth than that from the larger δ.

Figure 3.3 shows the corresponding comparisons of the pressure distribution. In most part of the foil, the pressure is not affected by the LEV, the results from the panel method and the inviscid FVM agree extremely well, whereas the LEV does affect the pressure very close to the leading edge. A low pressure spike is formed in the vicinity of the leading edge. The zoom-in views are consistent with Figure 3.2 – better correlation of the location and size of the LEV predicts better correlation of the pressure distribution. It is also worthwhile to point out that both the panel method and the FVM predict stagnation pressure coefficients greater than 1, because of the unsteadiness.

The results at a later stage are also examined. Only the larger δ are used this time. The LEV geometry from the smaller δ is too complex to handle. As shown in Figure 3.4, although the detailed structures of the LEV from thin shear layer model are convoluted, the spatial distributions of the LEV from both methods agree well. The pressure distributions are also reasonably close, as expected. The difference of the magnitude of the C_p may related to the numerical dissipation of the inviscid FVM.

The results from the panel method are correlated with RANS as well. As shown in Figure 3.5, the LEV geometry from $\delta = 0.0005c$ is closer to the RANS prediction than that from $\delta = 0.0003c$. However, although the location of the low pressure peak seems to be predicted correctly, the panel method apparently overestimated the magnitude of $-C_p$.

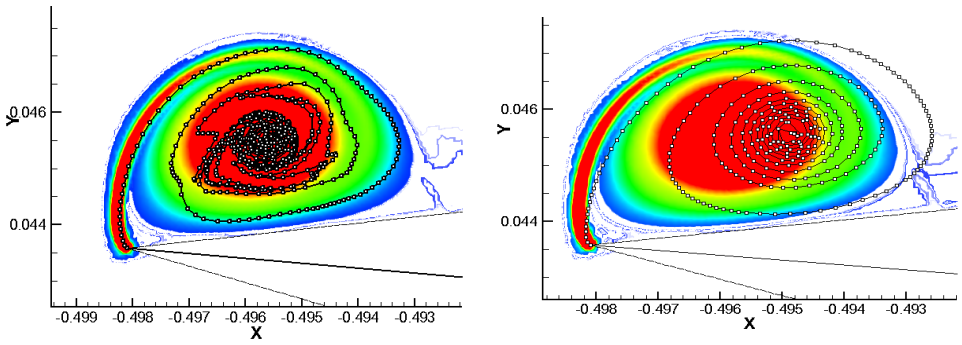

Figure 3.2: Comparisons of the LEV geometry, $t = 0.0125c/U$ (symbols are results from the LEV model; color maps are contours of vorticity magnitude from inviscid FVM; Left: $\delta = 0.0003c$; Right: $\delta = 0.0005c$)

3.2.4 Remarks

The results from the distinct thin shear layer LEV model on a biconvex foil seem to be encouraging. We at least could predict the inviscid behavior of the LEV shed from a sharp leading edge to a certain degree of accuracy. The predicted pressure distributions are also reasonable. However, several facts prevent the model being practically useful.

First of all, the spatial and temporal resolutions in this investigation are very fine. This is the reason that very small $\delta(0.0003, 0.0005)$ can be used. The rule of thumb to select the value of δ is that δ has to be in the same order of the spatial discretization so that the resulting flow field is smooth. Such fine resolutions can hardly be achieved in 3D applications.

Second, the correlation with RANS is only reasonable at the inception stage of the LEV. In RANS, the separated vorticity cloud is gradually stretched

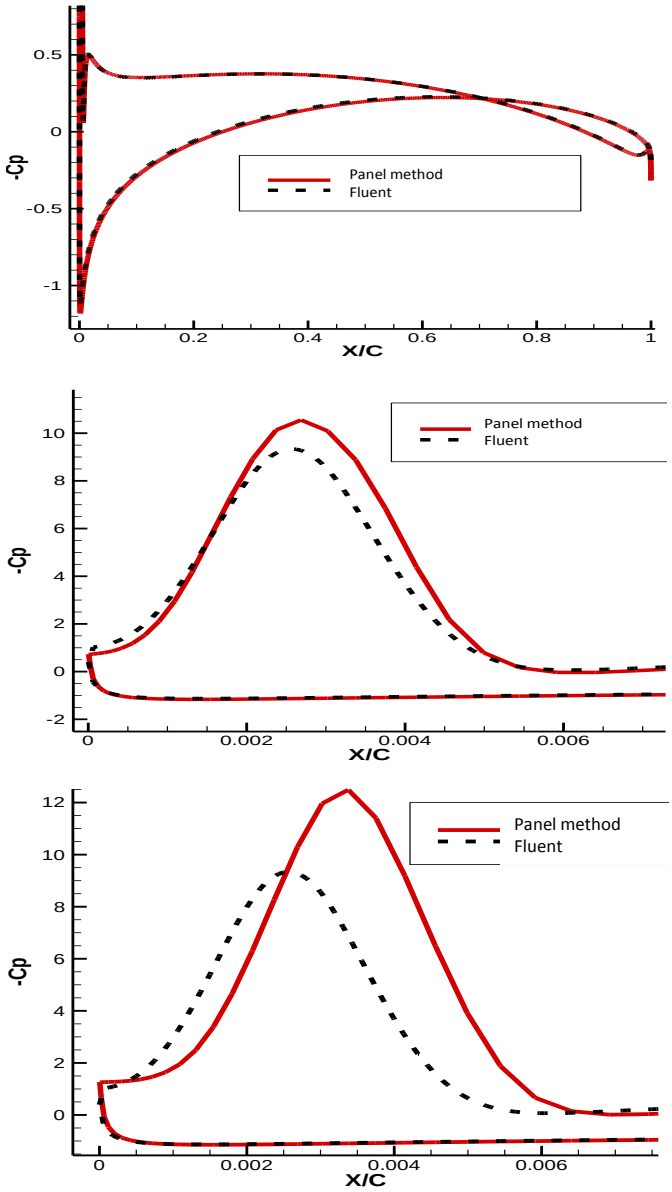

Figure 3.3: Comparisons of the pressure distribution, $t = 0.0125c/U$ (Top: the overall distribution; middle and bottom: a zoom-in view close to the leading edge. middel: $\delta = 0.0003c$, bottom: $\delta = 0.0005c$)

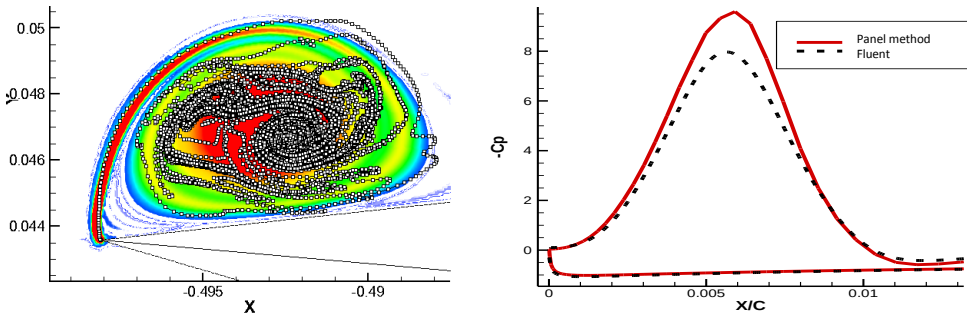

Figure 3.4: Comparisons of the LEV geometry and the corresponding pressure distribution, $t = 0.04c/U$, $\delta = 0.0005c$ (symbols are results from current schemes; color maps are contours of vorticity magnitude from inviscid FVM).

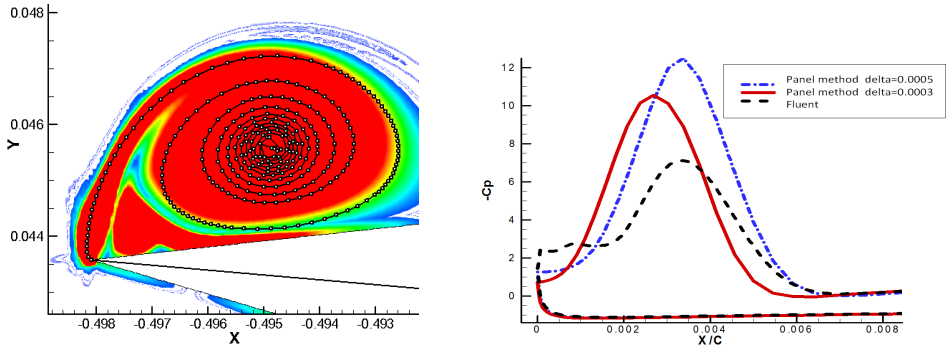

Figure 3.5: Comparisons of the LEV geometry and the corresponding pressure distribution, $t = 0.0125c/U$, $\delta = 0.0005c$ (symbols are results from current schemes; color maps are contours of vorticity magnitude from RANS).

in the stream-wise direction and squeezed in the normal direction of the wall. Eventually the separated vorticity cloud is concentrated in a thin and long, crescent region above the wall. We are far more interested in the stabilized LEV than just the inception stage, unfortunately the thin LEV model does not have the necessary physical fidelity to capture the fully developed LEV.

Most likely a round thick stationary separation bubble as shown in figures 3.2 to 3.5 will be the best result that we can expect from the thin LEV model.

Moreover, the thin LEV model is principally through a Lagrangian point of view. Therefore, the steady state cannot be well defined. Due to the lack of dissipation, energy carried by vortices keeps entering and accumulating in the rolling-up region. The unbound energy finally makes the model blow up. However, in three dimensions, a steady state of the rolled up LEV can be well defined, because there is an additional dimension allowing convection. The existence of the 3D steady LEV is the driven force for us to extend the thin LEV model into 3D despite the problems that we encounter in 2D.

Efforts are also taken to apply the thin LEV model in the cases of hydrofoils with round leading edges, but the results are less successful than those from the biconvex foil. The pressure Kutta condition does not work well in this case. The room for the LEV to roll up is much smaller than that of the biconvex foil due to the strong surface curvature. The visualization from RANS also indicates that the LEV shed from a round leading edge is less distinct than that from a sharp leading edge. More on modeling the LEV shed from a round leading edge will be discussed later.

3.3 Distinct thin shear layer LEV model in 3D

In this section, we are trying to extend the 2D distinct thin shear layer LEV model into 3D. Although this attempt is unfortunately not successful, it does give insight into the appropriate method to deal with the LEV.

3.3.1 Formulation of a low order panel method in 3D

The formulation of the low order panel method in 2D is also applicable in 3D. We reiterate the equation here.

$$2\pi\phi_p = \iint_{S_H} \left[\phi_p \frac{\partial G(p,p')}{\partial n_{p'}} - \frac{\partial \phi_p}{\partial n_{p'}} G(p,p')\right] ds + \iint_{S_V} \phi_V(y_{p'}) \frac{\partial G(p,p')}{\partial n_{p'}} ds \tag{3.10}$$

where S_H represents the surface of hydrofoils or propeller blades and S_V represents the surface of the shear layers such as the LEV and the trailing edge wake. $G(p,p')$ is the Green's function, which is defined as $1/R(p;p')$ in 3D. The boundary conditions in 3D are the same as those in 2D.

3.3.2 3D extension of the vortex blob method

In 3D, a vortex sheet is discretized into constant dipole elements, which are equivalent to vortex loops with constant vorticity strength. Induced velocity due to the vortex loop can be evaluated using the Biot-Savart law:

$$\mathbf{u} = -\frac{1}{4\pi} \iint \phi \nabla \left(\frac{\partial 1/R}{\partial n}\right) ds = \frac{1}{4\pi} \int \phi d\mathbf{l} \times \frac{\mathbf{R}}{R^3}. \tag{3.11}$$

Replacing the Biot-Savart kernel $\mathbf{R}/R^3$, with the Rosenhead-Moore kernel $\mathbf{R}/(R^2+\delta^2)^{3/2}$, leads to the 3D extension of the vortex blob method. Studies by Ramsey (1996)[35], He(2011)[14], and Lindsay and Krasny (2004)[27] showed that this method could give reasonable prediction of the 3D evolution of vortex sheets.

3.3.3 A pseudo-unsteady alignment scheme for 3D free shear layers

Free vortex sheets are material surfaces. When the distinct thin shear layer model is applied, the connectivity among the representing points on the vortex sheets has to be maintained. In many cases, steady state of the LEV and the trailing edge wake shed from a wing or a propeller blade can be defined under a proper frame of reference. In the steady state, the free vortex sheets have to be aligned with the local flow velocity. Therefore, *wake alignment* is often referred to as the procedure to determine the geometry of free vortex sheets, either in a steady or an unsteady sense.

The steady wake alignment problem historically more interested the engineering community. Analogously to the Euler-explicit scheme in unsteady cases, many researchers align a vortex sheet using the velocity at the upstream nodal points:

$$x_{i+1} = x_i + \Delta x, \tag{3.12}$$

$$y_{i+1} = y_i + \frac{q_{y,i}}{q_{x,i}}\Delta x, \tag{3.13}$$

$$z_{i+1} = z_i + \frac{q_{z,i}}{q_{x,i}}\Delta x. \tag{3.14}$$

Numerical tests show that this scheme is stable and converges fast. However, it has the same deficiency as the Euler-explicit scheme for the unsteady alignment: the scheme continuously enlarges the radius of the rolling-up region of the vortex sheet, and thus cannot predict the correct location and size of the rolling-up region. In order to better predict of the wake geometry,

an alignment scheme using the trapezoidal rule is preferred. However, direct application of the trapezoidal rule turned out to be unstable.

Tian and Kinnas (2011)[40] proposed a pseudo-unsteady alignment approach when simulating the LEV for delta wings with sharp leading edges. This alignment approach is also extended in the case of modeling the trailing edge wake of a propeller blade (Tian and Kinnas 2012)[41].

Consider a material line defined as follows:

$$y = y(x,t). \tag{3.15}$$

We have

$$q_y = \frac{\mathbf{D}y}{\mathbf{D}t} = \frac{\partial y}{\partial t} + q_x \frac{\partial y}{\partial x} \tag{3.16}$$

which leads to

$$\frac{\partial y}{\partial t} = q_y - q_x \frac{\partial y}{\partial x}. \tag{3.17}$$

Discretizing (3.17) with the central difference scheme for the slope and with the Euler-Explicit scheme for the unsteady term, we have:

$$\begin{aligned} y_i^{n+1} &= y_i^n + \Delta t/2 \left[(q_{y,i-1}^n + q_{y,i}^n) - (q_{x,i-1}^n + q_{x,i}^n) \frac{y_i^n - y_{i-1}^n}{x_i^n - x_{i-1}^n} \right] \\ &= y_i^n + \Delta t \left[\hat{q}_{y,i} - \hat{q}_{x,i} \frac{y_i^n - y_{i-1}^n}{x_i^n - x_{i-1}^n} \right] \\ &= \left(\frac{\Delta t}{\Delta x_i} \hat{q}_{x,i} \right) \frac{\hat{q}_{y,i} \Delta x_i}{\hat{q}_{x,i}} + \left(1 - \hat{q}_{x,i} \frac{\Delta t}{\Delta x_i} \right) y_i^n + \hat{q}_{x,i} \frac{\Delta t}{\Delta x_i} y_{i-1}^n \end{aligned} \tag{3.18}$$

where $\hat{q}_{y,i} = (q_{y,i-1}^n + q_{y,i}^n)/2, \hat{q}_{x,i} = (q_{x,i-1}^n + q_{x,i}^n)/2$, and $\Delta x_i = x_i^n - x_{i-1}^n$.

Denoting $\Delta t_i^* = \Delta x_i / \hat{q}_{x,i}$, and $\beta = \Delta t / \Delta t_i^*$, we have

$$\begin{aligned} y_i^{n+1} &= \hat{q}_{y,i}\Delta t + \left(1 - \frac{\Delta t}{\Delta t_i^*}\right) y_i^n + \frac{\Delta t}{\Delta t_i^*} y_{i-1}^n \\ &= \beta \hat{q}_{y,i}\Delta t_i^* + (1-\beta)\, y_i^n + \beta y_{i-1}^n, \\ z_i^{n+1} &= \hat{q}_{z,i}\Delta t + \left(1 - \frac{\Delta t}{\Delta t_i^*}\right) z_i^n + \frac{\Delta t}{\Delta t_i^*} z_{i-1}^n \\ &= \beta \hat{q}_{z,i}\Delta t_i^* + (1-\beta)\, z_i^n + \beta z_{i-1}^n. \end{aligned} \tag{3.19}$$

Notice that (3.19) is the alignment scheme for vortex sheets under horizontally uniform inflow. In other words, the inflow is parallel to the x-axis. The idea behind this approach is that the fixed coordinate has to be in the same direction of the dominant inflow, therefore, (3.19) behaves in an upwind manner numerically. For example, the slope of the curve at current point is evaluated using current point and the upstream point. However, in the case of the flow around a propeller, the dominant inflow will not be in the axial direction, but along helices with constant pitch. The rotational component of the inflow is important. Therefore, the scheme described in (3.19) has to be modified when simulating the propeller wake. The essence of the alignment scheme described above is to decompose the total velocity vector into two components: (1) a component parallel to the inflow and (2) a component normal to the inflow; then keep the length of the vortex segment in the inflow direction unchanged.

Consider a point under cylindrical coordinate $x_{i-1}, r_{r-1}, \theta_{i-1}$, with $\Delta\theta$ being the grid size parameter in the stream-wise direction. If the wake is only aligned with the inflow, the consequent point will be at $x_i = x_{i-1} + RJ_s\Delta\theta/\pi$;

$r_i = r_{i-1}$ and $\theta_i = \theta_{i-1} + \Delta\theta$. Therefore, the effective inflow direction in the Cartesian system on the segment connecting the $(i-1)$th and the ith points is

$$\mathbf{s}_i = \frac{\Delta\mathbf{s}_i}{|\Delta\mathbf{s}_i|} \tag{3.20}$$

where in Cartesian system $\Delta\mathbf{s}_i$ is defined as

$$\Delta\mathbf{s}_i = \begin{pmatrix} RJ_s\frac{\Delta\theta}{\pi} \\ r_i\cos\theta_i - r_{i-1}\cos\theta_{i-1} \\ r_i\sin\theta_i - r_{i-1}\sin\theta_{i-1} \end{pmatrix}. \tag{3.21}$$

Now the averaged perturbation velocity $\hat{\mathbf{u}}_i = (\mathbf{u}_i + \mathbf{u}_{i+1})/2$ can be decomposed into two components:

$$\hat{u}_{i,s} = \hat{\mathbf{u}}_i \cdot \mathbf{s}_i \tag{3.22}$$

$$\hat{\mathbf{u}}_{i,n} = \hat{\mathbf{u}}_i - \hat{u}_{i,s}\mathbf{s}_i \tag{3.23}$$

where $\hat{u}_{i,s}$ is the scalar projection of $\hat{\mathbf{u}}_i$ in Cartesian system onto $\mathbf{s}_i$, and $\hat{\mathbf{u}}_{i,n}$ is the vector component of $\hat{\mathbf{u}}_i$ normal to $\mathbf{s}_i$.

Defining $\Delta t_i^* = |\Delta\mathbf{s}_i|/(\hat{u}_{i,s}\Delta\theta/\omega_{prop} + |\Delta\mathbf{s}_i|)$, and $\beta = \Delta t/\Delta t_i^*$. we obtain the alignment scheme for the wake of propeller propeller blades:

$$\begin{aligned} \mathbf{x}_i^{n+1} &= \hat{\mathbf{u}}_{i,n}\Delta t + \left(1 - \frac{\Delta t}{\Delta t_i^*}\right)\mathbf{x}_i^n + \frac{\Delta t}{\Delta t_i^*}(\mathbf{x}_{i-1}^n + \Delta\mathbf{s}_i) \\ &= \beta\hat{\mathbf{u}}_{i,n}\Delta t_i^* + (1-\beta)\mathbf{x}_i^n + \beta(\mathbf{x}_{i-1}^n + \Delta\mathbf{s}_i) \end{aligned} \tag{3.24}$$

where $\mathbf{x}_i^n$ denotes the coordinates of the ith point at nth time step. It is easy to show that if the projection of the vector $\mathbf{x}_i^n - \mathbf{x}_{i-1}^n$ on $\mathbf{s}_i$ is $|\Delta\mathbf{s}_i|$, the projection of the vector $\mathbf{x}_i^{n+1} - \mathbf{x}_{i-1}^n$ on $\mathbf{s}_i$ is $|\Delta\mathbf{s}_i|$ as well. Equation (3.24) is implemented in the full wake alignment (FWA) model for propellers by Tian and Kinnas (2012)[41].

3.3.4 Application: delta wings with sharp leading edges

Delta wings are well-known for their strong LEV effects. In order to test the model, a delta wing with parabolic thickness distribution is investigated. Same as in the 2D biconvex foil case, maximum thickness is set to be 10% of the chord length at each section. The aspect ratio of this delta wing is 1. The inflow AOA is 15 degrees.

Both the Euler-Explicit like scheme and the pseudo-unsteady scheme are applied. RANS simulation with $k-\omega$ SST turbulent model is also carried out with commercial software Fluent. The RANS case using 5 million cells took 10 hours to converge, with 32 Intel Xeon 2.54GHz CPUs. The wall y^+s are mainly controlled in the range between 30 and 80.

Figure 3.6 shows the LEV geometries predicted from both Euler-Explicit like scheme and pseudo-unsteady scheme. The corresponding streamlines from RANS is also plotted. Obviously, the pseudo-unsteady scheme correlated better with the RANS result than with the Euler-Explicit like scheme.

Figure 3.7 compares the LEV geometries predicted from the pseudo-unsteady scheme with the experimental observation. In this case, the flow around a thin delta wing with a 15° semi-vertex angle at 20° AOA is simulated. The results agree well with the experimental observation, as shown in Figure 3.7, after Van Dyke's *An Album of Fluid Motion*, Fig. 90[42].

Two span-wise cross-sections are taken to make detailed comparisons for the cases shown in Figure 3.6(x/c=-1.5, -0.5). As shown in Figure 3.8 and

3.9, although the Euler-Explicit like scheme predicts a smoother LEV geometry than the pseudo-unsteady scheme, the latter has better correlation with the pressure distribution from RANS. The location of the low pressure peak seems to be captured by the latter; however, the magnitude is still overshot.

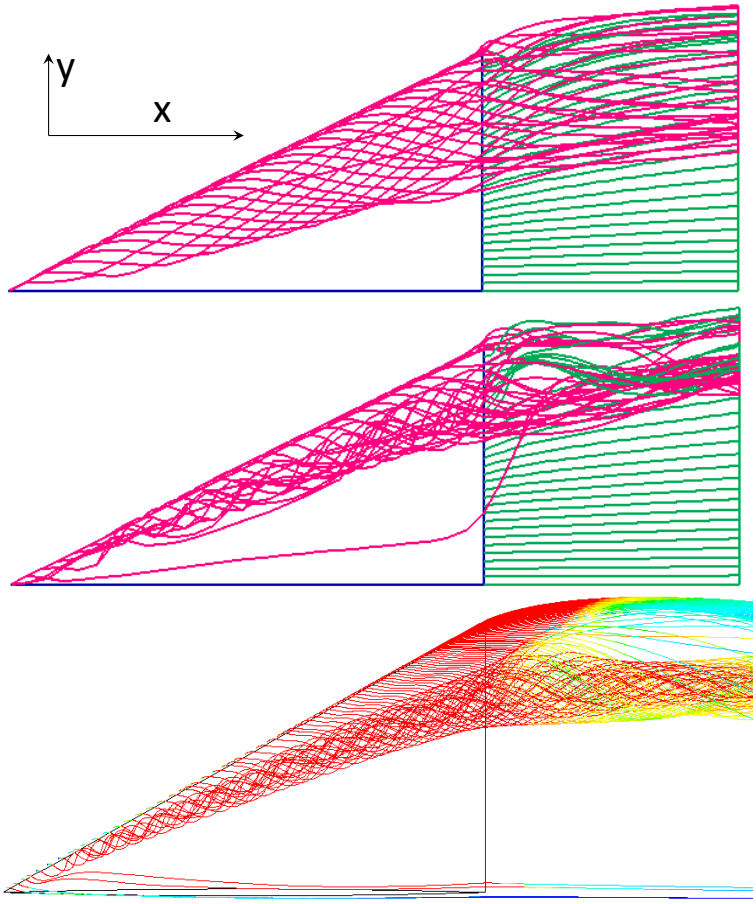

Figure 3.6: LEV geometry of the delta wing at 15° AOA(Top:Euler-Explicit like scheme; Middle: pseudo-unsteady scheme; Bottom: RANS streamlines released from leading edge.)

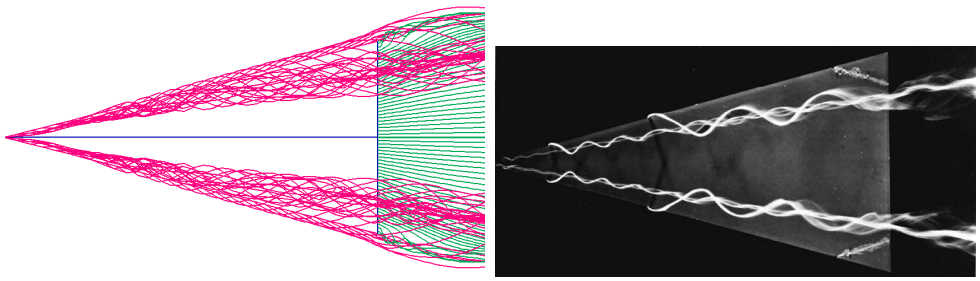

Figure 3.7: LEV geometry of a thin delta wing of 15° semi-vertex angle at 20° AOA(Top: pseudo-unsteady scheme; Bottom: corresponding experimental picture, after (Van Dyke 1982), Figure 90[42])

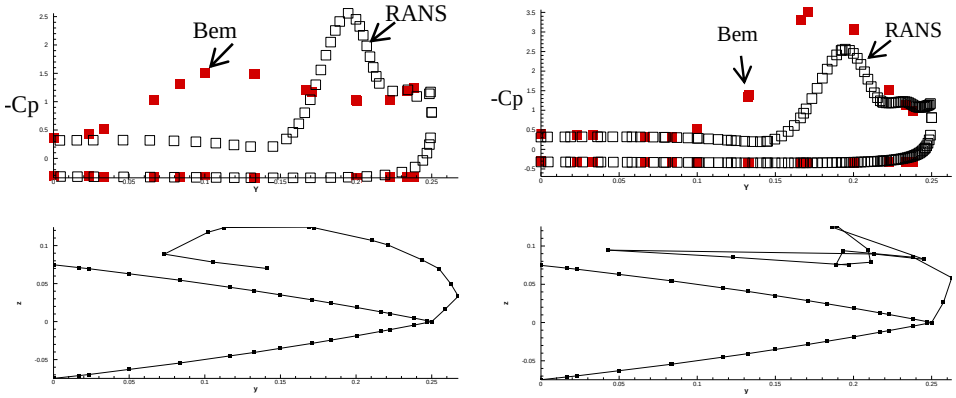

Figure 3.8: Comparisons of the pressure distribution on a delta wing at 15° AOA with RANS, $x/c = -1.5$ (Left:Euler-Expilict like scheme; Right: pseudo-unsteady scheme.)

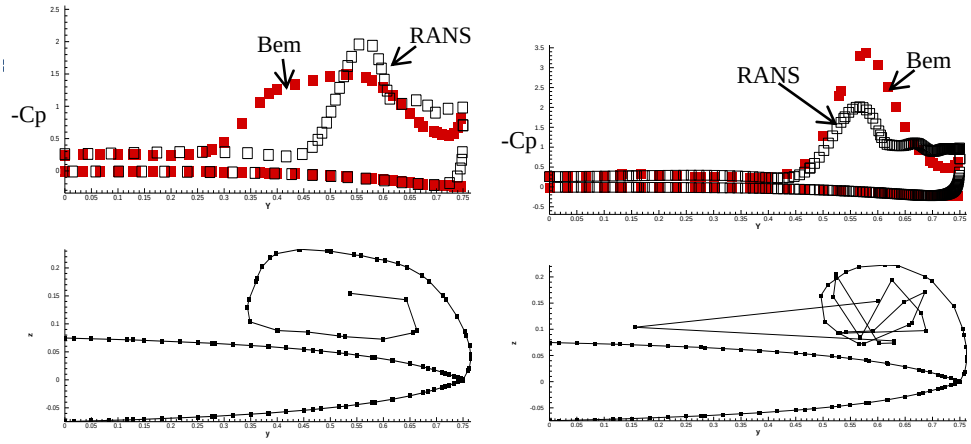

Figure 3.9: Comparisons of the pressure distribution on a delta wing at 15° AOA with RANS, $x/c = -0.5$ (Left:Euler-Explicit like scheme; Right: pseudo-unsteady scheme.)

3.3.5 Application: a propeller

A low order panel code, PROPCAV, is applied to model a five-bladed propeller DTNSR 4381, which is investigated by Boswell (1971)[2] through experimental measurement. The design advance ratio $J_s = V_s/nD$ of this propeller is 0.889, where V_s is the ship speed, n is the rotational speed of the propeller in revolution per second, and D is the diameter of the propeller.

For the simulations with the panel method, two wake models are adopted: PSF-2 wake model, which is a fast wake alignment scheme developed by Greeley and Kerwin (1987)[11], and a full wake alignment (FWA) scheme, which is implemented in this study. For all the advance ratios, wakes of one revolution are modeled with the FWA scheme. For the PSF-2 model, wakes are trimmed at 2.5 R downstream with an ultimate wake disk. The hub of this propeller is also modeled through BEM panels, but the hub vortex core is omitted in this study.

RANS simulations of the same propeller are carried out with commercial RANS solver FLUENT, for $J_s = 0.883, 0.6, 0.5$ and 0.4. k-ω SST turbulence model is adopted. QUICK scheme is used for spatial discretization, and SIMPLEC scheme is applied for pressure correction. 1.5 million hexahedral cells are used to simulate one sector of the domain with periodic boundary condition. It took 12 to 14 hours on 32 Intel Xeon 2.54GHz CPUs for the residuals to converge to 1E-6.

In the experimental study by Boswell (1971)[2], only integrated forces

were measured. Figure 3.10 compares the integrated forces predicted by PROPCAV and RANS, and the experimental measurements. We can see that the predicted KTs from PROPCAV with either wake model agree the well with both experimental data and RANS near design J_s. However, as the advance ratio becomes smaller, the KT predicted by PROPCAV using the PSF-2 alignment starts deviating from the experimental data and the RANS results. In the meantime, the KT from fully aligned wake model is still in close agreement with the experimental data. PROPCAV with either wake model tends to slightly overestimate the KQ near the design condition, but the results from PROPCAV with PSF-2 alignment deteriorate at low advance ratios.

Figure 3.11 shows the aligned wake geometry at two different advance ratios ($J_s = 0.889$ and $J_s = 0.5$). Clearly at low advance ratio, the wake sheets are strongly rolled up. Figure 3.12 shows sections of the aligned wake cut at the $z = 0$ plane, for different J_s with different spatial discretization on the blade, where propeller frame of reference is defined as: x is along the axial direction, y is along the radial direction passing the middle of the root of the key blade, and z is normal to x and y directions. The roll up of the tip vortex can be observed.

More detailed comparisons of the results between PROPCAV and RANS are performed in two different blade sections at two different advance ratios, as shown in Figure 3.13 and 3.14. The correlations among different numerical methods are remarkably good. Results from PROPCAV with fully aligned wake model are closer to that of RANS, comparing with the PSF-2 wake mod-

el. This is consistent with the results for the total forces. Also for the FWA model, different spatial grids yield almost coincident results.

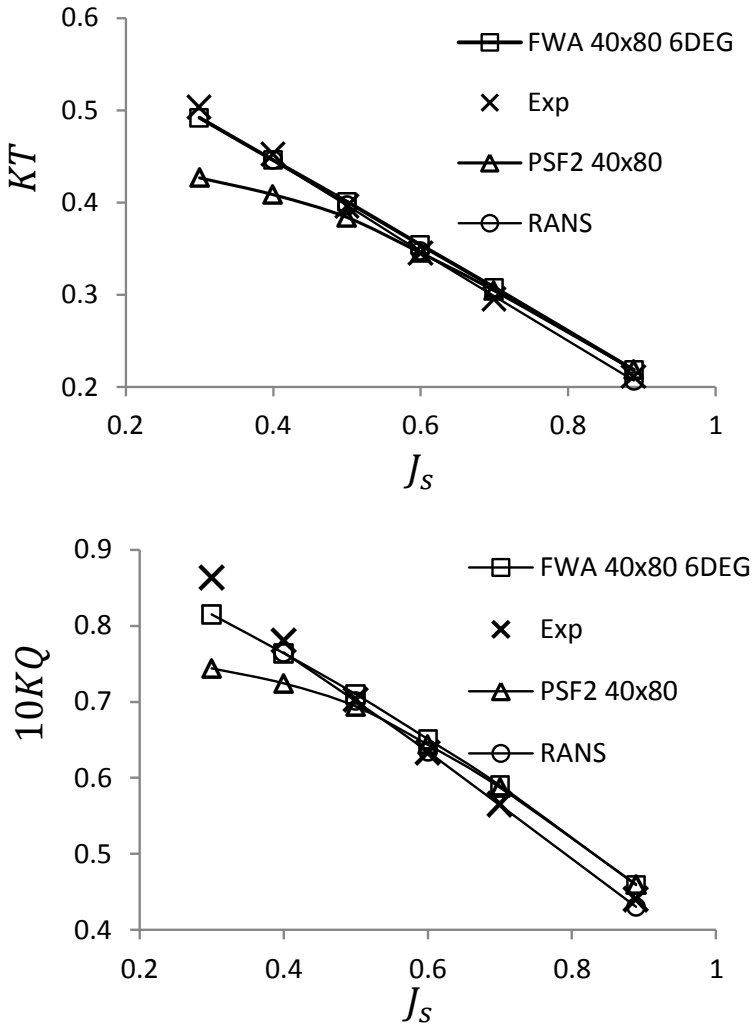

Figure 3.10: KT and 10KQ for propeller DTNSR 4381 from PROPCAV. Experimental data are extracted from (Boswell 1971)[2]. PSF-2 alignment is according to Greeley and Kerwin (1982)[11].

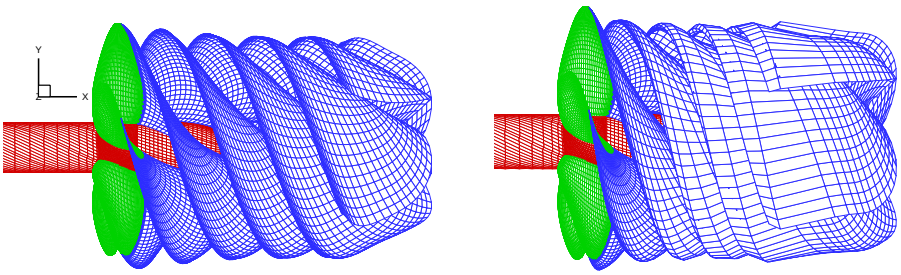

Figure 3.11: Wake geometry of the propeller DTNSR 4381 from FWA at different advance ratios. (Left: $J_s = 0.889$; Right: $J_s = 0.5$)

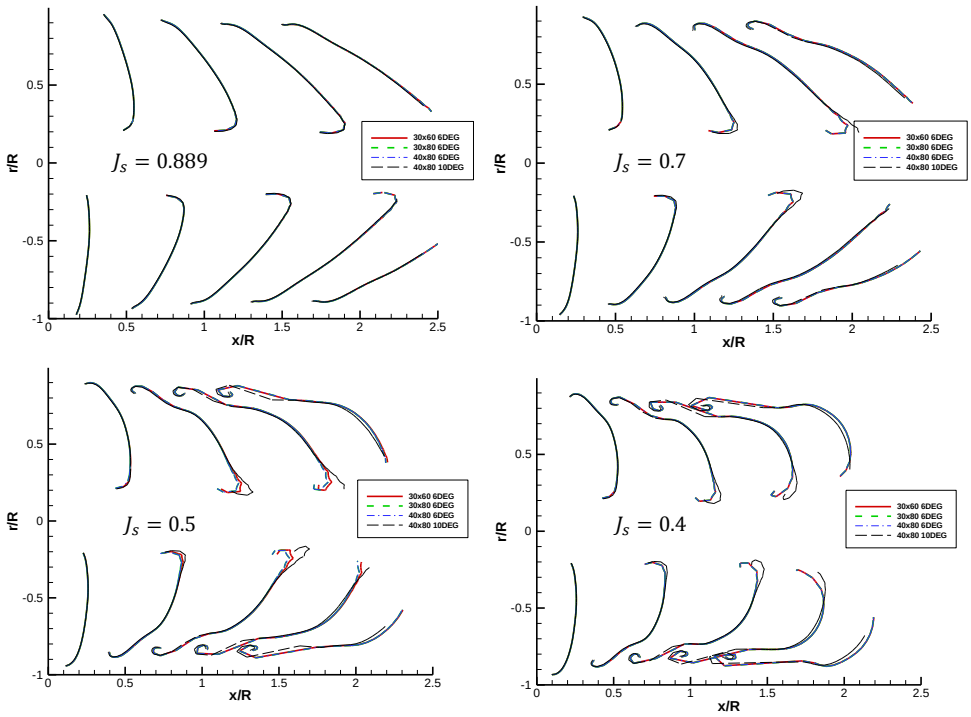

Figure 3.12: Sections on the aligned wake cut at $z = 0$ plane at different J_s with different discretization on the blade.

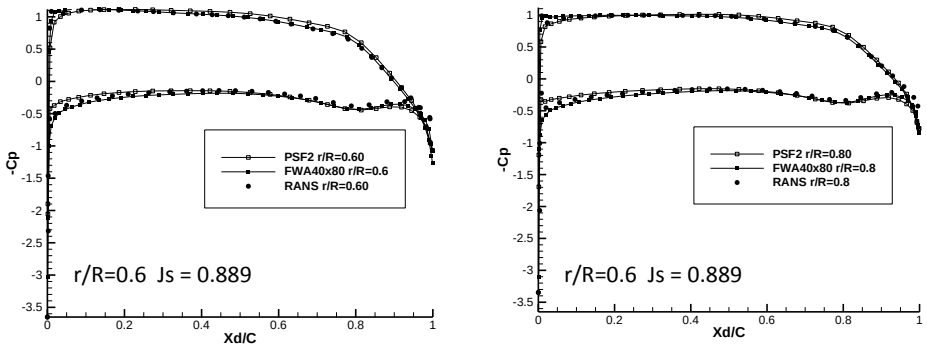

Figure 3.13: Comparison of pressure from different numerical methods at $J_s = 0.889$ of Propeller 4381, where $C_p = (p - p_0)/(\rho/2n^2D^2)$

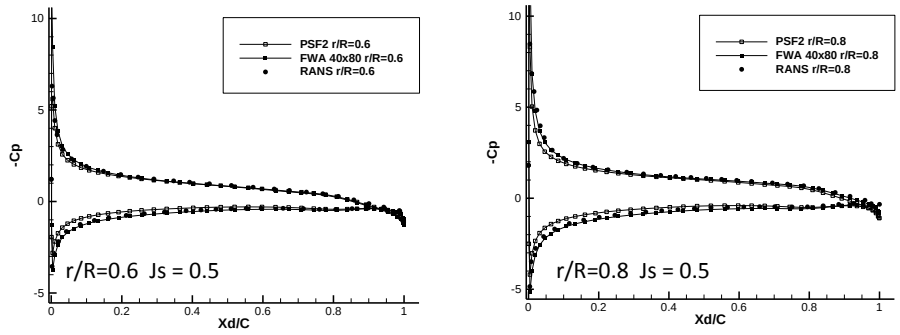

Figure 3.14: Comparison of pressure from different numerical methods at $J_s = 0.5$ of Propeller 4381, where $C_p = (p - p_0)/(\rho/2n^2D^2)$

Further application of the LEV model onto the current results, however, is not considered to be successful. The spatial discretization of the surface panels on the blade cannot resolve the roll-up region of the LEV, and thick numerical fence has to be applied in order to screen the abnormal velocities close to the wall. Consequently, the LEV sheet just do not roll up at all. The integrated forces do increase as expected, but the circulation seems to be affected too much. Comparisons with RANS on the pressure distribution also suggest that we have not captured the correct location of the low pressure plateau.

3.3.6 Remarks

The distinct vortex sheet model gains success on modeling the trailing edge wake. For modeling the propeller wake, the FWA scheme can help the panel method predict forces of a highly loaded propeller reasonably well. For propeller DTNSR 4381, the results predicted by PROPCAV with the FWA model are acceptable even when J_s is as low as 0.4. However, in order to analyze the propeller working at lower advance ratios, a LEV model is a must.

Unfortunately, the distinct vortex sheet model only works in a few cases for modeling the LEV. In 3D applications, the spatial resolution is often insufficient to resolve even the most basic flow pattern of the LEV. With this consideration, the author believes that a LEV model using spatially averaged variables could be less sensitive to the spatial resolution. This idea leads to the development of the distributed LEV model.

Chapter 4

VIScous Vorticity Equation (VISVE) model

As mentioned in the last chapter, the distinct LEV model performs well for the trailing edge wakes shed from propeller blades and the LEV shed from delta wings having sharp leading edge at high AOA. However, the distinct LEV model suffers from difficulties at moderate AOA and at round leading edges. In order to overcome these difficulties, a distributed LEV model is proposed.

4.1 Problems with the distinct LEV model

In the application of the distinct LEV model, two major difficulties are encountered: 1) detachment conditions; 2) wall effects.

The detachment conditions for the LEV and the trailing edge wake are different. Following the inviscid flow theory, the trailing edge wake with a Kutta condition only makes sense for a sharp trailing edge. Attaching the distinct wake sheet with a Kutta condition directly onto a round trailing edge usually leads to oscillating pressure distribution near the trailing edge. Pan and Kinnas (2011)[31] suggested that in order to apply the distinct wake model, the round trailing edge has to be extended to a sharp one with certain criteria. For the LEV, the sharp leading edge rarely appears in practical applications.

Thus the same argument is legitimate — the Kutta condition is not the proper boundary condition for the LEV shed from a round leading edge. In fact the detachment of the LEV from a round leading edge cannot be described by a simple condition only at the point where the surface flow changes direction. At least the surface patch with a length scale in the same order of the leading edge radius is closely related to the detachment.

The LEV also strongly interacts with the wall, as opposed to the trailing edge wake which is almost free from the influence of the wall. An inevitable problem for any LEV model is that the shed LEV could re-touch the wall. However, it is known that close to the wall, the velocity field evaluated from a low order panel method is very inaccurate. Practically a 'numerical fence' is usually imposed on the wall. If any representing point of the LEV goes too close to the wall, the point is pushed away from the wall with a prescribed clearance. In order to have smooth velocities, the clearance is commonly set as the characteristic length of the surface panels. Using high order formula to evaluate the wall induced velocity could improve the smoothness of the flow field, but it is difficult to implement in 3D. Obviously the 'numerical fence' is non-physical. Particular in 3D, due to the limited spatial resolution, quite often the characteristic length of the surface panels could be larger than the height of the LEV, therefore the roll-up of the LEV could be artificially suppressed.

Besides the two major difficulties discussed above, other issues such as how to evaluate the pressure (Bernoulli's equation could not be applid when

the wall is covered by a cloud of vorticity.) and how to determine the spanwise detachment point in 3D , also bug the distinct LEV model. We are not saying that the distinct LEV model totally fails. In fact the results from unsteady inviscid FVM simulation on a certain hydrofoil support a LEV model starting with a distinct thin layer and ending with a huge crescent vortex core (The RANS results, however, are in a favor of a distributed LEV model, even though considerable concentration of the vorticity in a narrow region can be observed). It is possible that we can design a better distinct LEV model in the future, but at this stage we switch to a distributed LEV model which helps us to overcome the difficulties with the distinct LEV model.

4.2 VIScous Vorticity Equation LEV model

The idea of the distributed LEV model is that instead of having a prescribed detachment point, every point on the wall can release vorticity into the flow field. Whether and how much vorticity enter the flow field from a surface panel are determined by the flow condition. This should resolve the problem of the detachment condition.

Without tracing the vortex sheet in a Lagrangian frame, the VIScous Vorticity Equation (VISVE) has to be solved in an Eulerian grid. The VISVE for incompressible flow is often written as:

$$\frac{\partial \boldsymbol{\omega}}{\partial t} + (\mathbf{q} \cdot \nabla)\boldsymbol{\omega} - (\boldsymbol{\omega} \cdot \nabla)\mathbf{q} = \nu \nabla^2 \boldsymbol{\omega} \tag{4.1}$$

where $\boldsymbol{\omega}$ is the vorticity vector, and the $\mathbf{q}$ is the velocity vector.

The Eulerian grid for solving (4.1) can be concentrated in the proximity to the leading edge, and thus a local solution of the vorticity distribution is sought. A panel method provides the boundary condition to the vorticity equation. The Eulerian grid ensures the smoothness of the velocity field near the wall, therefore the strong interaction between the LEV and the wall can be handled. Switching from a grid-free method to one uses a spatial grid, the model starts to assimilate to a Navier-Stokes (N-S) solver which uses grids as well. The N-S equation may even be easier to solve than the VISVE — at least the solving techniques of the former are pretty mature after being investigated extensively for decades. In the meantime, we rarely see applications of the vorticity equation in 3D. A few attempts on solving the vorticity equation (see Wu et al (1995)[46], Hansen et al (2003)[13], Lo et al (2005)[28], E and Liu (1997)[5] and Elshabka and Chung (1999)[6]) are merely limited in academia. The driven force for us to develop a VISVE solver is the spatial concentration property of vorticity.

4.2.1 Spatial concentration of vorticity

As mentioned before, the development of a VISVE solver in 3D could be challenging. The main reason that we follow the VISVE approach is the spatial concentration of vorticity. Vorticity in either attached or separated flow is often concentrated in a small region near the wall. This assertion comes from observations from RANS simulation. Figure 4.1 shows the vorticity distribution of a 2D hydrofoil at high angle of attack. The RANS domain has

to be big enough for this external flow problem, whereas the vorticity only squeeze in a small zone near the wall. The same thing happens in 3D, as shown in Figure 4.2, where a propeller in an open domain operates at low advance ratio. The vorticity distribution is really compact.

In other words, we may say that velocity is a globally distributed quantity, in contrast, vorticity is a locally concentrated quantity. If we solve the vorticity equation, the computational domain can be significantly reduced.

An additional benefit by solving the VISVE is that the effects of viscosity are inherently included, as opposed to the distinct LEV model which is intrinsicly deficient to express gradients associated with viscous dissipation.

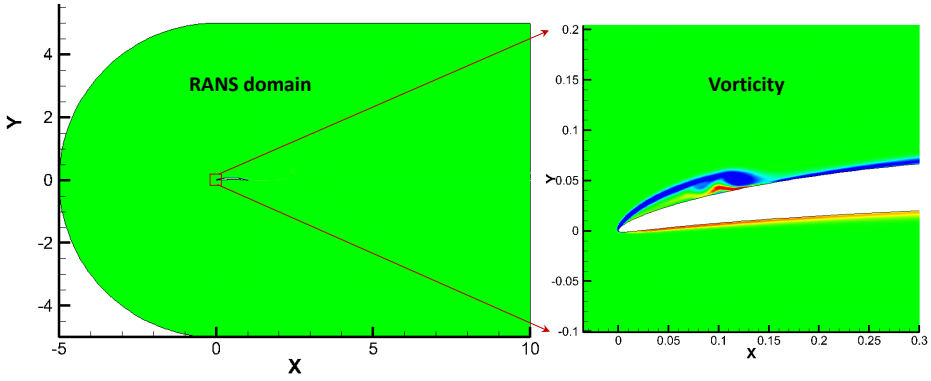

Figure 4.1: Vorticity concentration in 2D: a hydrofoil at high angle of attack

4.2.2 Pros and Cons of the VISVE method

Before exploring the VISVE method in more detail, its benefits and difficulties have to be carefully considered. A major advantage of the VISVE

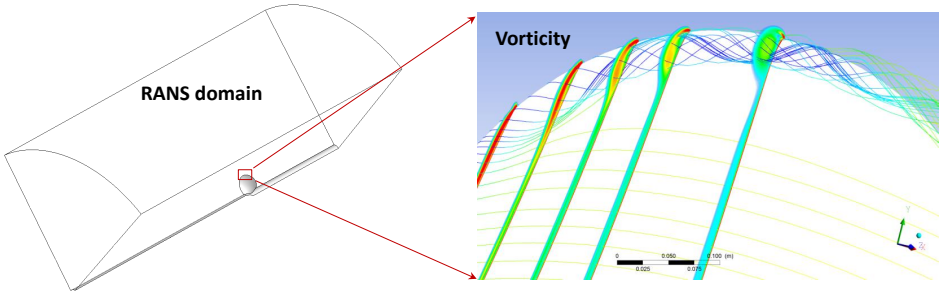

Figure 4.2: Vorticity concentration in 3D: a propeller at low advance ratio

method over the N-S method is that it is possible to construct a local solver with a small computational domain and small number of cells. The method is also beneficial for external flow problems, in which the far-field boundary conditions can be accurately represented via Green's function for Poisson's equation in unbounded domain, as opposed to the N-S method, which approximates the far-field boundary conditions as unperturbed inflow boundaries.

Conceivably, the VISVE method, especially in 3D, is also associated with many difficulties, otherwise it would have been much more popular than it is. First, notice the velocity still appears in the vorticity equation. Two vector fields with six unknowns – $\omega_{1,2,3}$ and $q_{1,2,3}$ are involved, as opposed to N-S method, which has only four unknowns – P and $q_{1,2,3}$. Moreover, both vorticity and velocity are divergence-free vector fields. The divergence-free condition of both vorticity and velocity puts a tight constraint on the solving scheme. Second, the boundary condition on the wall of the VISVE is not straightforward. In the N-S equation, the wall boundary condition can be

easily specified as a Dirichlet boundary condition on velocity and a Neumann boundary condition on pressure. In the VISVE, on the other hand, a vorticity creation algorithm is required on the wall.

4.3 VISVE and its general solving strategy

We re-write (4.1) here for the sake of comparing different forms of the vorticity equation:

$$\frac{\partial \boldsymbol{\omega}}{\partial t} + (\mathbf{q} \cdot \nabla)\boldsymbol{\omega} - (\boldsymbol{\omega} \cdot \nabla)\mathbf{q} = \nu \nabla^2 \boldsymbol{\omega} \tag{4.2}$$

Often the vorticity equation is seen in the form of (4.2), which is sometimes referred to as the *Vorticity Transportation Equation*. The second term in the LHS is the standard convective term in an advection-diffusion equation. The diffusive term because of viscosity appears in the RHS too. The third term in the LHS usually not seen in an advection-diffusion equation, is the vortex-stretching term.

(4.2) can be directly derived from the N-S equation by taking the curl of it, with some manipulation. In the midway from the N-S equation to (4.2), a less often seen 'curl form' of the vorticity equation can be written as:

$$\frac{\partial \boldsymbol{\omega}}{\partial t} + \nabla \times (\boldsymbol{\omega} \times \mathbf{q}) = -\nu \nabla \times (\nabla \times \boldsymbol{\omega}) \tag{4.3}$$

It will be shown in the following chapters that the curl form of the vorticity equation helps maintain a solenoidal vorticity field.

Velocity $\mathbf{q}$ appears in both (4.2) and (4.3). Thus the first step of solving the VISVE is to calculate the corresponding velocity field $\mathbf{q}$ of a given vorticity

distribution. After obtaining $\mathbf{q}$, the vorticity at the current time level $\boldsymbol{\omega}^n$ will be marched to the next time level $\boldsymbol{\omega}^{n+1*}$. Because of the similarity between the VISVE and advection-diffusion equations, the former may be solved using the same techniques of solving the latter. However, $\boldsymbol{\omega}^{n+1*}$ will not satisfy the boundary conditions on the wall. A correction on top of $\boldsymbol{\omega}^{n+1*}$ is necessary to represent the vorticity creation on the wall, in the meantime enforce the boundary conditions (both no-slip and non-penetrating). As summarized in Figure 4.3, the general solving strategy of the VISVE has three components: 1).vorticity-velocity solver; 2). VISVE solver; 3). Vorticity creation.

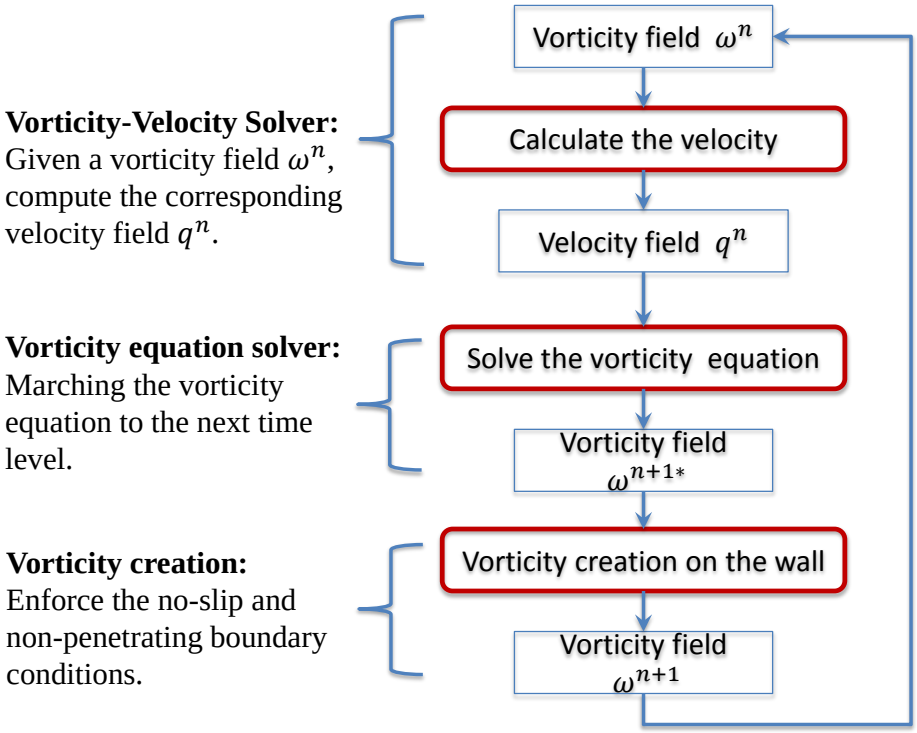

Figure 4.3: Flowchart of the general solving procedures of the VISVE.

4.4 VISVE method in 2D

The use of VISVE in 2D was popular in the past because vorticity degenerate into a scalar. Consequently the vortex stretching term disappears and the VISVE becomes a standard advection-diffusion equation for vorticity:

$$\frac{\partial \omega}{\partial t} + (\mathbf{q} \cdot \nabla)\omega = \nu \nabla^2 \omega \tag{4.4}$$

Though in 2D the VISVE is much simpler than in 3D, the two do share many common problems when being solved. Thus it is worthwhile to first develop the prototype of the VISVE solver in 2D.

4.4.1 Velocity decomposition

It is convenient to decompose the velocity field into three components:

$$\begin{aligned} \mathbf{q} &= \mathbf{U}_\infty + \mathbf{u}_p + \mathbf{u}_\omega \\ &= \mathbf{U}_\infty + \nabla\phi + \mathbf{u}_\omega \end{aligned} \tag{4.5}$$

where $\mathbf{q}$ denotes the total velocity, $\mathbf{U}_\infty$ is the free stream velocity, $\mathbf{u}_p = \nabla\phi$ is the perturbation velocity due to the presence of the object, and $\mathbf{u}_\omega$ represents the induced velocity due to the distributed vorticity in free space. For a particular flow field $\mathbf{q}$, this decomposition is unique, because the free space velocity $\mathbf{u}_\omega$ induced by a given vorticity field can be uniquely determined. It also can be shown that when the no-slip and the non-penetrating boundary conditions are both satisfied, the perturbation potential vanishes. If $\mathbf{q}$ represents the real velocity field, the decomposition should not contain the perturbation potential:

$$\mathbf{q} = \mathbf{U}_\infty + \mathbf{u}_\omega \tag{4.6}$$

In other words, the perturbation potential ϕ in (4.5) merely acts as an intermediate variable. Once the flow field is determined, the perturbation potential should disappear.

4.4.2 Vorticity-velocity solver

The vorticity-velocity solver in 2D is easy to implement with the help of a stream function ψ, which is defined in 3D as:

$$\nabla \times \boldsymbol{\psi} = \mathbf{q} \tag{4.7}$$

Consider the definition of vorticity $\boldsymbol{\omega}$. We have

$$\nabla \times (\nabla \times \boldsymbol{\psi}) = \boldsymbol{\omega} \tag{4.8}$$

which leads to

$$\nabla^2 \boldsymbol{\psi} = -\boldsymbol{\omega} \tag{4.9}$$

where $\nabla \cdot \boldsymbol{\psi} = 0$. (4.9) is an important relation which will be used in the 3D VISVE solver for matching the solutions in the far-field and in the near-field. In 2D, (4.9) also becomes a scalar equation:

$$\nabla^2 \psi = -\omega \tag{4.10}$$

Solving (4.10) per se is straightforward. The tricky part is to specify the boundary conditions. The wall boundary condition in 2D may be specified as a constant, since

$$\frac{\partial \psi}{\partial s} = \mathbf{q} \cdot \mathbf{n} = 0 \tag{4.11}$$

where **n** stands for the normal direction on the wall. The free space boundary conditions, on the other hand, has to be consistent with the flow outside the computational domain. Depending on the type of the solver, matching the computational domain and the external domain can be critical in order to get the correct solution.

4.4.2.1 Volume integral velocity solver

As shown in Figure 4.4, the boundary condition on $\partial\Omega_C$ has to be consistent with the flow field in Ω_E. The Poisson's equation (4.10) can be solved via the Green's function for the Laplacian in free space:

$$\psi(\mathbf{x}_f) = -\int_{\Omega_C} \omega(\mathbf{x}) G(\mathbf{x}, \mathbf{x}_f)\, \mathrm{d}\Omega + \psi_b \tag{4.12}$$

where $\mathbf{x}_f$ is the field point and $\mathbf{x}$ is the dummy variable running over Ω_C; $G(\mathbf{x}, \mathbf{x}_f) = (\ln|\mathbf{x} - \mathbf{x}_f|)/2\pi$ is the Green's function for the Laplacian in 2D. $\psi_b = yU_{\infty,x} - xU_{\infty,y}$ is the stream function corresponding to the background flow. If (4.12) is used everywhere, there is no need to match the solution. Although (4.12), which takes time $O(n^2)$, is computationally intensive, it is still affordable in 2D for a small domain. Theoretically the $O(n^2)$ complexity could be improved via a Fast Multipole Method (FMM) to be $O(n \log n)$ or even $O(n)$ (Greengard and Rohklin 1987)[12]. Thus for the prototype VISVE model in 2D, the direct integration through (4.12) is adopted. An advantage with (4.12) is that the result of the integration is independent of grid skewness. If a Finite Volume Method (FVM) or a Finite Difference Method (FDM) solver

for the original Poisson's equation (4.10) is used, the non-orthogonality of the grid must be taken into account.

When performing (4.12) over the domain, the integral is broken into a sum of the induction from all the cells in the domain. Mathematically the induction due to a cell with constant vorticity distribution is equivalent to the induced potential due to a 2D cell with constant source distribution. For this problem, a closed-form expression is given in Appendix A.

4.4.2.2 FVM velocity solver

Standard FVM can be adopted to solve (4.10) as well. Applying the divergence theorem over a cell leads to the standard five-point stencil for Laplacian in 2D:

$$A\bar{\omega} = -\sum_j \frac{\partial \psi}{\partial n_j} \Delta l_j \tag{4.13}$$

where A is the area of a cell and Δl_j's are the enclosing edges of the cell. In fact, other methods (FDM, FEM) for solving elliptic Partial Differential Equations (PDEs) can also be applied. The reason for choosing the FVM is that the LHS of the algebraic equation is in the same form as that of the contribution of the viscous term in the 2D VISVE. The FVM solver in 2D also has physical significance. As shown in Figure 4.5, since $-\partial\psi/\partial n = q_t$, which is the tangential velocity at the edge of a cell, (4.13) represents the Stokes' theorem.

When using the FVM velocity solver, the solution in Ω_C must match the solution in Ω_E. In order to do so, the Dirichlet boundary condition on

$\partial\Omega_C$ is evaluated through (4.12). On the wall, a constant has to be given for the Dirichlet boundary condition. The constant, denoting as C_{wall} cannot be arbitrary. It can be determined through (4.12). After finding the values of ψ on all the grid points on the wall, the constant is specified to be the averaged value of ψ on the wall. A more efficient way without using (4.12) to determine C_{wall}, is using the no-slip boundary condition on the wall. Because $\partial\psi/\partial n = q_w = 0$, a Neumann boundary condition can be specified. Once the ψ's on the wall are known, they can be replaced by their average in order to ensure the no-penetrating boundary condition, which overweights the importance of the no-slip boundary condition.

The benefit of using the FVM solver instead of the volume integral solver, is that the Poisson solver based on FVM/FDM/FEM can be very efficient. The established techniques(e.g., preconditioning, multi-grid method) in the modern Poisson solver lead to $O(n)$ complexity.

4.4.3 VISVE solver

Once the stream function ψ is known, the VISVE can be solved using general techniques for 2D advection-diffusion equation. In this dissertation, FVM and the Alternating Direction Implicit (ADI) method are adopted. For applying the FVM, (4.4) is written as following conservative form:

$$\frac{\partial\omega}{\partial t} + \nabla\cdot(\mathbf{q}\omega) = \nabla\cdot(\nu\nabla\omega) \tag{4.14}$$

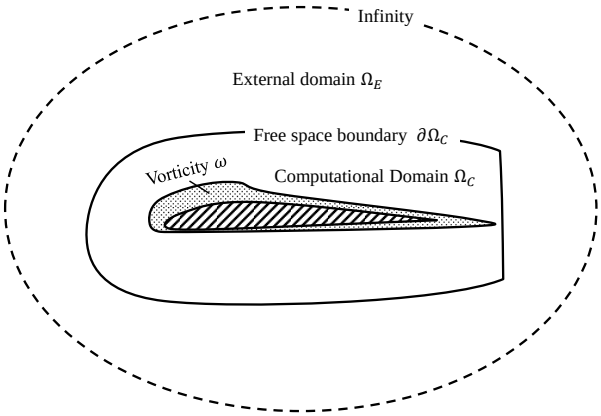

Figure 4.4: Schematic graph of the solution mathcing problem in 2D

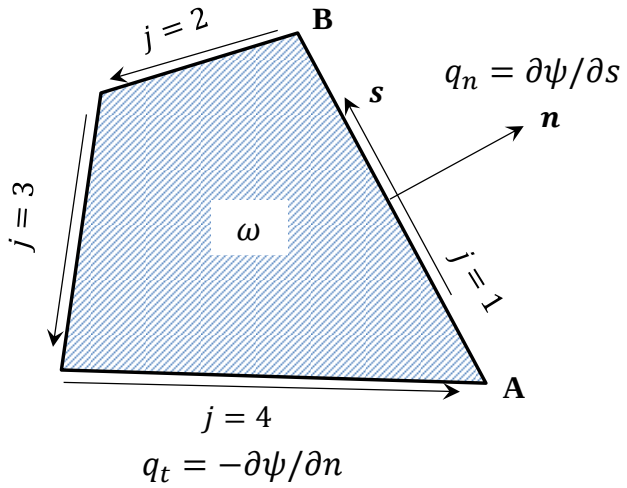

Figure 4.5: Stokes' theorem and the FVM solver

Applying divergence theorem to (4.14), we have the FVM discretization of the VISVE:

$$A\frac{\partial\bar{\omega}}{\partial t} = -\sum_j (\dot{m}\omega)_j + \nu\sum_j \frac{\partial\omega}{\partial n_j}\Delta l_j \tag{4.15}$$

where $\dot{m} = \int_{\partial A_j} \mathbf{q} \cdot \mathbf{n} \, \mathrm{d}l$. Knowing ψ, $\dot{m}$ can be easily evaluated as:

$$\dot{m} = \psi_B - \psi_A \tag{4.16}$$

where A and B denote the starting and ending points of a cell face, as shown in Figure 4.5. Notice (4.16) is exact, and the net mass flux in any cell is automatically nullified.

Standard ADI scheme by Peaceman and Rachford (1995)[32] is used to solve (4.15), which is first split in two directions:

$$\frac{\partial \omega}{\partial t} = (c_1 + d_1)\omega + (c_2 + d_2)\omega \tag{4.17}$$

where $c_{1,2}$ and $d_{1,2}$ are the convective and diffusive operators in directions 1 and 2 respectively. The two ADI sweeps can then be applied:

$$\begin{aligned} \omega^{n+1/2} &= [1 - \frac{\Delta t}{2}(c_1 + d_1)]^{-1}[1 + \frac{\Delta t}{2}(c_2 + d_2)]\omega^n \\ \omega^{n+1} &= [1 - \frac{\Delta t}{2}(c_2 + d_2)]^{-1}[1 + \frac{\Delta t}{2}(c_1 + d_1)]\omega^{n+1/2} \end{aligned} \tag{4.18}$$

4.4.4 QUICK scheme and flux limiter

Quadratic Upstream Interpolation for Convective Kinematics (QUICK) scheme by Leonard (1979)[25] is a popular upwind interpolation scheme for conservation laws. This scheme, with second-order accuracy, is widely considered to be highly conservative. The QUICK scheme for a quantity ϕ in non-uniform grid is given as (Ferziger and Peric 2002)[8]:

$$\phi_f = \phi_U + g_1(\phi_D - \phi_U) + g_2(\phi_U - \phi_{UU}) \tag{4.19}$$

where the subscripts $_f$, $_D$, $_U$ and $_{UU}$ stand for the current face, the downstream, the first upstream and the second upstream cells, as shown in Figure 4.6. The two coefficients g_1 and g_2 are given as:

$$\begin{aligned} g_1 &= \frac{R(\mathbf{x}_f, \mathbf{x}_U) R(\mathbf{x}_f, \mathbf{x}_{UU})}{R(\mathbf{x}_D, \mathbf{x}_U) R(\mathbf{x}_D, \mathbf{x}_{UU})} \\ g_2 &= \frac{R(\mathbf{x}_f, \mathbf{x}_U) R(\mathbf{x}_f, \mathbf{x}_D)}{R(\mathbf{x}_U, \mathbf{x}_{UU}) R(\mathbf{x}_D, \mathbf{x}_{UU})} \end{aligned} \tag{4.20}$$

where $R(\mathbf{x}_1, \mathbf{x}_2)$ is the distance between two points $\mathbf{x}_1$ and $\mathbf{x}_2$.

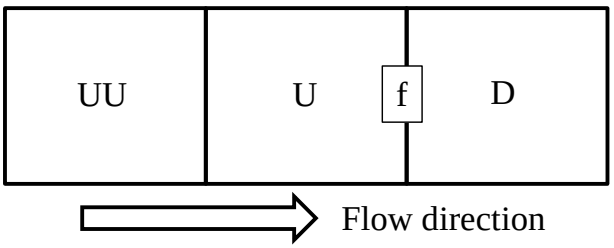

Figure 4.6: Schematic figure of the computational stencil of the QUICK scheme

However, using the QUICK scheme as is showed failure in our numerical test. The QUICK scheme is dispersive for large gradients, which is the case in our application — when modelling the vorticity, the rotational and the irrotational flow regions often share a sharp border. Consider following scenario: a cloud of positive vorticity is marching towards downstream. With the same configuration in Figure 4.6, we have $\phi_{UU} > 0$, $\phi_U = \phi_D = 0$. For uniform grid,

$$\begin{aligned} \phi_f &= \phi_U + \frac{3}{8}(\phi_D - \phi_U) + \frac{1}{8}(\phi_U - \phi_{UU}) \\ &= -\frac{1}{8}\phi_{UU} < 0 \end{aligned} \tag{4.21}$$

A negative ϕ_f causes a negative ϕ_D created from nowhere. This is totally unphysical. In order to ameliorate the performance of the QUICK scheme for large gradients, a flux limiter is necessary.

The flux limiter is a blending function between the first order upwind scheme and a high order scheme. For large gradients, the spatial discretization switches to first order upwind to maintain the monotonicity of the method; for small to moderate gradients, the solver goes back to a high order scheme for better accuracy. This technique is commonly used in the numerical simulation of conservation laws, especially in high speed aerodynamics, to capture the shock wave. In this dissertation, the flux limiter proposed by Woodfield et al (2004)[45] is adopted. The QUICK scheme with the flux limiter becomes:

$$\phi_f = \phi_U + \alpha(\eta)[g_1(\phi_D - \phi_U) + g_2(\phi_U - \phi_{UU})] \tag{4.22}$$

where η is a variable representing the steepness of the gradient:

$$\eta = \frac{\phi_U - \min(\phi_{UU}, \phi_D)}{|\phi_{UU} - \phi_D|} \tag{4.23}$$

$$\alpha = \begin{cases} 0, & \eta < 0 \\ \eta/\delta_f, & 0 < \eta < \delta_f \\ 1, & \delta_f < \eta < 1 - \delta_f \\ 1 - \eta/\delta_f, & 1 - \delta_f < \eta < 1 \\ 0, & 1 < 1 \end{cases} \tag{4.24}$$

where δ_f indicts the size of the blending region between the first order upwind and the QUICK, as shown in Figure 4.7. Obviously bigger δ_f makes the spatial discretization more towards the first order upwind. Woodfield et al

(2004) recommended 0.2 for δ_f. From numerical tests we found $\delta_f = 0.1$ also works with our method in the meantime induces less numerical dissipation, so this value is chosen in this dissertation.

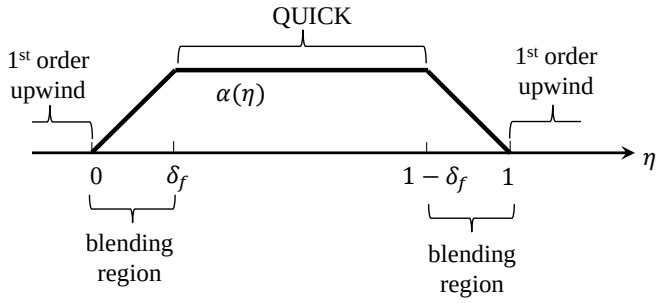

Figure 4.7: Schematic figure of flux limiter by Woodfield et al (2004)[45]

4.4.5 Vorticity creation on the wall

Once the vorticity equation is solved, the vorticity field marches to the next time level, ω^{n+1*}. However, ω^{n+1*} cannot give a velocity field which satisfies the non-penetrating and the no-slip boundary conditions at the same time. Consider the vorticity-velocity solver. On the wall, one can either eliminate the tangential velocity via Dirichlet boundary conditions, or nullify the normal velocity via Neumann boundary conditions. In order to enforce both conditions, new vorticity has to be generated from the wall. The numerical treatment of the vorticity creation on the wall is shown in Figure 4.8.

1. At time t, we have a vorticity distribution ω^n. The vorticity in the first layer cells adjacent to the wall is denoted as ω_b^n.

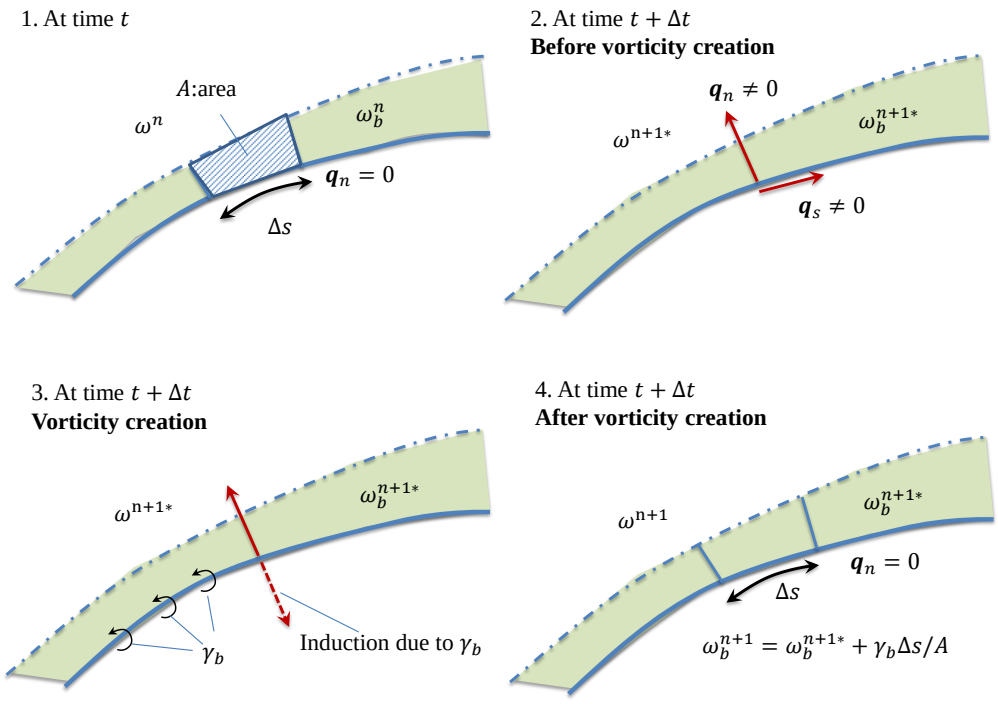

Figure 4.8: Schematic figure of the vorticity creation algorithm.

2. At time $t + \Delta t$, before the vorticity creation, the solution of the VISVE gives a new vorticity distribution ω^{n+1*} and the corresponding ω_b^{n+1*}. The free space induction from ω^{n+1*} along with the background flow gives finite normal as well as tangential velocities on the wall, denoting as q_n and q_s. Both q_n and q_s can be obtained from the two mentioned vorticity-velocity solvers. In 2D, the volume integral velocity solver is convenient to use, since only the values on the wall boundary are needed. In 3D, however, the volume integration becomes more expensive so that

q_s is evaluated through the FVM velocity solver, although it still needs the volume integration to calculate q_n, which serves as the Neumann boundary condition. This procedure is called *inner solution matching* in the 3D VISVE solver, and will be discussed later.

3. At time $t + \Delta t$, in order to eliminate q_n, a Boundary Element Method (BEM) solver is called. In the BEM, the q_n is used to form the RHS. The singularity (dipole in this case) from the solution of the BEM together with q_s can be converted into a sheet of concentrated surface vorticity γ_b. On the wall γ_b induces normal velocities cancelling q_n so that the normal velocity diminishes.

4. At time $t + \Delta t$, after the vorticity creation, the surface vorticity γ_b need to enter the fluid domain. Following the Stokes' theorem γ_b is averaged with the area of the adjacent cells and added on top of the ω_b^{n+1*}. The '*' in the sup-script can now be removed: $\omega_b^{n+1} = \omega_b^{n+1*} + \gamma_b \Delta s/A$. This step is also an approximation of the no-slip boundary condition.

   It is worthwhile to point out that if the background flow is irrotational, the integration of the γ_b along a closed loop, namely, the circulation, should be 0. The numerical integration $\gamma_b \Delta s$ may or may not introduce an accumulation of the second order truncation error. It is important to exclude the accumulated circulation due to numerical integration, otherwise the solution could be spoiled over time.

The basic idea of the vorticity creation algorithm is still valid in 3D. The difference is that in 3D the tangential velocity on the wall has two components.

4.4.6 Application: a 2D hydrofoil at high angle of attack

The distributed LEV model is then applied in the case of a 2D hydrofoil at high Angle Of Attack (AOA). The modeling parameters are listed in table 4.1. The Reynolds number is specified to be 5×10^4. About 7,000

Table 4.1: Modeling parameters of the distributed LEV model on a 2D hydrofoil.

Thickness	t_{max}/c	Camber	f_{max}/c	$\Delta t[c/U_\infty]$	AOA
Naca66	5%	Naca.8	5%	0.00001	10°

cells are used in the VISVE method. In the meantime, a Navier-Stokes (N-S) simulation is also carried out in order to validate the results. All the subsequent N-S simulations in this case are performed using ANSYS Fluent, version 14.5. The N-S simulation uses about 60,000 cells. Figure 4.9 compares the computational domains between the two methods.

Figure 4.10–4.13 show the comparison of the predicted vorticity distribution from the VISVE method and the N-S simulation at different time. Reasonable agreement between the two methods can be observed. Particularly the VISVE method is able to predict the secondary vortex due to the strong viscous interaction between the LEV and the wall. Other methods in the inviscid vortex dynamics will fail in this scenario.

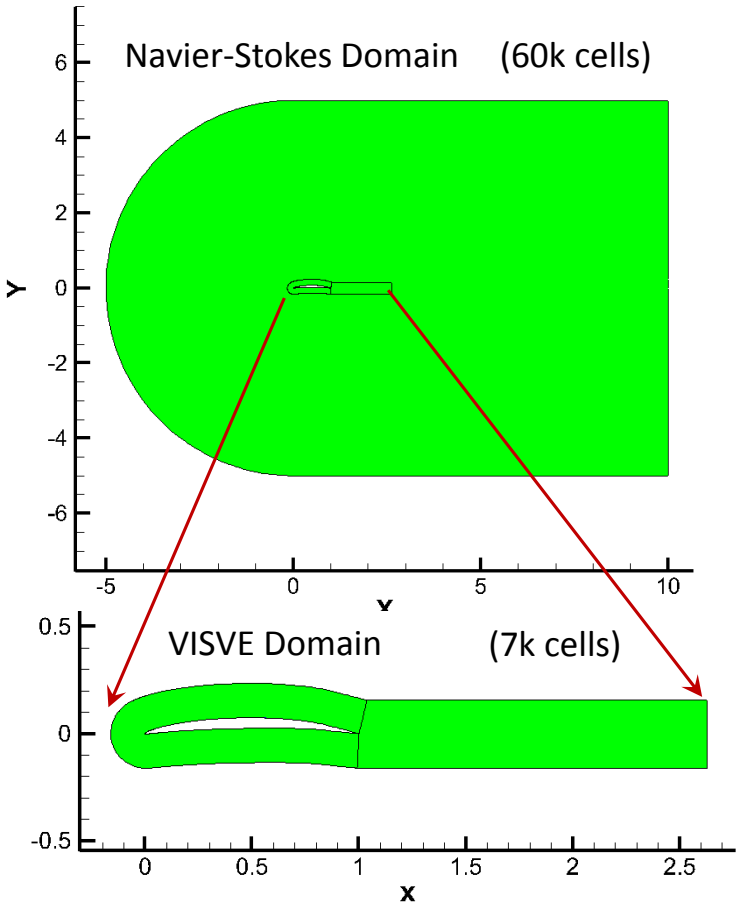

Figure 4.9: Comparison of the computational domain between N-S and VISVE in the case of a 2D hydrofoil at 10° AOA.

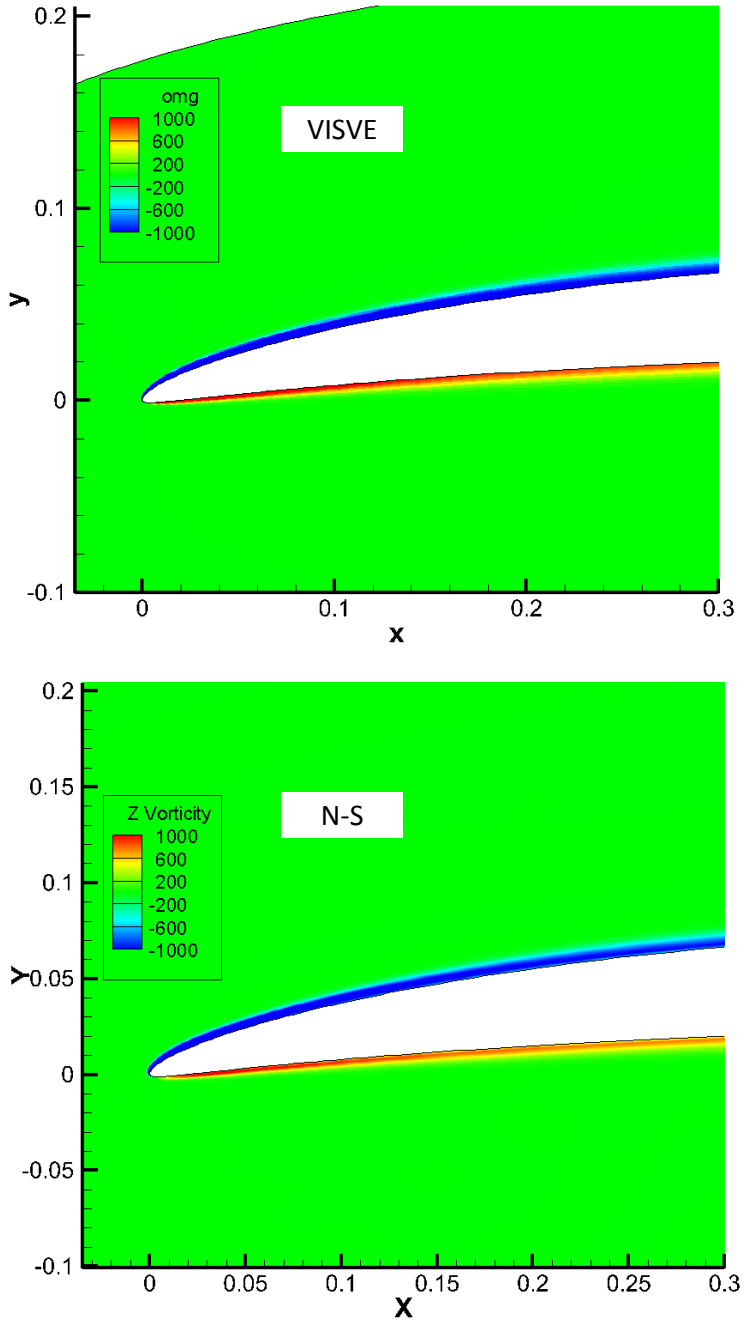

Figure 4.10: Comparison of predicted vorticity between N-S and VISVE in the case of a 2D hydrofoil at 10° AOA, $t = 0.5C/U_\infty$.

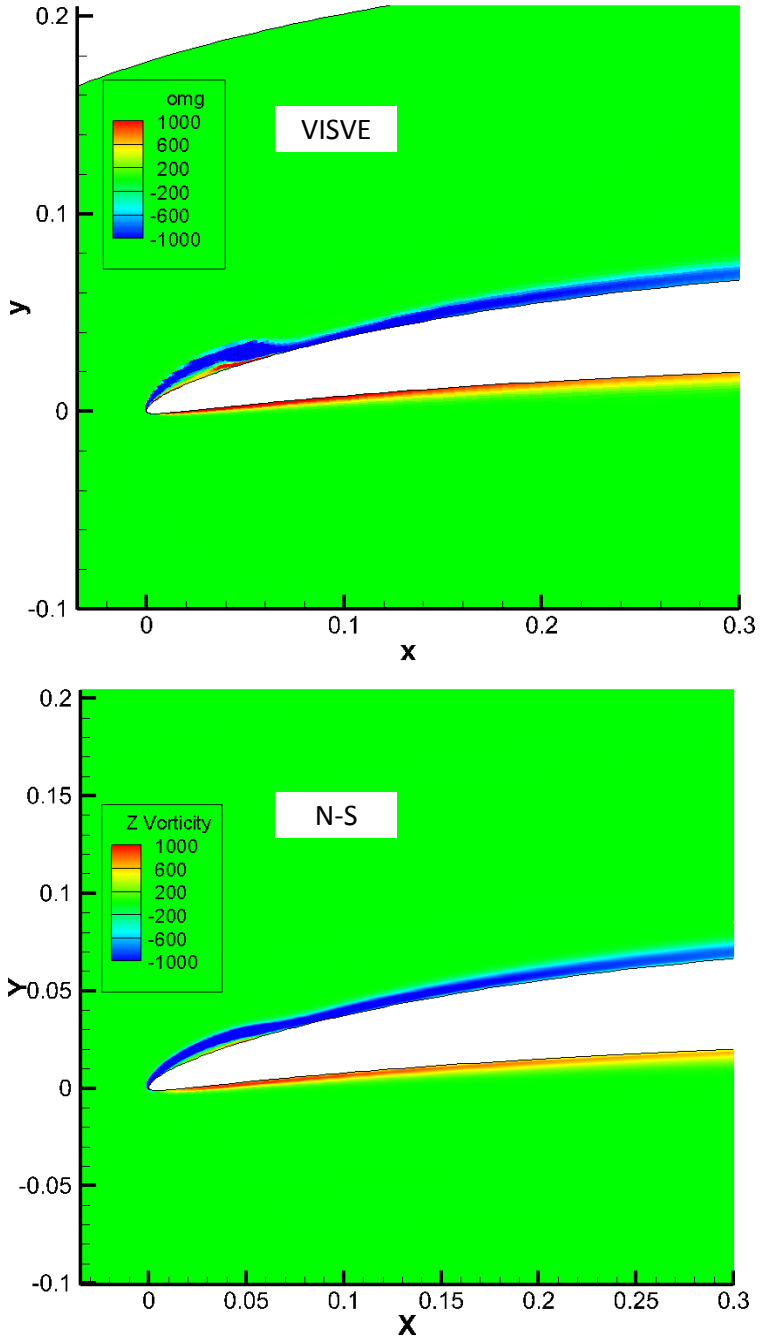

Figure 4.11: Comparison of predicted vorticity between N-S and VISVE in the case of a 2D hydrofoil at 10° AOA, $t = 1.0\mathrm{C}/\mathrm{U}_\infty$.

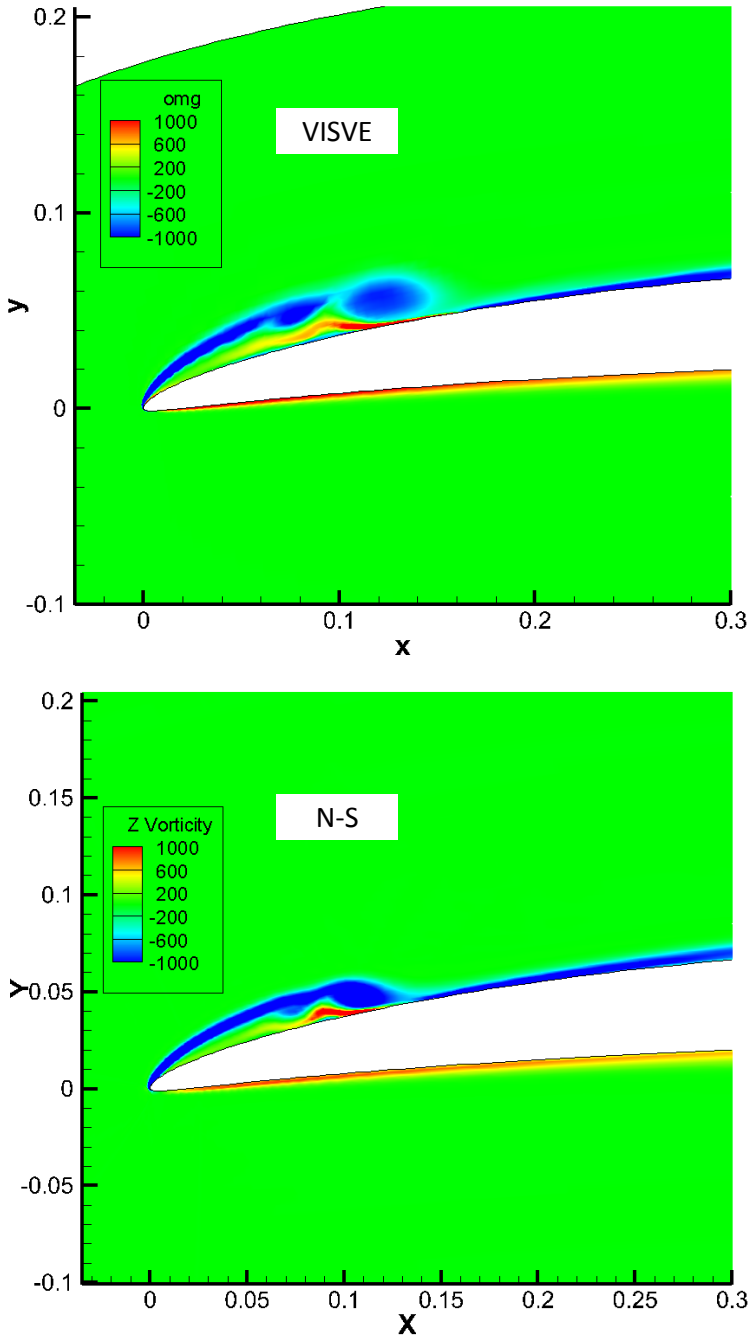

Figure 4.12: Comparison of predicted vorticity between N-S and VISVE in the case of a 2D hydrofoil at 10° AOA, $t = 1.5\mathrm{C}/\mathrm{U}_\infty$.

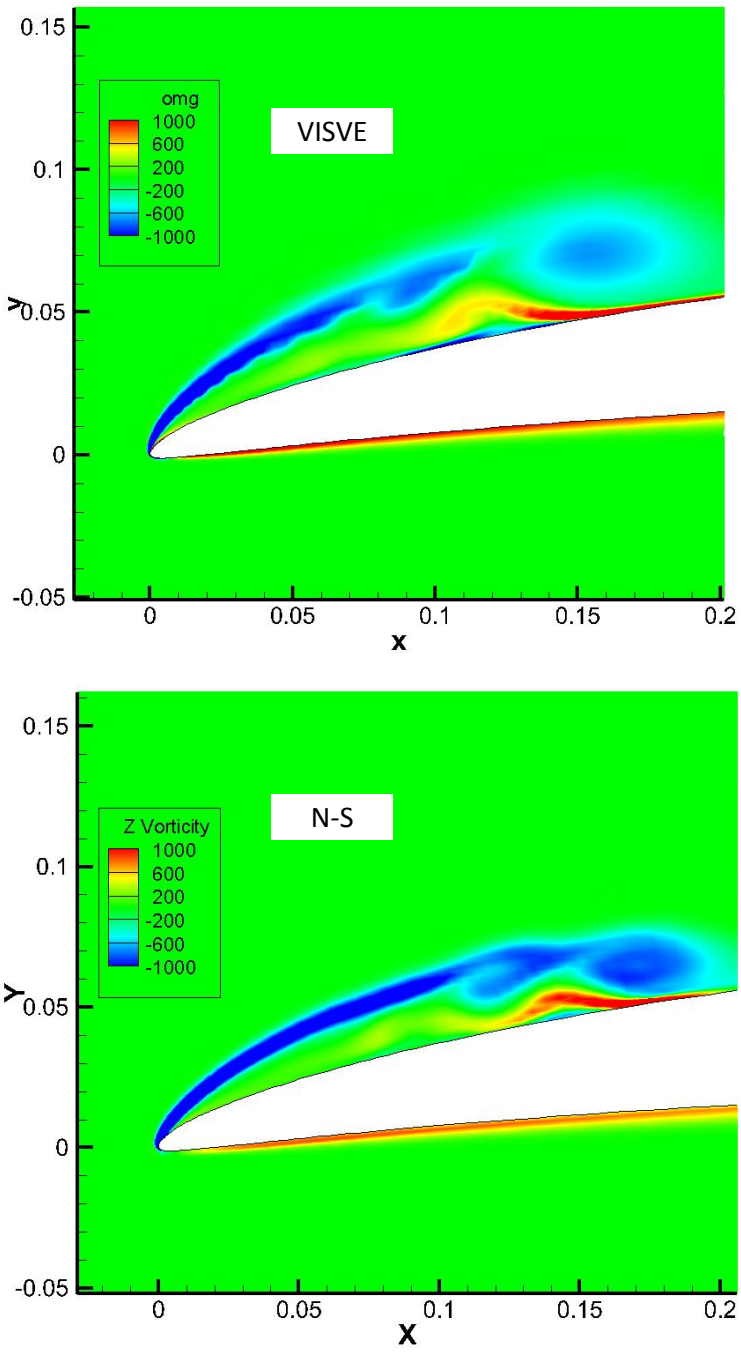

Figure 4.13: Comparison of predicted vorticity between N-S and VISVE in the case of a 2D hydrofoil at 10° AOA, $t = 2.0\mathrm{C}/\mathrm{U}_\infty$.

4.5 VISVE method in 3D

Eventually, we come from the two-dimensional, fictitious world, to the three-dimensional, real world. For the Navier-Stokes method, it requires marginal theoretical efforts, though considerably more work of coding and book keeping is needed. Classic textbooks on Computational Fluid Dynamics (CFD) such as Ferziger and Peric(2002)[8] usually illustrate the solving techniques of the N-S equation in 2D without bothering to put a chapter on how to extend the methods into 3D. For the vorticity equation, however, things become ugly in 3D. Our old friend ψ, the stream function, which is a nice scalar in 2D, now becomes $\boldsymbol{\psi}$, a vector. Thus it is more difficult to construct the vorticity-velocity solver in 3D. The vorticity equation per se, also becomes a vector equation with a nasty vortex stretching term. These difficulties are addressed in the 3D VISVE method.

4.5.1 Vorcitity-velocity solver

As mentioned, the stream function $\boldsymbol{\psi}$ becomes a vector in 3D. In order to obtain $\boldsymbol{\psi}$, three Poisson's equations as shown in (4.9) have to be solved. The increased number of equations is not the biggest problem whereas the boundary condition for $\boldsymbol{\psi}$ is. Underlying (4.9), there is an important condition:

$$\nabla \cdot \boldsymbol{\psi} = 0 \tag{4.25}$$

Without (4.25), the $\boldsymbol{\psi}$ solved from (4.9) cannot recover the flow field $\mathbf{q}$. Take the divergence of (4.9), we have

$$\nabla^2(\nabla \cdot \boldsymbol{\psi}) = -\nabla \cdot \boldsymbol{\omega} = 0 \tag{4.26}$$

Thus the $\nabla \cdot \boldsymbol{\psi}$ satisfies the Laplace equation. Clearly if and only if on the boundary of the computational domain $\nabla \cdot \boldsymbol{\psi} = 0$, (4.25) holds throughout the computational domain. This boundary condition links the three Poisson equations for the three components of $\boldsymbol{\psi}$ and cannot be treated as either a Dirichlet or a Neumann boundary condition. Moreover, the no-slip and non-penetrating boundary conditions cannot be represented easily through simple boundary conditions on $\boldsymbol{\psi}$. For example, the non-penetrating boundary condition requires $\nabla_s \times (\mathbf{n} \times (\boldsymbol{\psi} \times \mathbf{n})) = 0$, where ∇_s is the surface gradient operator on the wall. Although there are still ways to handle these strange boundary conditions, the resulting numerical method could become clumsy, especially when dealing with non-orthogonal grids.

Stream function is still very useful for calculating the normal velocity flux across a cell face induced by a given vorticity distribution in free space. The stream function in 3D can be calculated through volume integration similar to (4.12):

$$\boldsymbol{\psi}(\mathbf{x}_f) = -\int_V \boldsymbol{\omega}(\mathbf{x}) G(\mathbf{x}, \mathbf{x}_f)\, \mathrm{d}V + \boldsymbol{\psi}_b \tag{4.27}$$

where $\mathbf{x}_f$ is the field point and $\mathbf{x}$ is the dummy variable running over the computational domain; $G(\mathbf{x}, \mathbf{x}_f) = -1/(4\pi|\mathbf{x} - \mathbf{x}_f|)$ is the Green's function for the Laplacian in 3D. $\boldsymbol{\psi}_b = (0, xU_{\infty,z} - zU_{\infty,x}, 0)$ is the stream function

corresponding to the background flow. Notice $\boldsymbol{\psi}_b$ does not contain the background rotation, which will be discussed in Section 4.5.7. The integration in (4.27) is broken into a sum of the inductions from all the cells in the domain. In 3D, it is not easy to obtain closed-form expression of the induction from a hexahedral cell, thus approximation or numerical integration is needed. In this dissertation, since the cells often have very small height, their induction are calculated approximately using a planar source panel. The details of this calculation are given in Appendix A.

Knowing the stream function at the corners of a polygonal surface, it is very convenient to calculate the velocity flux across the surface. Recall

$$\mathbf{q} = \nabla \times \boldsymbol{\psi} \tag{4.28}$$

Applying Stokes' theorem on the polygonal face, we have

$$A\bar{q}_n = \iint_A \mathbf{q} \cdot \mathrm{d}\mathbf{A} = \int_{\partial A} \boldsymbol{\psi} \cdot \mathrm{d}\mathbf{l} \tag{4.29}$$

where $\bar{q}_n$ is the face averaged normal velocity, or approximately the normal velocity at the centroid of the face, q_n. For the polygonal face, the contribution from each straight edge on ∂A is evaluated using the trapezoidal rule. The benefit of using (4.29) is that for a closed body represented by many faces, the sum of $A\bar{q}_n$ over all the faces is rigorously zero, since the contribution from each edge is counted twice with opposite signs. The strict conservation of mass is important for the Poisson solver for the velocity field which will be introduced immediately.

4.5.2 A Poisson solver for velocity

Recall the pressure Poisson's equation in the N-S method. A Poisson's equation for a scalar is used to enforce the continuity equation. In N-S, the scalar is the pressure. Borrowing the same idea, in the VISVE method we may be also able to construct a scalar in order to enforce the continuity equation. Consider an unknown velocity field $\mathbf{q}$, which has a known vorticity distribution $\nabla \times \mathbf{q} = \boldsymbol{\omega}$. If there is a known vector field $\mathbf{w}$ which preserves the vorticity field $\nabla \times \mathbf{w} = \boldsymbol{\omega}$, the difference between $\mathbf{q}$ and $\mathbf{w}$ is potential:

$$\mathbf{q} = \mathbf{w} + \nabla\varphi \tag{4.30}$$

The vector field $\mathbf{w}$ does not necessarily satisfy the continuity equation:

$$\nabla \cdot \mathbf{w} \neq 0 \tag{4.31}$$

Take the divergence of (4.32):

$$\nabla \cdot \mathbf{w} + \nabla^2\varphi = \nabla \cdot \mathbf{q} = 0 \tag{4.32}$$

Thus we have:

$$\nabla^2\varphi = -\nabla \cdot \mathbf{w} \tag{4.33}$$

which is a Poisson's equation for φ. Once we solve (4.33) for φ, the real velocity field $\mathbf{q}$ can then be calculated through (4.30). In other words, if we have a cheap way to construct $\mathbf{w}$ which preserves the given vorticity distribution, we can make a potential correction on top of $\mathbf{w}$ to obtain the velocity field $\mathbf{q}$. This procedure in discrete form can be performed on a staggered grid system.

4.5.2.1 Staggered arrangement of variables

The staggered arrangement of variables is an old-fashioned technique for the N-S solvers. This arrangement was popular in the 70 and 80's for its strong coupling between the pressure and the velocities, but started to fade out and be substituted by the gradually maturing collocated arrangement techniques. Staggered arrangement is simple and clean on Cartesian, structured grid, but becomes awkward and even unmanageable on 3D unstructured grid. In our method the staggered arrangement was not considered in the first place, but it does show convenience on the treatment of the curl operator and is adopted in the end. The staggered arrangement does make the book keeping of the code messier, but still manageable. The author really hopes in the future the staggered arrangement can be replaced by a collocated arrangement by mimicking the pressure treatment in the N-S solvers.

As shown in Figure 4.14, the face projection of vorticity is located at the centroid of a face ($\omega_i = \boldsymbol{\omega} \cdot \mathbf{n}_i, i = 1, 2, 3$) and velocity vectors are stored in the center of the surrounding edges of a face. The numbers in the parenthesis indicate the local index of a location. For getting the global index, a (i, j, k) triplet has to be added on top of the local index. For example, the global index for $(1, 1/2, 0)$ is $(i + 1, j + 1/2, k)$.

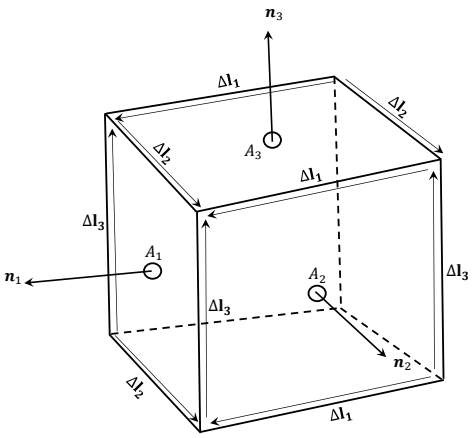

(a). Direction, area and length

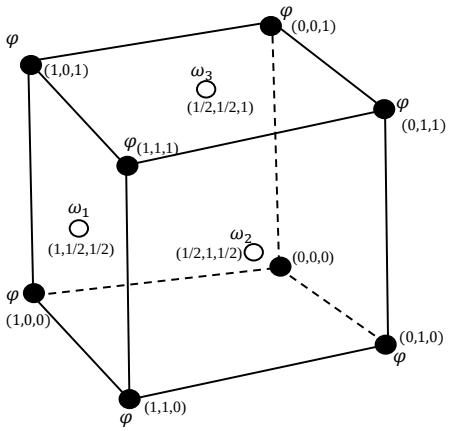

(b). Variables at faces and nodes and their numbering

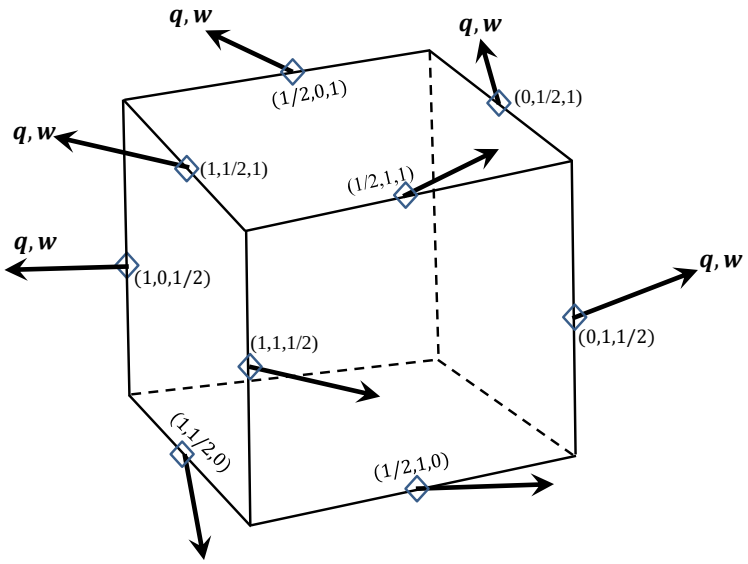

(c). Variables at edges and their local numbering

Figure 4.14: Staggered arrangement of variables.

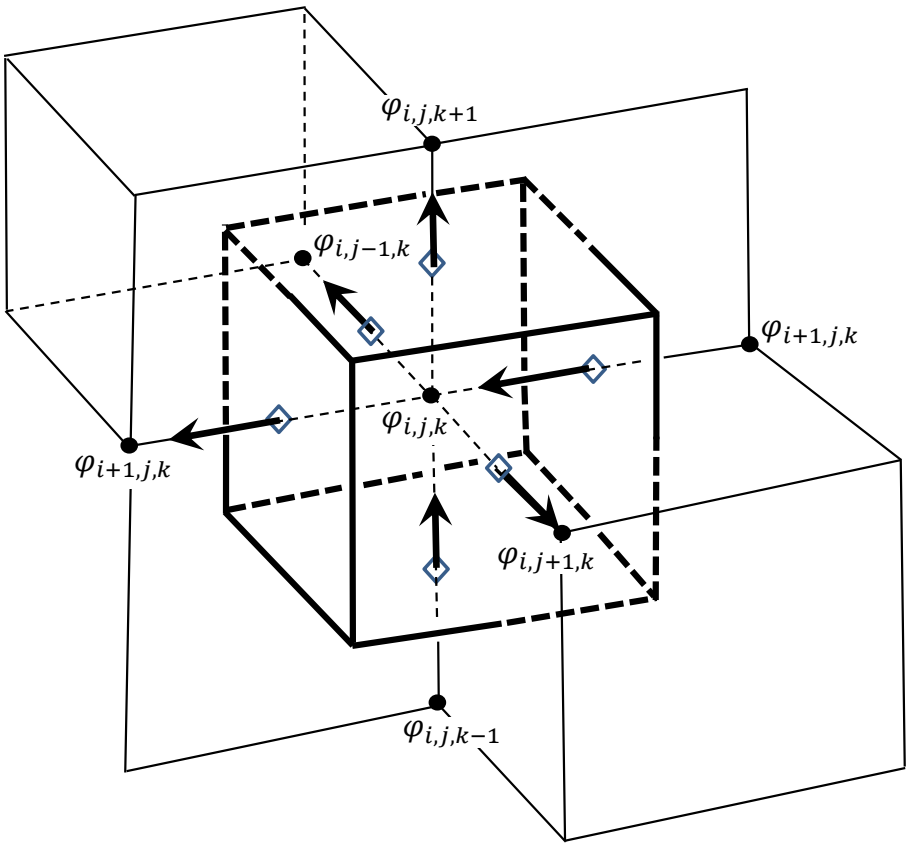

Figure 4.15: Staggered grid for the Poisson's equation in order to enforce the continuity equation.

4.5.2.2 Discretization with FVM

It is convenient to apply the Stokes' theorem with the staggered arrangement. For example, for ω_2 on face $(1/2, 1, 1/2)$, we have

$$\begin{aligned}(A_2\omega_2)_{(1/2,1,1/2)} = (\mathbf{q}\cdot\Delta\mathbf{l}_3)_{(0,1,1/2)} - (\mathbf{q}\cdot\Delta\mathbf{l}_3)_{(1,1,1/2)} \\ + (\mathbf{q}\cdot\Delta\mathbf{l}_1)_{(1/2,1,0)} - (\mathbf{q}\cdot\Delta\mathbf{l}_1)_{(1/2,1,1)}\end{aligned} \tag{4.34}$$

Suppose the vector field $\mathbf{w}$ also preserves the vorticity field $\boldsymbol{\omega}$, we also have

$$\begin{aligned}(A_2\omega_2)_{(1/2,1,1/2)} = (\mathbf{w}\cdot\Delta\mathbf{l}_3)_{(0,1,1/2)} - (\mathbf{w}\cdot\Delta\mathbf{l}_3)_{(1,1,1/2)} \\ + (\mathbf{w}\cdot\Delta\mathbf{l}_1)_{(1/2,1,0)} - (\mathbf{w}\cdot\Delta\mathbf{l}_1)_{(1/2,1,1)}\end{aligned} \tag{4.35}$$

Obviously the $\mathbf{w}$ is not unique. With a given $\mathbf{w}$, one can construct a $\mathbf{w}'$ as $\mathbf{w}' = \mathbf{w} - \alpha\mathbf{w}\times\Delta\mathbf{l}_i$. Therefore we have $\mathbf{w}'\cdot\Delta\mathbf{l}_i = \mathbf{w}\cdot\Delta\mathbf{l}_i$, which means $\mathbf{w}'$ also satisfies (4.35). Consider the most extreme scenario, $\mathbf{w}$ all align with the edges, it is natural to enforce the continuity equation at the nodes, as shown in Figure 4.15. Every node is embedded into a staggered cell which has a 1/2 index shift in all directions. Denoting the area and normal direction of the faces of a staggered cell as A_s and $\mathbf{n}_s$, the volume of the cell as V_s the continuity equation on the cells shown in Figure 4.15 becomes:

$$\begin{aligned}&\left[A_s(\frac{\partial\varphi}{\partial n_{s1}} + \mathbf{w}\cdot\mathbf{n}_{s1})\right]_{i+1/2,j,k} - \left[A_s(\frac{\partial\varphi}{\partial n_{s1}} + \mathbf{w}\cdot\mathbf{n}_{s1})\right]_{i-1/2,j,k} \\ +&\left[A_s(\frac{\partial\varphi}{\partial n_{s2}} + \mathbf{w}\cdot\mathbf{n}_{s2})\right]_{i,j+1/2,k} - \left[A_s(\frac{\partial\varphi}{\partial n_{s2}} + \mathbf{w}\cdot\mathbf{n}_{s2})\right]_{i,j-1/2,k} \\ +&\left[A_s(\frac{\partial\varphi}{\partial n_{s3}} + \mathbf{w}\cdot\mathbf{n}_{s3})\right]_{i,j,k+1/2} - \left[A_s(\frac{\partial\varphi}{\partial n_{s3}} + \mathbf{w}\cdot\mathbf{n}_{s3})\right]_{i,j,k-1/2} \\ =&0\end{aligned} \tag{4.36}$$

Assuming $\mathbf{n}_{si}$'s align with $\Delta\mathbf{l}_i, i = 1, 2, 3$, we have

$$\begin{aligned}
\left.\frac{\partial\varphi}{\partial n_{s1}}\right|_{i+1/2,j,k} &= \frac{\varphi_{i+1,j,k} - \varphi_{i,j,k}}{\Delta l_1\big|_{i+1/2,j,k}} + O(\Delta l^2) \\
\left.\frac{\partial\varphi}{\partial n_{s1}}\right|_{i-1/2,j,k} &= \frac{\varphi_{i,j,k} - \varphi_{i-1,j,k}}{\Delta l_1\big|_{i-1/2,j,k}} + O(\Delta l^2) \\
\left.\frac{\partial\varphi}{\partial n_{s2}}\right|_{i,j+1/2,k} &= \frac{\varphi_{i,j+1,k} - \varphi_{i,j,k}}{\Delta l_2\big|_{i,j+1/2,k}} + O(\Delta l^2) \\
\left.\frac{\partial\varphi}{\partial n_{s2}}\right|_{i,j-1/2,k} &= \frac{\varphi_{i,j,k} - \varphi_{i,j-1,k}}{\Delta l_2\big|_{i,j-1/2,k}} + O(\Delta l^2) \\
\left.\frac{\partial\varphi}{\partial n_{s3}}\right|_{i,j,k+1/2} &= \frac{\varphi_{i,j,k+1} - \varphi_{i,j,k}}{\Delta l_3\big|_{i,j,k+1/2}} + O(\Delta l^2) \\
\left.\frac{\partial\varphi}{\partial n_{s3}}\right|_{i,j,k-1/2} &= \frac{\varphi_{i,j,k} - \varphi_{i,j,k-1}}{\Delta l_3\big|_{i,j,k-1/2}} + O(\Delta l^2)
\end{aligned} \tag{4.37}$$

Substituting (4.37) into (4.36), with some manipulation we have:

$$\begin{aligned}
&B_P\varphi_{i,j,k} \\
&+B_W\varphi_{i+1,j,k} + B_E\varphi_{i-1,j,k} \\
&+B_N\varphi_{i,j+1,k} + B_S\varphi_{i,j-1,k} \\
&+B_T\varphi_{i,j,k+1} + B_B\varphi_{i,j,k+1} = -\dot{m}_{i,j,k}
\end{aligned} \tag{4.38}$$

where

$$\begin{aligned}
B_W &= \left.\frac{A_s}{V\Delta l_1}\right|_{i+1/2,j,k}, \quad B_E = \left.\frac{A_s}{V\Delta l_1}\right|_{i-1/2,j,k} \\
B_N &= \left.\frac{A_s}{V\Delta l_2}\right|_{i,j+1/2,k}, \quad B_S = \left.\frac{A_s}{V\Delta l_2}\right|_{i,j-1/2,k} \\
B_T &= \left.\frac{A_s}{V\Delta l_3}\right|_{i,j,k+1/2}, \quad B_B = \left.\frac{A_s}{V\Delta l_3}\right|_{i,j,k-1/2} \\
B_P &= -(B_W + B_E + B_N + B_S + B_T + B_B)
\end{aligned} \tag{4.39}$$

and

$$\begin{aligned}\dot{m}_{i,j,k} = [&(A_s\mathbf{w}\cdot\mathbf{n}_{s1})_{i+1/2,j,k} - (A_s\mathbf{w}\cdot\mathbf{n}_{s1})_{i-1/2,j,k} \\ &+(A_s\mathbf{w}\cdot\mathbf{n}_{s2})_{i+1/2,j,k} - (A_s\mathbf{w}\cdot\mathbf{n}_{s2})_{i-1/2,j,k} \\ &+(A_s\mathbf{w}\cdot\mathbf{n}_{s3})_{i+1/2,j,k} - (A_s\mathbf{w}\cdot\mathbf{n}_{s3})_{i-1/2,j,k}]/V\end{aligned} \tag{4.40}$$

Clearly (4.38) is the FVM discretization of (4.33) using the standard seven-point stencil for the Lapacian in 3D . After solving (4.38) for φ, the projection of the real velocity field $\mathbf{q}$ on each grid edge can be calculated as:

$$\begin{aligned}(\mathbf{q}\cdot\mathbf{l}_1)_{i+1/2,j,k} &= \frac{\varphi_{i+1,j,k}-\varphi_{i,j,k}}{\Delta l_1\big|_{i+1/2,j,k}} + (\mathbf{w}\cdot\mathbf{l}_1)_{i+1/2,j,k} \\ (\mathbf{q}\cdot\mathbf{l}_2)_{i,j+1/2,k} &= \frac{\varphi_{i,j+1,k}-\varphi_{i,j,k}}{\Delta l_2\big|_{i,j+1/2,k}} + (\mathbf{w}\cdot\mathbf{l}_2)_{i,j+1/2,k} \\ (\mathbf{q}\cdot\mathbf{l}_3)_{i,j,k+1/2} &= \frac{\varphi_{i,j,k+1}-\varphi_{i,j,k}}{\Delta l_3\big|_{i,j,k+1/2}} + (\mathbf{w}\cdot\mathbf{l}_3)_{i,j,k+1/2}\end{aligned} \tag{4.41}$$

where

$$\mathbf{l}_i = \frac{\Delta\mathbf{l}_i}{\Delta l_i}, \qquad i = 1,2,3 \tag{4.42}$$

The results from (4.41) can then be interpolated to recover all the three Cartesian components of $\mathbf{q}$. Up to this point, $\mathbf{q}$ satisfies the continuity equation in discrete sense.

Needless to say, the Poisson solver for velocity for a scalar φ is much more computationally efficient than those using stream functions. The biggest advantage of using the Poisson solver for φ is that it solves a equation directly related to velocity. Consequently the boundary conditions can be easily specified. If the normal velocities on the boundary is known, one can specify a Neumann boundary condition on φ. If the tangential velocities on the boundary is known, one can specify a Dirichlet boundary condition on φ.

Now, the key problem left is that how to construct $\mathbf{w}$ without solving any equations. This problem will be addressed after the VISVE solver and the vorticity creation are discussed.

Notice in the derivation of (4.37), we assumed that $\mathbf{n}_{si}$'s align with $\mathbf{l}_i$'s. This is only true for orthogonal grid. For a general non-orthogonal grid, $\mathbf{n}_{si}$'s differ from $\mathbf{l}_i$'s, and that is the reason we distinguish the two in the derivation after (4.37). The non-orthogonality of the grid will be also be discussed in Section 4.5.6.

4.5.3 VISVE solver

Let us admit that at time level n, knowing the vorticity field $\boldsymbol{\omega}^n$, we have a way to construct $\mathbf{w}^n$ and find the velocity field $\mathbf{q}^n$.We want to solve the vorticity equation (4.2) or (4.3) and march to the next time level $n+1$. Since the staggered arrangement is used, the curl form (4.3) can be easily discretized.

Apply the Stokes' theorem to (4.3) on a cell surface, as shown in Figure 4.16 we have

$$A\frac{\partial \boldsymbol{\omega}\cdot\mathbf{n}}{\partial t}+\sum_{\partial A}(\boldsymbol{\omega}\times\mathbf{q})\cdot\Delta\mathbf{l}=-\nu\sum_{\partial A}(\nabla\times\boldsymbol{\omega})\cdot\Delta\mathbf{l} \tag{4.43}$$

where the normal vector of the face, $\mathbf{n}$ can be $\mathbf{n}_1$, $\mathbf{n}_2$ or $\mathbf{n}_3$. For example, if $\mathbf{n}=\mathbf{n}_3\big|_{i+1/2,j+1/2,k}$, (4.43) becomes:

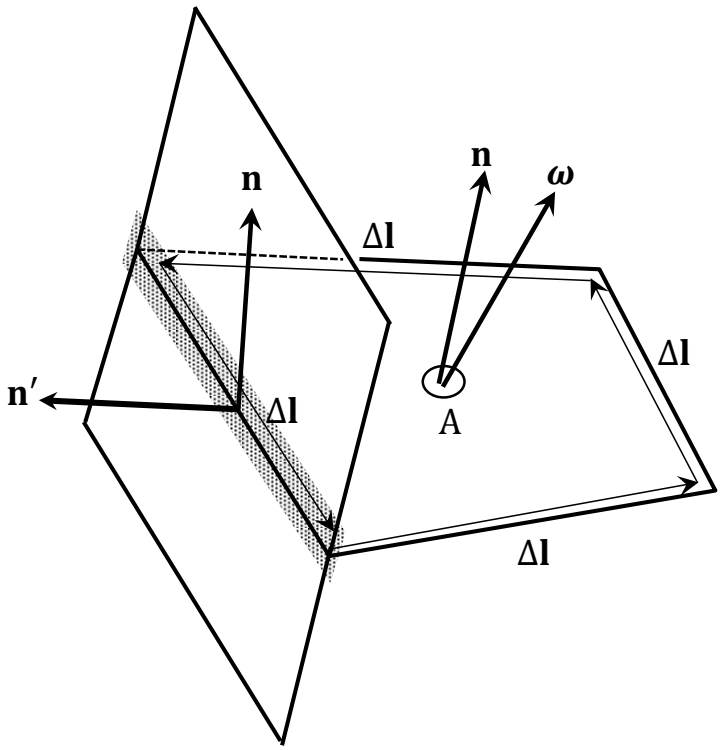

Figure 4.16: Spatial discretization of the VISVE on a face of a cell

$$
\begin{aligned}
&\left(A_3 \frac{\partial \omega_3}{\partial t}\right)_{i+\frac{1}{2},j+\frac{1}{2},k} \\
&+ \left[(\boldsymbol{\omega} \times \mathbf{q}) \cdot \Delta \mathbf{l}_1\right]_{i+\frac{1}{2},j,k} - \left[(\boldsymbol{\omega} \times \mathbf{q}) \cdot \Delta \mathbf{l}_1\right]_{i+\frac{1}{2},j+1,k} \\
&- \left[(\boldsymbol{\omega} \times \mathbf{q}) \cdot \Delta \mathbf{l}_2\right]_{i,j+\frac{1}{2},k} + \left[(\boldsymbol{\omega} \times \mathbf{q}) \cdot \Delta \mathbf{l}_2\right]_{i+1,j+\frac{1}{2},k} \\
=& -\nu \left[(\nabla \times \boldsymbol{\omega}) \cdot \Delta \mathbf{l}_1\right]_{i+\frac{1}{2},j,k} + \nu \left[(\nabla \times \boldsymbol{\omega}) \cdot \Delta \mathbf{l}_1\right]_{i+\frac{1}{2},j+1,k} \\
&+ \nu \left[(\nabla \times \boldsymbol{\omega}) \cdot \Delta \mathbf{l}_2\right]_{i,j+\frac{1}{2},k} - \nu \left[(\nabla \times \boldsymbol{\omega}) \cdot \Delta \mathbf{l}_2\right]_{i+1,j+\frac{1}{2},k}
\end{aligned}
\tag{4.44}
$$

Now we want to express the second and the third terms in (4.43) using

the three face projections of the vorticity: ω_1, ω_2 and ω_3.

4.5.3.1 Convective and stretching term

We first deal with the second term in (4.43). Since we use the curl form of the VISVE, the convective term and the vorticity stretching term become a single term. Consider the edge in Figure 4.16 marked by shadow. Two faces with normal direction $\mathbf{n}$ and $\mathbf{n}'$ pass through the edge. Because it belongs to both faces, both normal vectors are perpendicular to it. Hence for this edge we have

$$\Delta\mathbf{l} = \frac{\mathbf{n}\times\mathbf{n}'}{|\mathbf{n}\times\mathbf{n}'|}\Delta l \tag{4.45}$$

Using the following Lagrange's identity (3D case of the Binet-Cauchy identity):

$$(\mathbf{a}\times\mathbf{b})\cdot(\mathbf{c}\times\mathbf{d}) = (\mathbf{a}\cdot\mathbf{c})(\mathbf{b}\cdot\mathbf{d}) - (\mathbf{a}\cdot\mathbf{d})(\mathbf{b}\cdot\mathbf{c}) \tag{4.46}$$

we have

$$\begin{aligned}(\boldsymbol{\omega}\times\mathbf{q})\cdot\Delta\mathbf{l} &= \frac{\Delta l}{|\mathbf{n}\times\mathbf{n}'|}(\boldsymbol{\omega}\times\mathbf{q})\cdot(\mathbf{n}\times\mathbf{n}') \\ &= \frac{\Delta l}{|\mathbf{n}\times\mathbf{n}'|}\left[\underbrace{(\boldsymbol{\omega}\cdot\mathbf{n})(\mathbf{q}\cdot\mathbf{n}')}_{\text{I}} - \underbrace{(\boldsymbol{\omega}\cdot\mathbf{n}')(\mathbf{q}\cdot\mathbf{n})}_{\text{II}}\right]\end{aligned} \tag{4.47}$$

The term I in (4.47) is called *on-plane convection*, and the term II is called *off-plane convection*. The $\boldsymbol{\omega}\cdot\mathbf{n}$ and $\boldsymbol{\omega}\cdot\mathbf{n}'$ are then two out of the three face projections of $\boldsymbol{\omega}$. For example, for the second term in (4.44), we have $\mathbf{n} = \mathbf{n}_3$ and $\mathbf{n}' = -\mathbf{n}_2$. Thus this term can be written as:

$$(\boldsymbol{\omega}\times\mathbf{q})\cdot\Delta\mathbf{l}_1 = \frac{\Delta l_1}{|\mathbf{n_2}\times\mathbf{n_3}|}[(-\mathbf{q}\cdot\mathbf{n}_2)\omega_3 + (\mathbf{q}\cdot\mathbf{n}_3)\omega_2] \tag{4.48}$$

Similarly we also have:

$$(\boldsymbol{\omega} \times \mathbf{q}) \cdot \Delta \mathbf{l}_2 = \frac{\Delta l_2}{|\mathbf{n_1} \times \mathbf{n_3}|}[(\mathbf{q} \cdot \mathbf{n}_1)\omega_3 - (\mathbf{q} \cdot \mathbf{n}_3)\omega_1] \tag{4.49}$$

(4.44) then becomes:

$$\begin{aligned}
&\left(A_3 \frac{\partial \omega_3}{\partial t}\right)_{i+\frac{1}{2},j+\frac{1}{2},k} \\
&+ \left\{ \frac{\Delta l_1}{|\mathbf{n_2} \times \mathbf{n_3}|}[\underline{(\mathbf{q} \cdot \mathbf{n}_2)\omega_3} - (\mathbf{q} \cdot \mathbf{n}_3)\omega_2] \right\}_{i+\frac{1}{2},j+1,k} \\
&- \left\{ \frac{\Delta l_1}{|\mathbf{n_2} \times \mathbf{n_3}|}[\underline{(\mathbf{q} \cdot \mathbf{n}_2)\omega_3} - (\mathbf{q} \cdot \mathbf{n}_3)\omega_2] \right\}_{i+\frac{1}{2},j,k} \\
&- \left\{ \frac{\Delta l_2}{|\mathbf{n_1} \times \mathbf{n_3}|}[\underline{(\mathbf{q} \cdot \mathbf{n}_1)\omega_3} - (\mathbf{q} \cdot \mathbf{n}_3)\omega_1] \right\}_{i,j+\frac{1}{2},k} \\
&+ \left\{ \frac{\Delta l_2}{|\mathbf{n_1} \times \mathbf{n_3}|}[\underline{(\mathbf{q} \cdot \mathbf{n}_1)\omega_3} - (\mathbf{q} \cdot \mathbf{n}_3)\omega_1] \right\}_{i+1,j+\frac{1}{2},k} \\
&= -\nu\left[(\nabla \times \boldsymbol{\omega}) \cdot \Delta \mathbf{l}_1\right]_{i+\frac{1}{2},j,k} + \nu\left[(\nabla \times \boldsymbol{\omega}) \cdot \Delta \mathbf{l}_1\right]_{i+\frac{1}{2},j+1,k} \\
&+ \nu\left[(\nabla \times \boldsymbol{\omega}) \cdot \Delta \mathbf{l}_2\right]_{i,j+\frac{1}{2},k} - \nu\left[(\nabla \times \boldsymbol{\omega}) \cdot \Delta \mathbf{l}_2\right]_{i+1,j+\frac{1}{2},k}
\end{aligned} \tag{4.50}$$

The meaning of the on-plane and the off-plane terms can immediately be seen from (4.50). All the on-plane terms (underlined) are convection for ω_3, which also appears in the time-dependent term.

It is worthwhile to point out that (4.47) is accurate for both orthogonal or non-orthogonal grid. Thus there is no need to consider the skewness correction for the convective and stretching term. In order to calculate both on-plane and off-plane convective terms, the values of $\omega_{1,2,3}$ must be interpolated to the edges. The QUICK scheme with flux limiter in the 2D VISVE

solver is adopted. The upwinding criteria are the signs of the $\mathbf{q}\cdot\mathbf{n}_1$, $\mathbf{q}\cdot\mathbf{n}_2$ and $\mathbf{q}\cdot\mathbf{n}_3$ in front of the ω_1, ω_2 and ω_3.

4.5.3.2 Diffusive term

We then tackle the third term in (4.43). This term represents the effect of viscosity. Apparently if constant kinematic viscosity ν is used, the solver can only handle laminar flow. The author hopes in the future through an eddy viscosity the effect of turbulence can also be consider to some extent.

In (4.3), the viscous term has a double curl operator. The discretization in (4.43) have already taken off one curl. We have to take care of the left curl operator. As shown in Figure 4.17, the Stokes' theorem is applied on the face of the staggered grid (shadowed).

$$\begin{aligned}
&[(\nabla\times\boldsymbol{\omega})\cdot\Delta\mathbf{l}_2]_{i+1,j+\frac{1}{2},k}\\
&=\left(\frac{\Delta l_2}{A_s}\right)_{i+1,j+\frac{1}{2},k}[(\Delta l_3\omega_3)_{i+\frac{1}{2},j+\frac{1}{2},k}-(\Delta l_3\omega_3)_{i+\frac{3}{2},j+\frac{1}{2},k}]\\
&+\left(\frac{\Delta l_2}{A_s}\right)_{i+1,j+\frac{1}{2},k}[(\Delta l_1\omega_1)_{i+1,j+\frac{1}{2},k+\frac{1}{2}}-(\Delta l_1\omega_1)_{i+1,j+\frac{1}{2},k-\frac{1}{2}}]
\end{aligned}\tag{4.51}$$

Similarly we have

$$\begin{aligned}
&[(\nabla\times\boldsymbol{\omega})\cdot\Delta\mathbf{l}_1]_{i+\frac{1}{2},j+1,k}\\
&=\left(\frac{\Delta l_1}{A_s}\right)_{i+\frac{1}{2},j+1,k}[(\Delta l_3\omega_3)_{i+\frac{1}{2},j+\frac{3}{2},k}-(\Delta l_3\omega_3)_{i+\frac{1}{2},j+\frac{1}{2},k}]\\
&+\left(\frac{\Delta l_1}{A_s}\right)_{i+\frac{1}{2},j+1,k}[(\Delta l_2\omega_2)_{i+\frac{1}{2},j+1,k-\frac{1}{2}}-(\Delta l_2\omega_2)_{i+\frac{1}{2},j+1,k+\frac{1}{2}}]
\end{aligned}\tag{4.52}$$

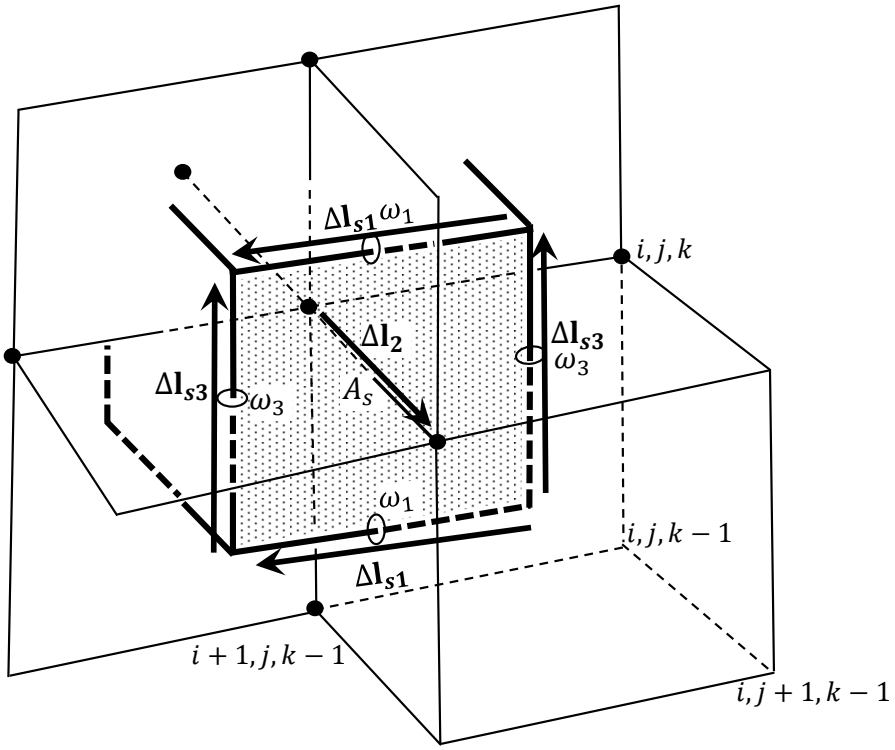

Figure 4.17: Spatial discretization of the viscous term.

(4.50) can then be written, with all the on-plane terms underlined, as:

$$
\begin{aligned}
&\left(A_3\frac{\partial\omega_3}{\partial t}\right)_{i+\frac{1}{2},j+\frac{1}{2},k} \\
&+\left\{\frac{\Delta l_1}{|\mathbf{n_2}\times\mathbf{n_3}|}[\underline{(\mathbf{q}\cdot\mathbf{n}_2)\omega_3}-(\mathbf{q}\cdot\mathbf{n}_3)\omega_2]\right\}_{i+\frac{1}{2},j+1,k} \\
&-\left\{\frac{\Delta l_1}{|\mathbf{n_2}\times\mathbf{n_3}|}[\underline{(\mathbf{q}\cdot\mathbf{n}_2)\omega_3}-(\mathbf{q}\cdot\mathbf{n}_3)\omega_2]\right\}_{i+\frac{1}{2},j,k} \\
&-\left\{\frac{\Delta l_2}{|\mathbf{n_1}\times\mathbf{n_3}|}[\underline{(\mathbf{q}\cdot\mathbf{n}_1)\omega_3}-(\mathbf{q}\cdot\mathbf{n}_3)\omega_1]\right\}_{i,j+\frac{1}{2},k} \\
&+\left\{\frac{\Delta l_2}{|\mathbf{n_1}\times\mathbf{n_3}|}[\underline{(\mathbf{q}\cdot\mathbf{n}_1)\omega_3}-(\mathbf{q}\cdot\mathbf{n}_3)\omega_1]\right\}_{i+1,j+\frac{1}{2},k} \\
=&-\nu\left(\frac{\Delta l_1}{A_s}\right)_{i+\frac{1}{2},j,k}[\underline{(\Delta l_3\omega_3)_{i+\frac{1}{2},j+\frac{1}{2},k}}-\underline{(\Delta l_3\omega_3)_{i+\frac{1}{2},j-\frac{1}{2},k}}] \\
&-\nu\left(\frac{\Delta l_1}{A_s}\right)_{i+\frac{1}{2},j,k}[(\Delta l_2\omega_2)_{i+\frac{1}{2},j,k-\frac{1}{2}}-(\Delta l_2\omega_2)_{i+\frac{1}{2},j,k+\frac{1}{2}}] \qquad (4.53)\\
&+\nu\left(\frac{\Delta l_1}{A_s}\right)_{i+\frac{1}{2},j+1,k}[\underline{(\Delta l_3\omega_3)_{i+\frac{1}{2},j+\frac{3}{2},k}}-\underline{(\Delta l_3\omega_3)_{i+\frac{1}{2},j+\frac{1}{2},k}}] \\
&+\nu\left(\frac{\Delta l_1}{A_s}\right)_{i+\frac{1}{2},j+1,k}[(\Delta l_2\omega_2)_{i+\frac{1}{2},j+1,k-\frac{1}{2}}-(\Delta l_2\omega_2)_{i+\frac{1}{2},j+1,k+\frac{1}{2}}] \\
&+\nu\left(\frac{\Delta l_2}{A_s}\right)_{i,j+\frac{1}{2},k}[\underline{(\Delta l_3\omega_3)_{i-\frac{1}{2},j+\frac{1}{2},k}}-\underline{(\Delta l_3\omega_3)_{i+\frac{1}{2},j+\frac{1}{2},k}}] \\
&+\nu\left(\frac{\Delta l_2}{A_s}\right)_{i,j+\frac{1}{2},k}[(\Delta l_1\omega_1)_{i,j+\frac{1}{2},k+\frac{1}{2}}-(\Delta l_1\omega_1)_{i,j+\frac{1}{2},k-\frac{1}{2}}] \\
&-\nu\left(\frac{\Delta l_2}{A_s}\right)_{i+1,j+\frac{1}{2},k}[\underline{(\Delta l_3\omega_3)_{i+\frac{1}{2},j+\frac{1}{2},k}}-\underline{(\Delta l_3\omega_3)_{i+\frac{3}{2},j+\frac{1}{2},k}}] \\
&-\nu\left(\frac{\Delta l_2}{A_s}\right)_{i+1,j+\frac{1}{2},k}[(\Delta l_1\omega_1)_{i+1,j+\frac{1}{2},k+\frac{1}{2}}-(\Delta l_1\omega_1)_{i+1,j+\frac{1}{2},k-\frac{1}{2}}]
\end{aligned}
$$

(4.53) is lengthy. For the sake of further explanation, (4.53) is re-written

as a more compact form:

$$\begin{aligned}\frac{\partial[A_3\omega_3]}{\partial t} + \mathbb{C}_3(\mathbf{q})[\omega_3] + \mathbb{D}_3[\omega_3] = \mathbb{C}_{13}(\mathbf{q})[\omega_1] + \mathbb{D}_{13}[\omega_1] \\ + \mathbb{C}_{23}(\mathbf{q})[\omega_2] + \mathbb{D}_{23}[\omega_2]\end{aligned} \tag{4.54}$$

where the brackets $[\cdot]$ indicate unknown column vector, and $\mathbb{C}$ and $\mathbb{D}$ are coefficient matricies. The matrices $\mathbb{C}$'s come from the convective and stretching term, and $\mathbb{D}$'s come from the viscous term.

$$\begin{aligned}\mathbb{C}_1 &= \mathbb{C}_{12} + \mathbb{C}_{13} \\ \mathbb{C}_2 &= \mathbb{C}_{21} + \mathbb{C}_{23} \\ \mathbb{C}_3 &= \mathbb{C}_{31} + \mathbb{C}_{32} \\ \mathbb{D}_1 &= \mathbb{D}_{12} + \mathbb{D}_{13} \\ \mathbb{D}_2 &= \mathbb{D}_{21} + \mathbb{D}_{23} \\ \mathbb{D}_3 &= \mathbb{D}_{31} + \mathbb{D}_{32}\end{aligned} \tag{4.55}$$

Clearly the LHS of (4.54) is in the form of an advection-diffusion equation for ω_3, if all the RHS terms are treated as source terms.

Similarly for ω_1 and ω_2 we also have:

$$\begin{aligned}\frac{\partial[A_1\omega_1]}{\partial t} + \mathbb{C}_1(\mathbf{q})[\omega_1] + \mathbb{D}_1[\omega_1] = \mathbb{C}_{21}(\mathbf{q})[\omega_2] + \mathbb{D}_{21}[\omega_2] \\ + \mathbb{C}_{31}(\mathbf{q})[\omega_3] + \mathbb{D}_{31}[\omega_3]\end{aligned} \tag{4.56}$$

$$\begin{aligned}\frac{\partial[A_2\omega_2]}{\partial t} + \mathbb{C}_2(\mathbf{q})[\omega_2] + \mathbb{D}_2[\omega_2] = \mathbb{C}_{12}(\mathbf{q})[\omega_1] + \mathbb{D}_{12}[\omega_1] \\ + \mathbb{C}_{32}(\mathbf{q})[\omega_3] + \mathbb{D}_{32}[\omega_3]\end{aligned} \tag{4.57}$$

Notice the RHS of (4.54) appears in the LHS of (4.56) and (4.57). Thus if we add up (4.54) to (4.57), we have:

$$\frac{\partial[A_1\omega_1]}{\partial t} + \frac{\partial[A_2\omega_2]}{\partial t} + \frac{\partial[A_3\omega_3]}{\partial t} = 0 \tag{4.58}$$

(4.58) shows that by construction the divergence free of the vorticity field is guaranteed, as long as the initial vorticity field is solenoidal.

4.5.3.3 Temporal integration

Discretize the unsteady term in (4.54) to (4.56) using the Euler backward scheme in time. We have

$$\frac{[A_1\omega_1^{n+1*} - A_1\omega_1^n]}{\Delta t} + (\mathbb{C}_1(\mathbf{q}^n) + \mathbb{D}_1)\,[\omega_1^{n+1*}] = (\mathbb{C}_{21}(\mathbf{q}^n) + \mathbb{D}_{21})\,[\omega_2^{n+1*}] + (\mathbb{C}_{31}(\mathbf{q}^n) + \mathbb{D}_{31})\,[\omega_3^{n+1*}] \tag{4.59}$$

$$\frac{[A_2\omega_2^{n+1*} - A_2\omega_2^n]}{\Delta t} + (\mathbb{C}_2(\mathbf{q}^n) + \mathbb{D}_2)\,[\omega_2^{n+1*}] = (\mathbb{C}_{12}(\mathbf{q}^n) + \mathbb{D}_{12})\,[\omega_1^{n+1*}] + (\mathbb{C}_{32}(\mathbf{q}^n) + \mathbb{D}_{32})\,[\omega_3^{n+1*}] \tag{4.60}$$

$$\frac{[A_3\omega_3^{n+1*} - A_3\omega_3^n]}{\Delta t} + (\mathbb{C}_3(\mathbf{q}^n) + \mathbb{D}_3)\,[\omega_3^{n+1*}] = (\mathbb{C}_{23}(\mathbf{q}^n) + \mathbb{D}_{23})\,[\omega_2^{n+1*}] + (\mathbb{C}_{13}(\mathbf{q}^n) + \mathbb{D}_{13})\,[\omega_1^{n+1*}] \tag{4.61}$$

It can be seen that (4.59) to (4.61) are coupled though the RHS's. When solving (4.59) for ω_1, the RHS is treated as known. The solution ω_1^{n+1*} updates the RHS of (4.59) and (4.61), which are handled in the same way. This procedure is performed iteratively until the three unknown components ω_1, ω_2 and ω_3 converge.

The mentioned iterative technique has a few advantages. First, the LHS's of (4.59) –(4.61) are fully decoupled 2D equations. For a computational domain with $n_1 \times n_2 \times n_3$ cells, (4.59) with known RHS represents $n_1 + 1$ 2D equations, which can be solved in parallel without communication between

threads. Moreover, the matrices of the 2D equations in the same direction share the same sparse pattern, thus if a sparse matrix solver is used, the re-ordering and symbolic decomposition can be performed only once.

The solution at the next time level has a $n+1*$ sup-script because the vorticity created on wall in the time interval t to $t+\Delta t$ has not been included into the solution.

4.5.4 Vorticity Creation in 3D

The vorticity creation algorithm in 3D share the same philosophy as in 2D. The $\boldsymbol{\omega}^{n+1*}$ in free space induces velocity field $\mathbf{u}_{\omega}^{n+1*}$. Together with the inflow $\mathbf{U}_{\infty}$, we have a velocity field $\mathbf{q}^{n+1*}$:

$$\mathbf{q}^{n+1*}(\mathbf{x}_p) = \mathbf{U}_{\infty} + \nabla \times \int \frac{\boldsymbol{\omega}^{n+1*}}{4\pi|\mathbf{x}-\mathbf{x}_p|}\,\mathrm{d}V \tag{4.62}$$

where $\mathbf{x}_p$ is the field point, and $\mathbf{x}$ is the dummy variables running through the computational domain. $\mathbf{q}^{n+1*}$ does not satisfy the no-slip and the non-penetrating boundary conditions on the wall. As in the 2D VISVE method, the normal component of $\mathbf{q}^{n+1*}$, q_n^{n+1*}, is used to form the RHS of a BEM solver solving for a potential distribution ϕ on the wall:

$$\frac{\partial \phi}{\partial n} = -q_n^{n+1*} \tag{4.63}$$

Once the ϕ on the wall is determined, the $\partial\phi/\partial s$ together with the tangential component of $\mathbf{q}^{n+1*}$ on the wall, $\mathbf{q}_s^{n+1*}$, give the created vorticity $\boldsymbol{\gamma}_b$:

$$\boldsymbol{\gamma}_b = -\mathbf{q}_s^{n+1*} - \nabla_s \phi \tag{4.64}$$

where $\nabla_s = (\partial/\partial s_1, \partial/\partial s_2)$ is the gradient operator on the wall. The $\boldsymbol{\gamma}_b$ then enters the adjacent cell, as shown in Figure 4.18:

$$\omega_1^{n+1}\Big|_{i,j+\frac{1}{2},k+\frac{1}{2}} = \begin{cases} \omega_1^{n+1*}\Big|_{i,j+\frac{1}{2},k+\frac{1}{2}} + \gamma_{b2}\Big|_{i,j+\frac{1}{2}} \dfrac{\Delta l_2\Big|_{i,j+\frac{1}{2},k}}{A_1\Big|_{i,j+\frac{1}{2},k+\frac{1}{2}}} & k=0 \\ \omega_1^{n+1*}\Big|_{i,j+\frac{1}{2},k+\frac{1}{2}} & k>0 \end{cases} \tag{4.65}$$

$$\omega_2^{n+1}\Big|_{i+\frac{1}{2},j,k+\frac{1}{2}} = \begin{cases} \omega_2^{n+1*}\Big|_{i+\frac{1}{2},j,k+\frac{1}{2}} + \gamma_{b1}\Big|_{i+\frac{1}{2},j} \dfrac{\Delta l_1\Big|_{i+\frac{1}{2},j,k}}{A_2\Big|_{i+\frac{1}{2},j,k+\frac{1}{2}}} & k=0 \\ \omega_2^{n+1*}\Big|_{i+\frac{1}{2},j,k+\frac{1}{2}} & k>0 \end{cases} \tag{4.66}$$

When using (4.65) and (4.66), one must be careful with the subscripts of γ_b, since γ_{b1} contributes to ω_2 and γ_{b2} contributes to ω_1.

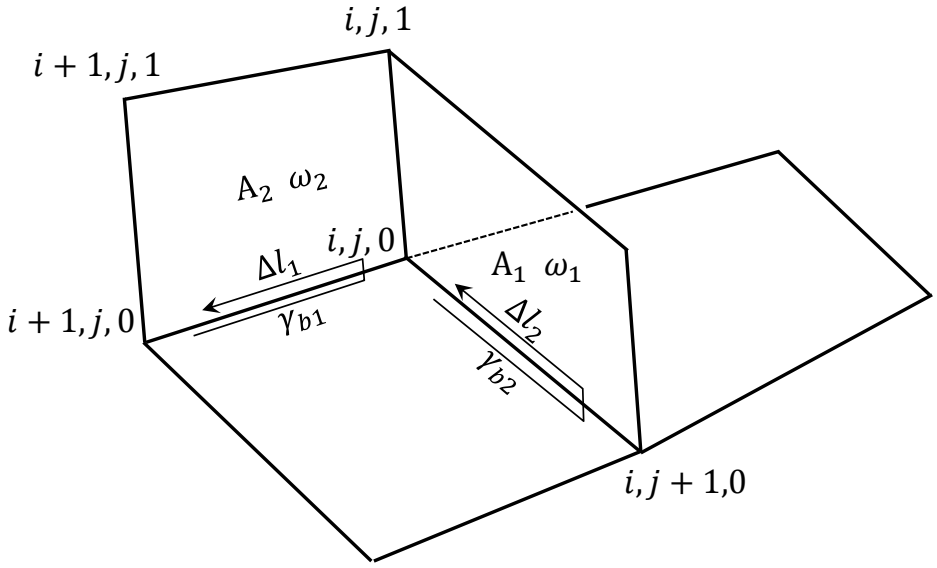

Figure 4.18: Vorticity creation on the wall, in 3D

In 2D, the tangential component of $\mathbf{q}^{n+1*}$ on the wall can be easily

calculated through direct integration. However, in 3D the stream function only gives the normal component q_n^{n+1*}. If the tangential component is needed, a volume integration using the Biot-Savart kernel, which is more singular than the point source kernel must be carried out. Alternatively, the $\mathbf{q}_s^{n+1*}$ on the wall can be calculated through the Poisson solver, which is more efficient than direct integration. When using the Poisson solver, the normal velocity on the outer boundary and on the wall due to ω^{n+1*} and the inflow U_∞ are calculated and used as Neumann boundary conditions. Using the normal velocity on the wall as the boundary condition for the Poisson's equation is called *inner solution matching*, because the solution of the Poisson's equation matches the velocity field $\mathbf{q}^{n+1*}$ defined in (4.62)

It seems to be an overkill to use the Poisson solver, which calculates the velocity in the whole computational domain, to evaluate only the velocity on the wall, but at this stage, the Poisson solver is numerically more efficient than direct integration with the Biot-Savart kernel.

4.5.5 Construction of the vorticity preserving field, w

Now that we have discussed the numerical scheme marching from $\boldsymbol{\omega}^n$ to $\boldsymbol{\omega}^{n+1}$, it is a good time to explain how the vorticity preserving field $\mathbf{w}^{n+1}$ is determined.

Consider the requirement of $\mathbf{w}^{n+1}$, using the configuration in Figure 4.16:

$$A\boldsymbol{\omega}^{n+1} \cdot \mathbf{n} = \sum_{\partial A} \mathbf{w}^{n+1} \cdot \Delta\mathbf{l} \tag{4.67}$$

For cell faces not adjacent to the wall, $\boldsymbol{\omega}^{n+1} = \boldsymbol{\omega}^{n+1*}$, since the vorticity creation only affects the first layer of cells. Recall

$$A\boldsymbol{\omega}^{n+1} \cdot \mathbf{n} = \Delta t \sum_{\partial A} [-(\boldsymbol{\omega}^{n+1*} \times \mathbf{q}^n) + \nu \nabla \times \boldsymbol{\omega}^{n+1*}] \cdot \Delta \mathbf{l} + A\boldsymbol{\omega}^n \cdot \mathbf{n} \quad (4.68)$$

and

$$A\boldsymbol{\omega}^n \cdot \mathbf{n} = \sum_{\partial A} \mathbf{q}^n \cdot \Delta \mathbf{l} \quad (4.69)$$

Comparing (4.67), (4.68) and (4.69), we have

$$\mathbf{w}^{n+1} = \Delta t[-(\boldsymbol{\omega}^{n+1*} \times \mathbf{q}^n) + \nu \nabla \times \boldsymbol{\omega}^{n+1*}] + \mathbf{q}^n \quad (4.70)$$

For the cell face adjacent to the wall, the newly created vorticity has to be considered. It can be easily shown that following construction for the edges on the wall recovers the ω^{n+1} in the first layer of cells:

$$\mathbf{w}^{n+1} = \Delta t[-(\boldsymbol{\omega}^{n+1*} \times \mathbf{q}^n) + \nu \nabla \times \boldsymbol{\omega}^{n+1*}] + \mathbf{q}^n + \mathbf{q}_s^{n+1*} + \nabla_s \phi^{n+1} \quad (4.71)$$

Both (4.70) and (4.71) are explicit, because all the terms in the RHS are known once $\boldsymbol{\omega}^{n+1}$ is known.

Up to now, all the major steps in the loop shown in Figure 4.3 are covered. A few more details in the method will be discussed in the following sections.

4.5.6 Grid non-orthogonality

Generally, the computational grid is not orthogonal. As shown in the previous sections, the grid non-orthogonality causes no additional discretiza-

tion error other than the local truncation error for the convective and stretching terms which only involve with first order derivatives. However, for terms have second order derivatives, the error because of the grid non-orthogonality must be considered.

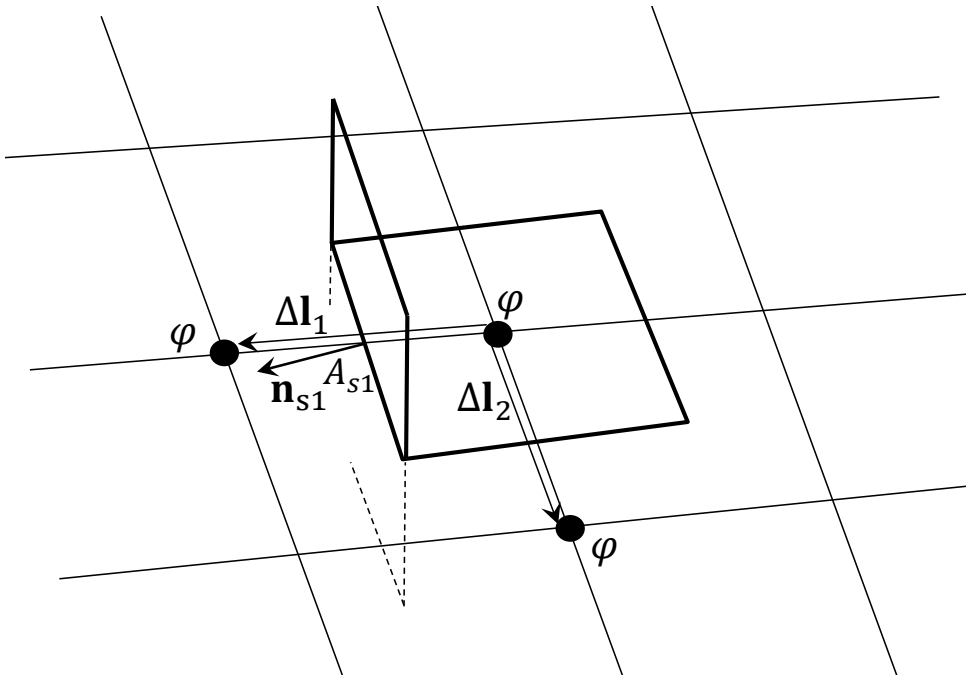

Figure 4.19: Schematic plot of the non-orthogonality of the grid

Take the Poisson's equation for velocity for an example, for a non-orthogonal grid, as shown in Figure 4.19, the normal vector of face A_{s1}, $\mathbf{n}_{s1}$ does not align with the edge $\Delta\mathbf{l}_1$, the face flux across face A_{s1} not only has a contribution from $\partial\varphi/\partial l_1$, but has a contribution from $\partial\varphi/\partial l_2$. Including the mixed derivatives such as flux due to $\partial\varphi/\partial l_2$ on A_{s1} to the LHS greatly increases the difficulty of coding, as well as the size the computational stencil.

Currently the mixed derivatives are put into the RHS in an iterative manner:

$$A_{s1}\left(\frac{\partial\varphi}{\partial n_{s1}}\right) = A_{s1}\left(\frac{\partial\varphi}{\partial l_1}\right)^{\text{new}} + A_{s1}\left(\frac{\partial\varphi}{\partial n_{s1}} - \frac{\partial\varphi}{\partial l_1}\right)^{\text{old}} \tag{4.72}$$

Thus the first term in the RHS of (4.72) still appears in the LHS of the linear algebraic system as if the grid is orthogonal, whereas the second term in the RHS of (4.72) is put into the RHS of the linear algebraic system as a correction term. The correction term is updated with newly evaluated φ, and should converge after a few iterations. This deferred-correction technique, on the one hand, simplifies the programing, on the other hand, may slow down the simulation since iteration is needed. For grid with large skewness, the results may even diverge.

4.5.7 Rotational frame of reference

When modeling the propeller flow, it is convenient to use the rotational frame of reference. In the meantime, the background rotation carries a uniform vorticity, which must be excluded from the vorticity field when solving the VISVE.

For a right handed propeller operating with rotational speed Ω, the rotational velocity vector is $(-\Omega, 0, 0)$. Denoting $\mathbf{\Omega} = (\Omega, 0, 0)$, we have

$$\mathbf{q}_r = \mathbf{q}_a + \mathbf{\Omega} \times \mathbf{r} \tag{4.73}$$

where $\mathbf{q}_a$ is the velocity under the inertial frame of reference, and $\mathbf{q}_r$ is the velocity in the rotational frame of reference. $\mathbf{r} = (0, y, z)$ is the radial vector of

a field point. The vorticity $\boldsymbol{\omega}$ is defined under the inertial frame of reference:

$$\boldsymbol{\omega} = \nabla \times \mathbf{q}_a \tag{4.74}$$

The background rotation add a constant vorticity $2\boldsymbol{\Omega}$ into the relative velocity field $\mathbf{q}_r$:

$$\boldsymbol{\omega} + 2\boldsymbol{\Omega} = \nabla \times \mathbf{q}_r \tag{4.75}$$

The momentum equation in the rotational frame of reference is written as:

$$\frac{\partial \mathbf{q}_r}{\partial t} + \mathbf{q}_r \cdot \nabla \mathbf{q}_r - 2\boldsymbol{\Omega} \times \mathbf{q}_r - \Omega^2 \mathbf{r} = -\nabla P + \nu \nabla^2 \mathbf{q}_r \tag{4.76}$$

Substituting (4.75) into (4.76), with some manipulation, we have

$$\frac{\partial \mathbf{q}_r}{\partial t} + \nabla \left(\frac{q_r^2}{2} + P - \frac{\Omega^2 r^2}{2} \right) = \mathbf{q}_r \times \boldsymbol{\omega} + \nu \nabla^2 \mathbf{q}_r \tag{4.77}$$

Taking the curl of (4.77) gives the VISVE in the rotational frame of reference:

$$\frac{\partial \boldsymbol{\omega}}{\partial t} + \nabla \times (\boldsymbol{\omega} \times \mathbf{q}_r) = -\nu \nabla \times (\nabla \times \boldsymbol{\omega}) \tag{4.78}$$

(4.78) shows that in the rotational frame of reference, the VISVE keeps the same form as that in the inertial frame of reference. Meanwhile, the velocity in the VISVE must be the relative velocity $\mathbf{q}_r$. Notice that the $\mathbf{w}$ constructed using (4.70) and (4.71) does not contain the vorticity due to the background rotation $2\boldsymbol{\Omega}$, when solving the Poisson's equation for $\mathbf{q}_r$, the contribution of $2\boldsymbol{\Omega}$ must be added into $\mathbf{w}$.

Consider an edge has two nods $\mathbf{x}_1 = (x_1, y_1, z_1)$ and $\mathbf{x}_2 = (x_2, y_2, z_2)$, the contribution of the background rotation on this edge to the vorticity preserving

field $\mathbf{w}$ is:

$$\begin{aligned}\mathbf{w}_b \cdot \Delta\mathbf{l} &= \int_{\mathbf{x}_1}^{\mathbf{x}_2} \boldsymbol{\Omega} \times \mathbf{r} \cdot \mathrm{d}\mathbf{l} \\ &= \Omega(y_1 z_2 - z_1 y_2)\end{aligned} \tag{4.79}$$

where $\mathbf{w}_b$ stands for the additional correction on $\mathbf{w}$ due to the background rotation. When the rotational frame of reference is used, before calling the Poisson solver for velocity, $\mathbf{w}_b$ must be added into $\mathbf{w}$ calculated from (4.70) and (4.71).

Since the Poisson solver is corresponding to $\mathbf{q}_r$, the Neumann boundary condition should also incorporate the background rotation. The $\boldsymbol{\psi}_b$ in (4.27) must be corrected as:

$$\boldsymbol{\psi}_b = (-\frac{1}{2}\Omega r^2, xU_{\infty,z} - zU_{\infty,x}, 0) \tag{4.80}$$

4.5.8 Pressure calculation

In the VISVE, pressure is not directly in the solution and has to be calculated through post-processing. Define the total head H as:

$$H = \frac{q_r^2}{2} + P - \frac{\Omega^2 r^2}{2} \tag{4.81}$$

From (4.77) we can obtain:

$$\nabla H = -\frac{\partial \mathbf{q}_r}{\partial t} + \mathbf{q}_r \times \boldsymbol{\omega} - \nu \nabla \times (\nabla \times \boldsymbol{\omega}) \tag{4.82}$$

Integrating the RHS of (4.82) gives H, and consequently, the pressure P. In fact there are certain relation between φ and H. Thus (4.82) may not need to be explicitly integrated to find H. However, more careful investigation is needed in order to use φ in the pressure calculation.

4.5.9 Potential wake model

The wake of a propeller extends for a considerably long distance. In order to retain the spatial compactness of the method, a potential wake model, which works well for boundary element method, is included.

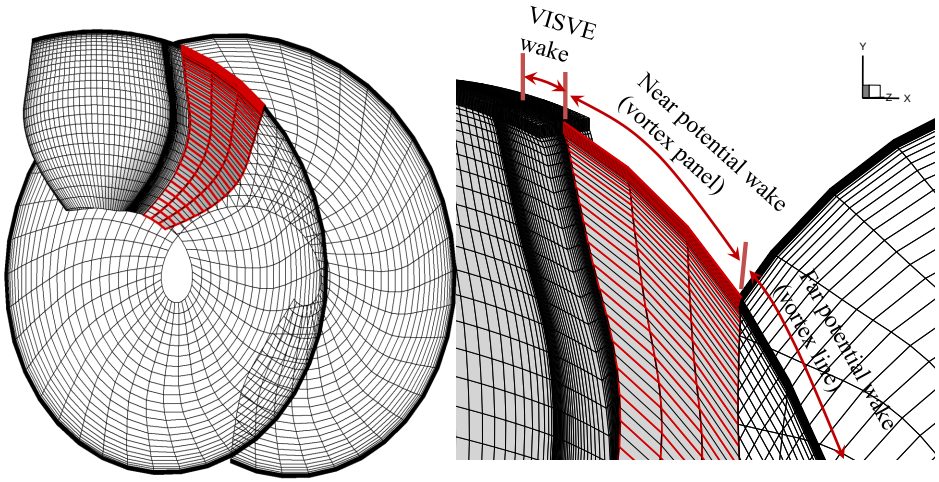

Figure 4.20: Schematic plot of the wake model for a propeller.

AS shown in Figure 4.20, the trailing edge wake of a propeller is modeled as three parts: 1). the VISVE wake; 2). the near potential wake; 3). the far potential wake.

The VISVE wake is the natural extension of the computational domain after the tailing edge of the propeller blade. In this region, the VISVE is still solved. The total vorticity across the end of the VISVE wake, denoted as Γ_W, are passed to the near potential wake.

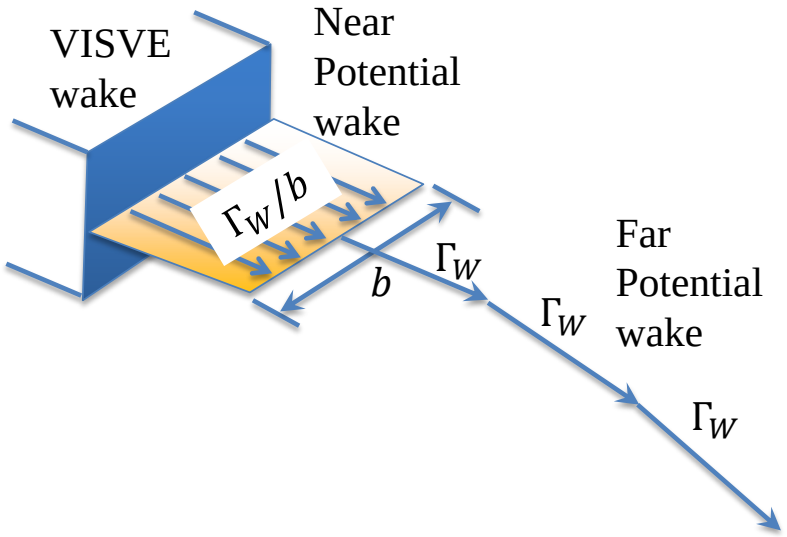

Figure 4.21: Strength of the singularities on the potential wake.

As shown in Figure 4.21, in the near potential wake region, the wake is modeled using constant vortex panels. The strength of the vortex equals to Γ_W/b, where b is the width of the panel.

In the far potential wake region, the wake is modeled using vortex lines. The vortex strength for each line is specified as Γ_W.

4.5.10 A complete flowchart

Up to now, all the solving techniques in the VISVE method are discussed. A complete flowchart of the numerical code is shown in Figure 4.22

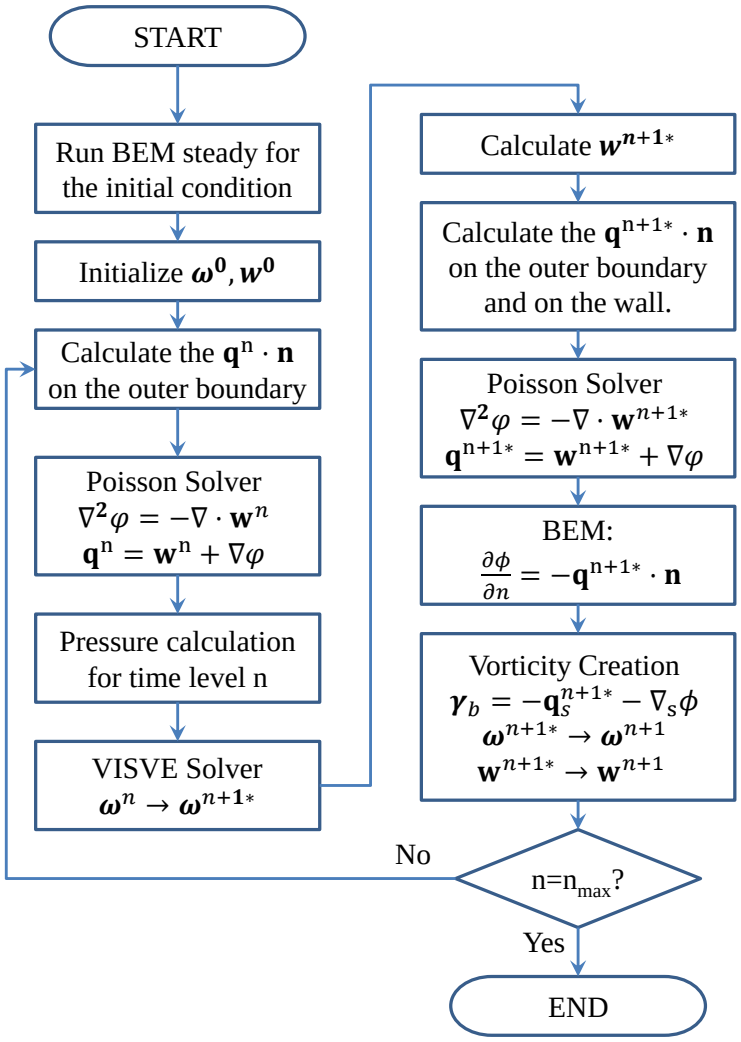

Figure 4.22: A complete flowchart of the numerical code of the VISVE method.

4.5.11 Application: LEV of a 3D wing

The VISVE method is applied in the case of a 3D swept wing at 6 degree AOA. The wing has a 5% thickness/camber ratio at mid-span. The ratio decreases linearly to zero towards the tip. The wing is constructed with a NACA 66 thickness form and no camber through all the spanwise stations. The plan-form of the wing as well as the surface panels in BEM is shown in Figure 4.23. Ten layers of cells grow in the normal direction to form the VISVE grid, as shown in Figure 4.24.

Both simulations with and without viscosity were carried out. The Reynolds number in the viscous case was specified to be 5×10^4, where the length scale is the chord length at the mid-span section. Although the method is formulated to be unsteady, the results of the simulation tended to reach the steady state. The predicted tip flows in both viscous and inviscid cases are shown in Figure 4.25. The inviscid results show clear LEV and rolled-up tip vortex, whereas the presence of viscosity suppressed the formation of the LEV and tip vortex. Figure 4.26 show a side view of the y-vorticity contours in both cases. Again viscosity leads to more attached flow as well as a thick boundary layer which has a strong tendency to leave the wall in the suction side of the wing.

The preliminary results on modelling the tip flow of the 3D swept wing using the VISVE method are promising. A Navier-Stokes simulation of the viscous case was also carried out in order to validate the proposed method. The number of cells in the N-S simulation was about 700,000, which is 30

times of the number of cells in the VISVE model. Correlation between the results from both methods was made at a certain time instance, as shown in Figure 4.27. Great similarities can be observed between both methods, although the resolution in the VISVE model is coarser than that in the N-S simulation.

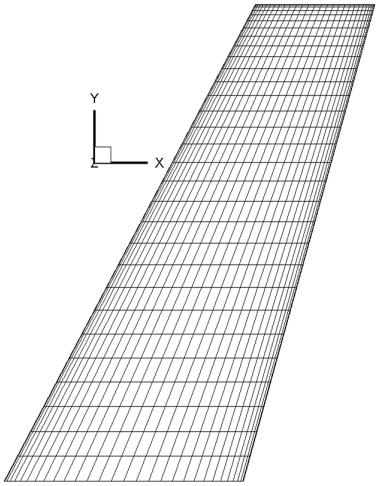

Figure 4.23: Planform and the BEM panels on the swept wing.

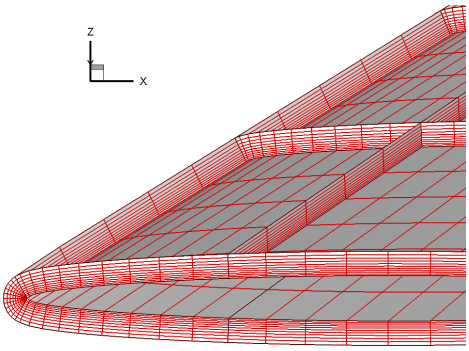

Figure 4.24: VISVE cells based on the BEM panels of the swept wing.

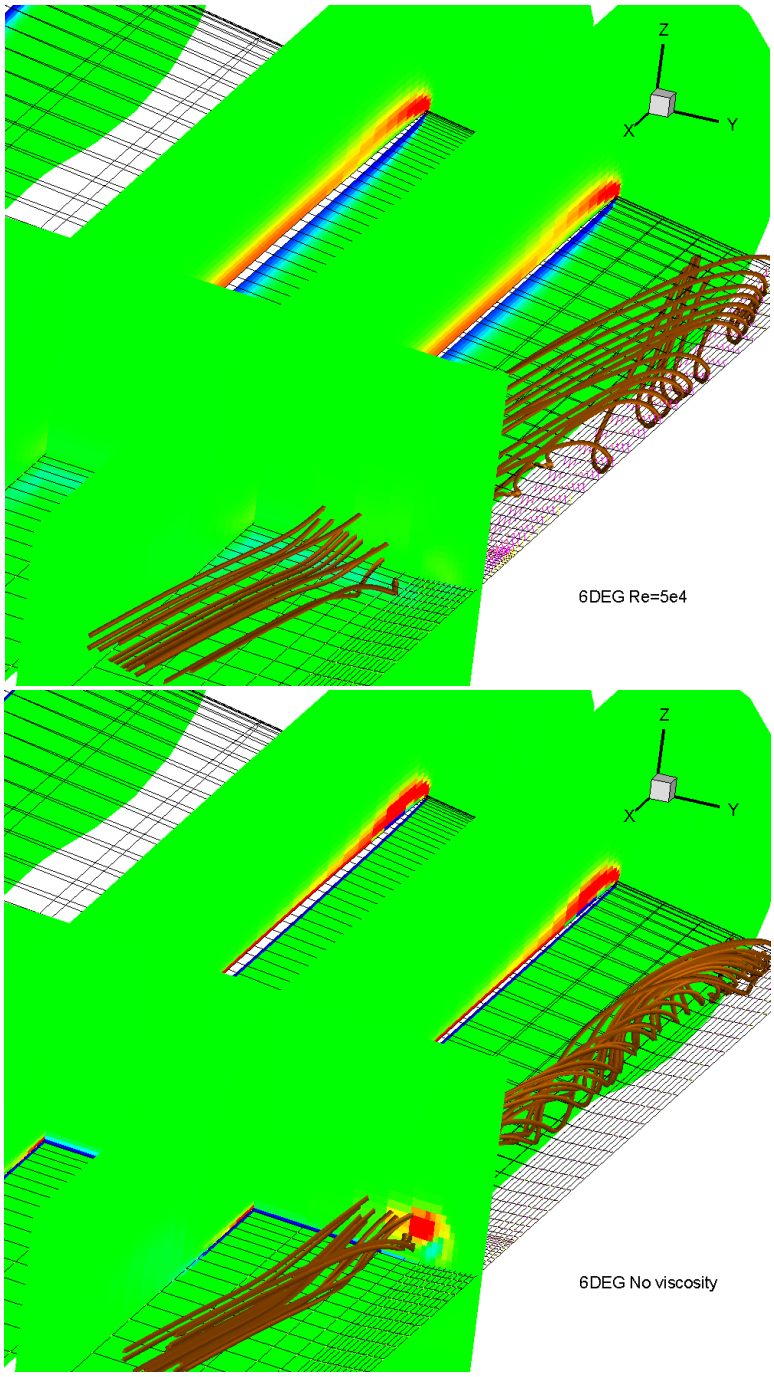

Figure 4.25: Predicted tip flow in the case of a 3D swept wing at 6 Degree AOA. Top: with viscosity; Bottom: w/o viscosity

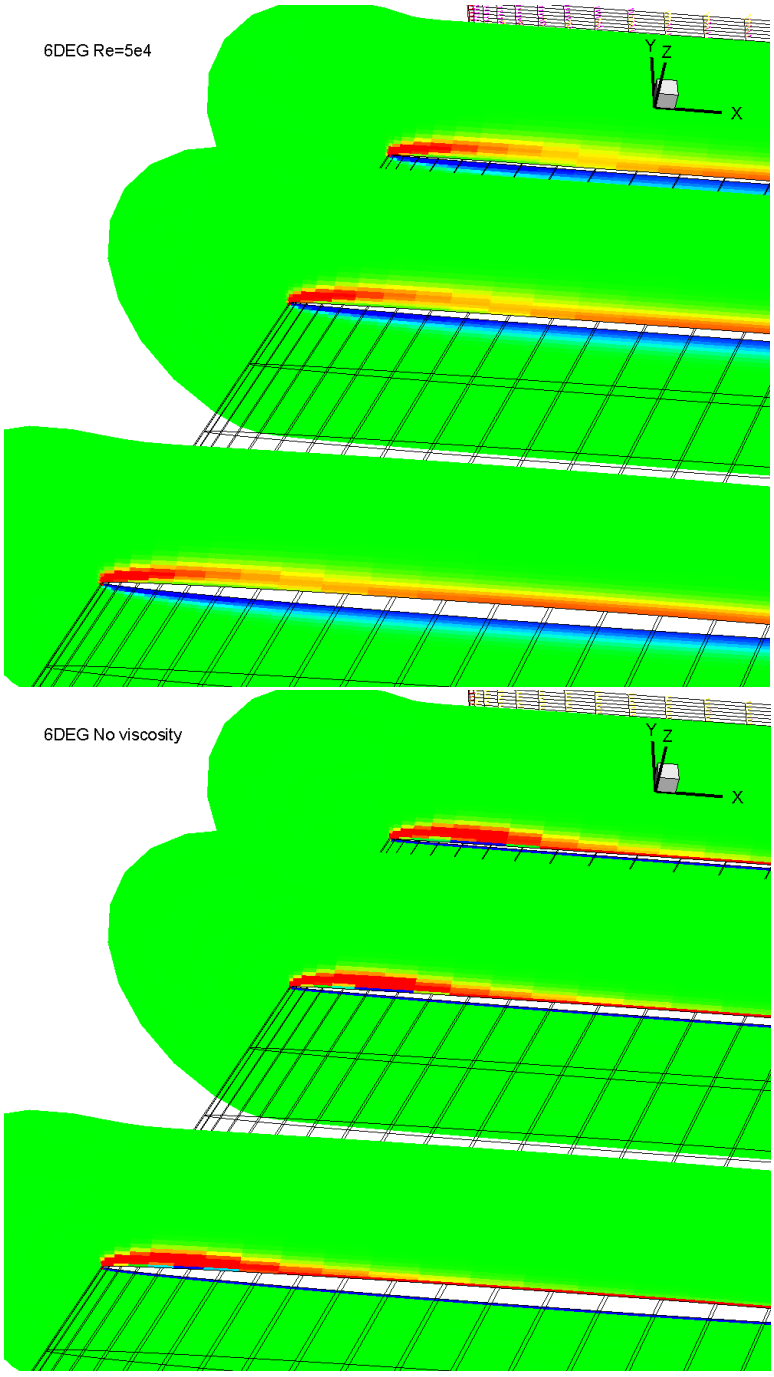

Figure 4.26: Side view of the predicted y-voriticy contour in the case of a 3D swept wing at 6 Degree AOA. Top: with viscosity; Bottom: w/o viscosity

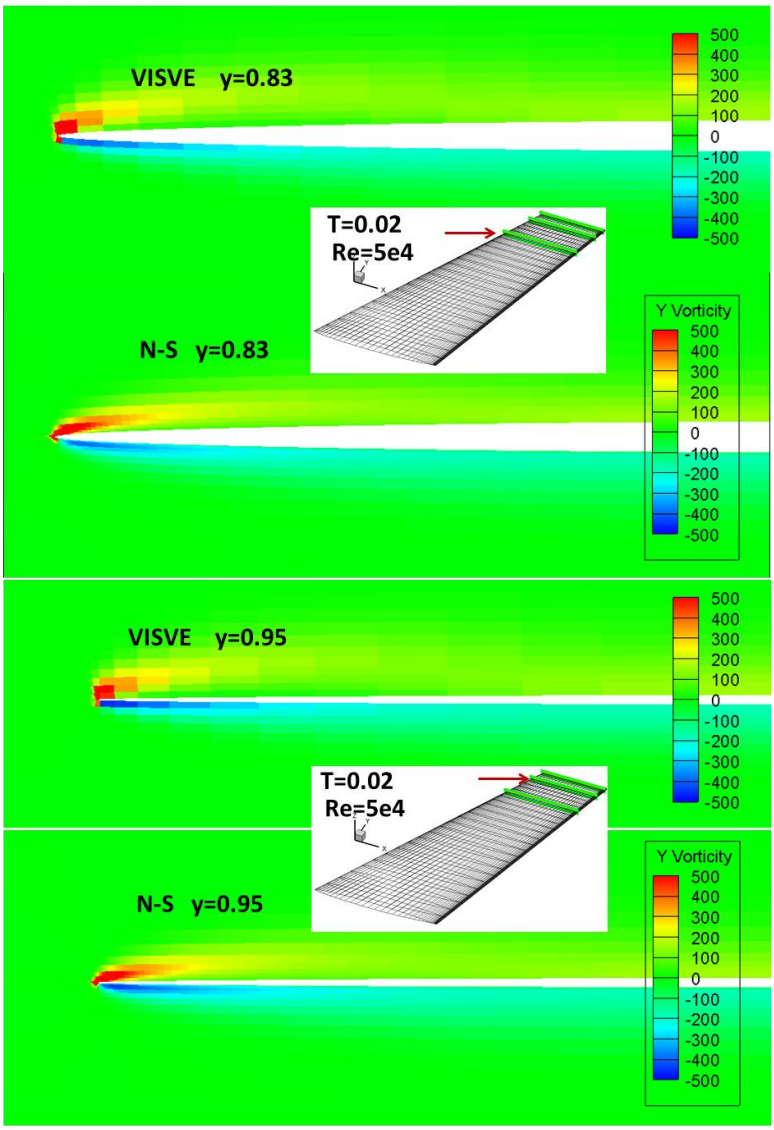

Figure 4.27: Correlation of the y-vorticity at two sections close to the tip in the case of a 3D swept wing at 6 Degree AOA. Top: $y = 0.83$span; Bottom: $y = 0.95$ span

4.5.12 Application: a propeller at high loading

The method is eventually applied in the case of a model propeller at high loading. As a preliminary test, the propeller only has one blade. The pitch and thickness of the blade are the same as those of a 5 bladed propeller NSRCD 4381 (Boswell 197[2]). The design advance ratio of NSRCD 4381 is 0.889. The geometric data of the model propeller in our simulation is shown in Appendix B. Two advance ratios $J = 0.6$ and $J = 0.3$ are investigated.

Figure 4.28 shows the computational grid. On the blade 80×25 (chord-wise×span-wise) panels are used, and 20 layers of cells grow in the normal direction. The VISVE wake region has 20 layers of cells, and the region beyond the tip has 10 layers of cells. In total about 84,000 cells are used to discretize the computational domain.

In the $J = 0.6$ case, the time step size Δt is specified as $0.001[\mathrm{R}/\mathrm{U}_\infty]$, which is about 10 times of the time step from the CFL condition. Clearly the backward Euler scheme greatly improves the numerical stability of the method. The Reynolds number based on the propeller diameter D and the inflow, $Re_D = 2 \times 10^6$. Figure 4.29 shows the predicted vorticity distribution around the propeller. Both the tip vortex and the leading edge vortex are captured by the method. Figure 4.30 – 4.40 show a series vorticity distributions at the 20th, 40th, 60th, 80th, 100th and 120th time step.

Simulation for the same operating condition ($J = 0.6$) is also performed using a denser grid on the blade (100×30 panels), and smaller time

step size ($\Delta t = 0.0008[\mathrm{R/U}_\infty]$), the predicted vorticity distributions at $t = 0.02, 0.06, 0.08, 0.10, 0.12[R/U_\infty]$ are also shown in Figure 4.31– 4.41.

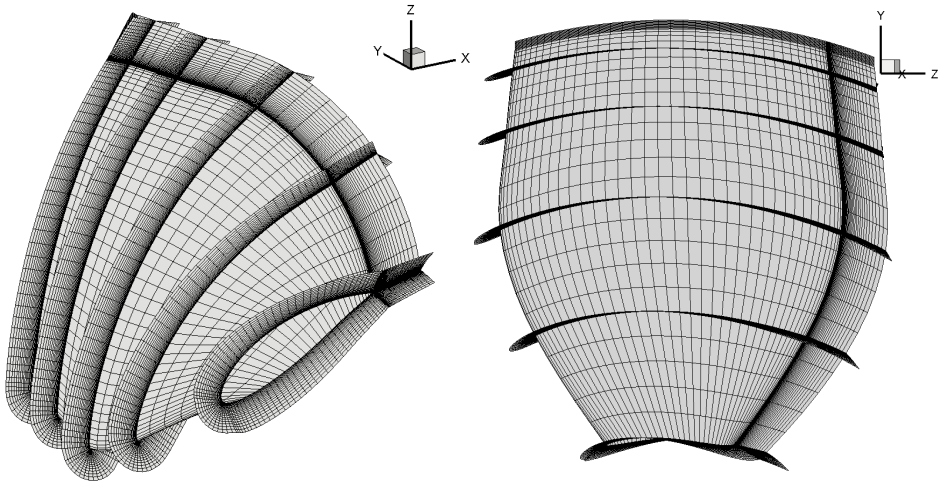

Figure 4.28: Computational grid in the case of a propeller at high loadings.

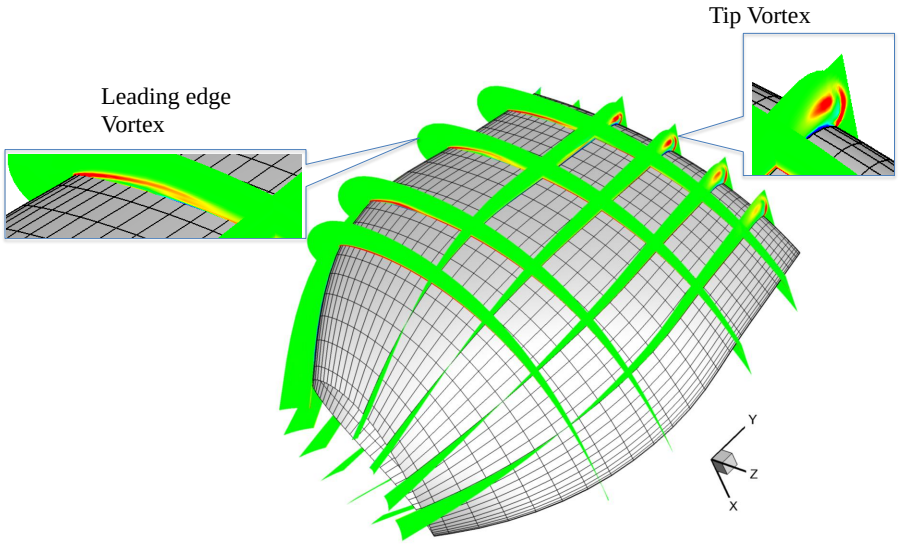

Figure 4.29: Predicted vorticity distribution around the propeller, $t = 0.12[\mathrm{R}/\mathrm{U}_\infty]$.

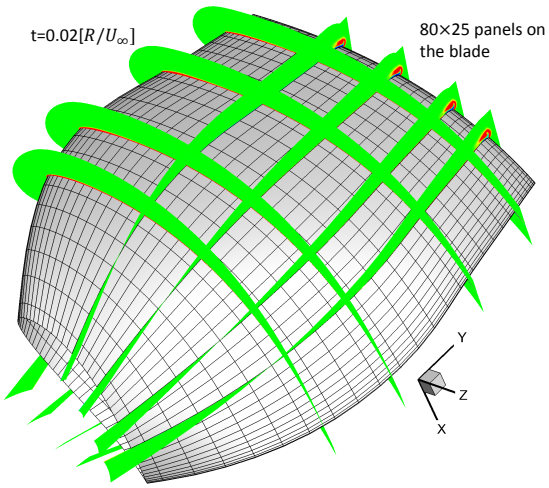

Figure 4.30: Temporal evolution of the vorticity around the propeller blade, $J = 0.6$, $t = 0.02$[R/U$_\infty$], 80×25 panels on the blade.

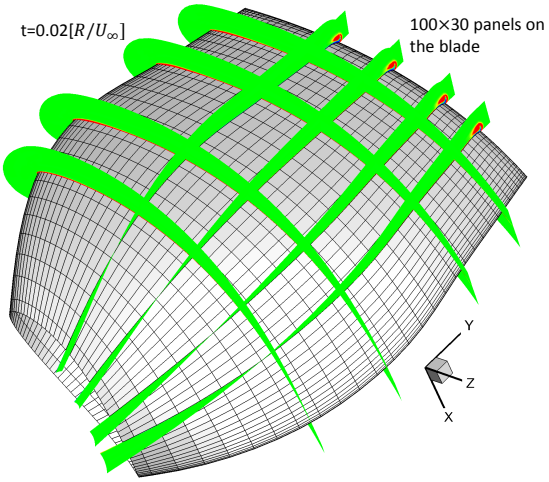

Figure 4.31: Temporal evolution of the vorticity around the propeller blade, $J = 0.6$, $t = 0.02$[R/U$_\infty$], 100×30 panels on the blade.

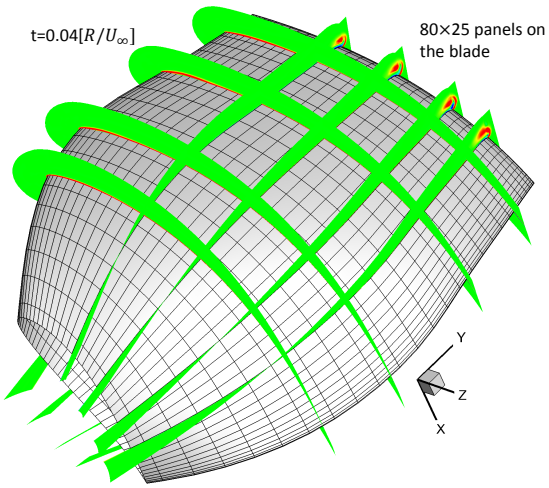

Figure 4.32: Temporal evolution of the vorticity around the propeller blade, $J = 0.6$, $t = 0.04$[R/U$_\infty$], 80×25 panels on the blade.

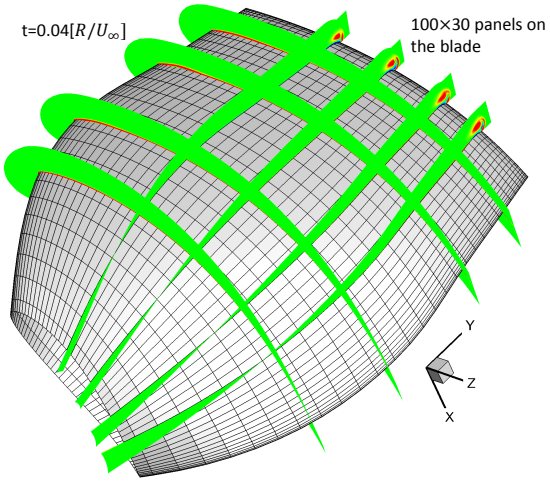

Figure 4.33: Temporal evolution of the vorticity around the propeller blade, $J = 0.6$, $t = 0.04$[R/U$_\infty$], 100×30 panels on the blade.

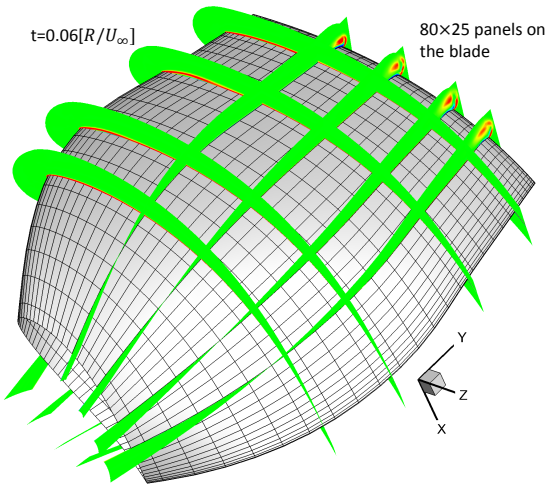

Figure 4.34: Temporal evolution of the vorticity around the propeller blade, $J = 0.6$, $t = 0.06$[R/U$_\infty$], 80×25 panels on the blade.

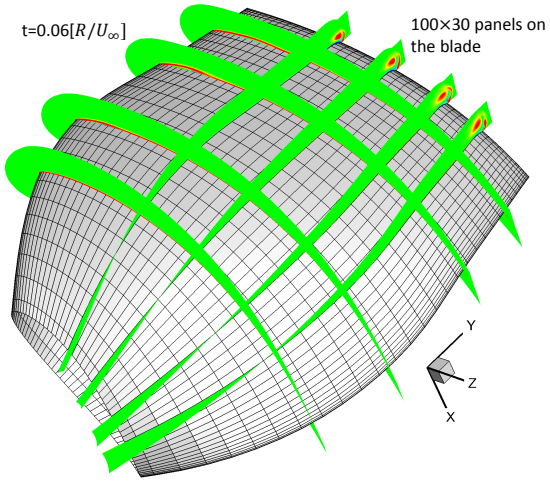

Figure 4.35: Temporal evolution of the vorticity around the propeller blade, $J = 0.6$, $t = 0.06$[R/U$_\infty$], 100×30 panels on the blade.

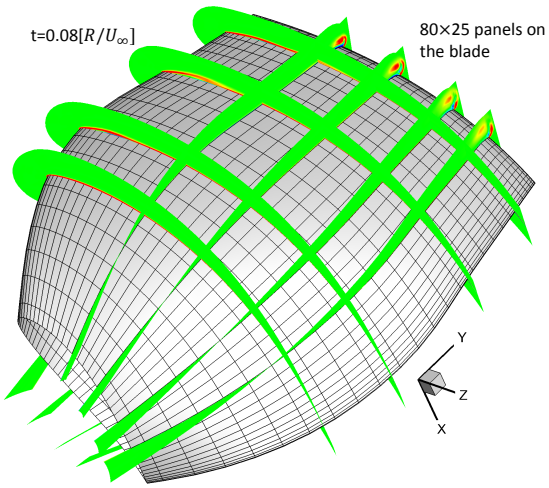

Figure 4.36: Temporal evolution of the vorticity around the propeller blade, $J = 0.6$, $t = 0.08$[R/U$_\infty$], 80×25 panels on the blade.

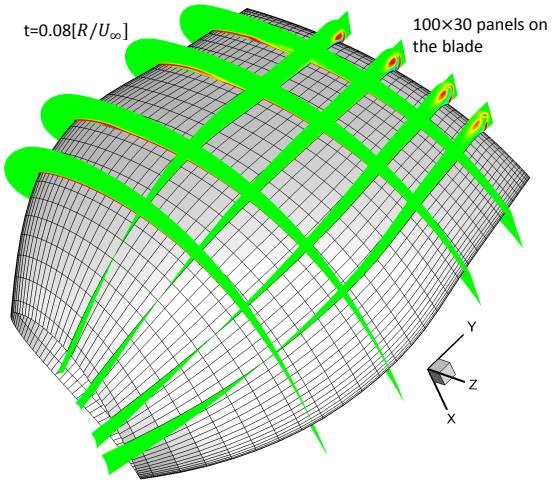

Figure 4.37: Temporal evolution of the vorticity around the propeller blade, $J = 0.6$, $t = 0.08$[R/U$_\infty$], 100×30 panels on the blade.

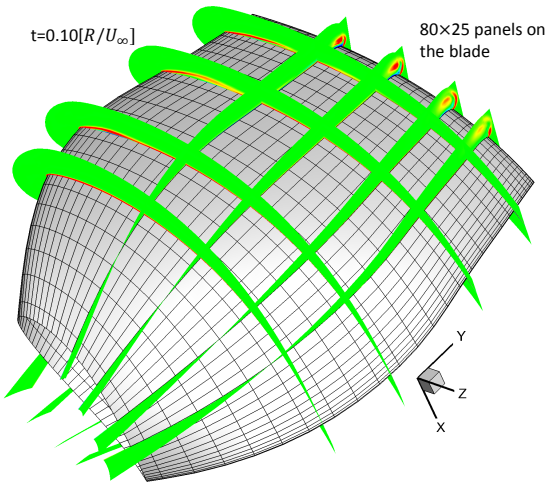

Figure 4.38: Temporal evolution of the vorticity around the propeller blade, $J = 0.6$, $t = 0.10$[R/U$_\infty$], 80×25 panels on the blade.

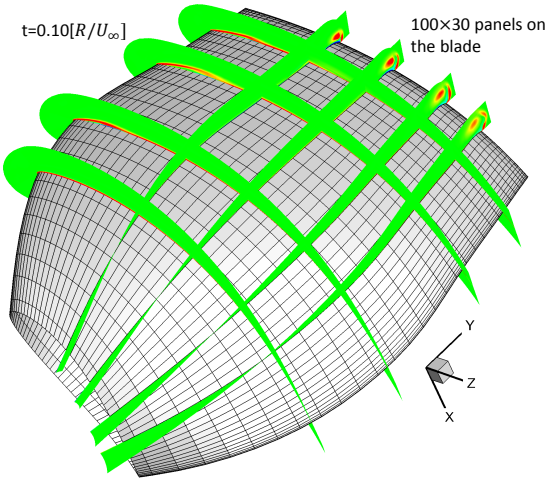

Figure 4.39: Temporal evolution of the vorticity around the propeller blade, $J = 0.6$, $t = 0.10$[R/U$_\infty$], 100×30 panels on the blade.

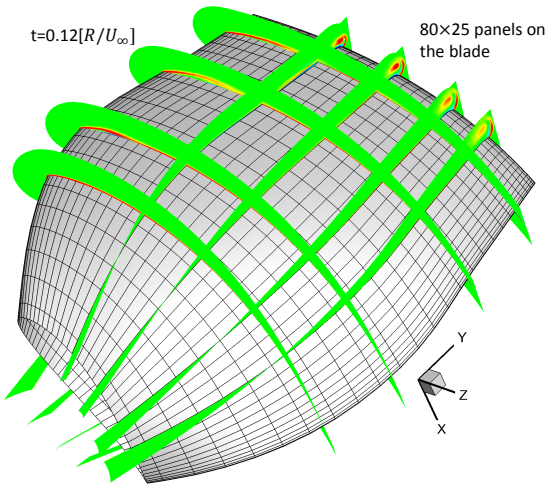

Figure 4.40: Temporal evolution of the vorticity around the propeller blade, $J = 0.6$, $t = 0.12$[R/U$_\infty$], 80×25 panels on the blade.

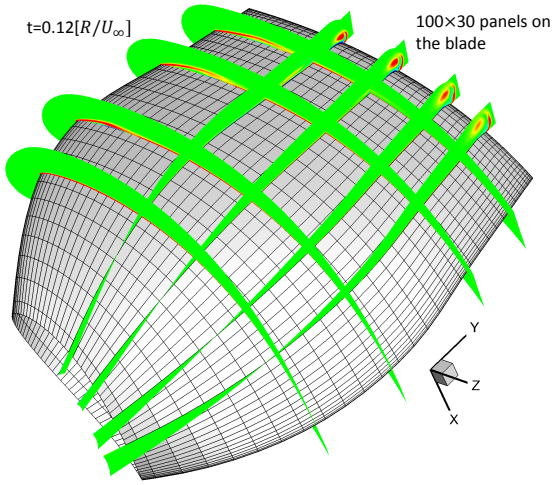

Figure 4.41: Temporal evolution of the vorticity around the propeller blade, $J = 0.6$, $t = 0.12$[R/U$_\infty$], 100×30 panels on the blade.

Figure 4.42 – 4.44 show the effect of the LEV on the pressure distribution. As expected, the LEV creates a low pressure plateau close to the leading edge. Conceivably the total torque and thrust with the LEV are increased, as shown in Table 4.2.

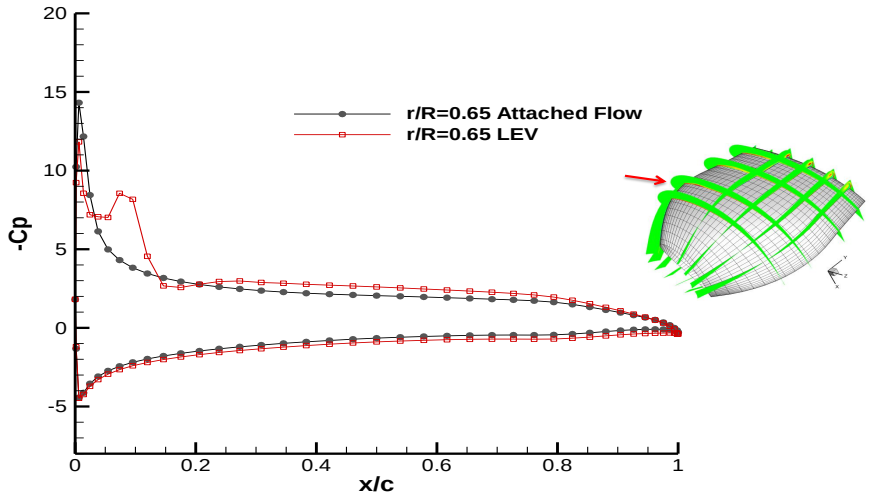

Figure 4.42: Effect of the LEV on the pressure distribution, $J = 0.6$, $r/R = 0.65$, $C_p = \frac{P-P_0}{0.5\rho n^2 D^2}$.

Table 4.2: Predicted thrust and torque coefficients (KT and KQ) with and without the LEV.

	Attached Flow	With LEV	Change in %
KT	0.167	0.2	+19%
KQ	0.0289	0.0341	+18%

The flow around the propeller at an extremely high loading condi-

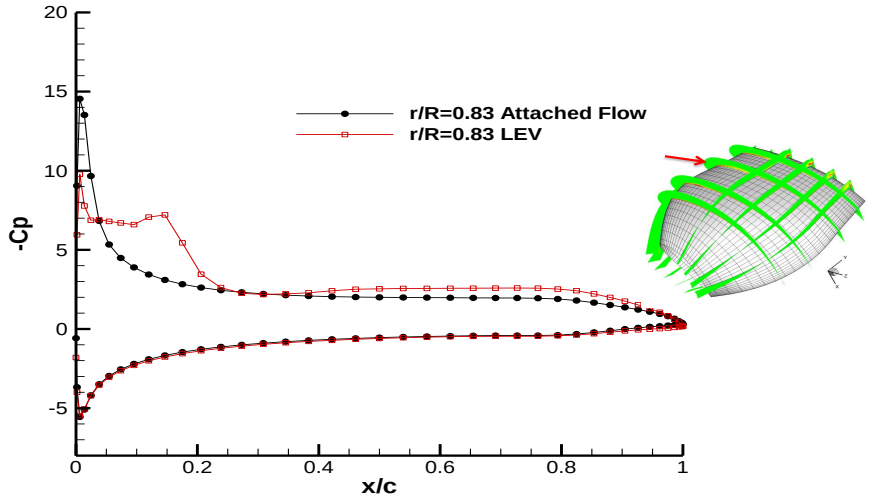

Figure 4.43: Effect of the LEV on the pressure distribution, $J = 0.6$, $r/R = 0.83$, $C_p = \frac{P-P_0}{0.5\rho n^2 D^2}$.

tion: $J = 0.3$, is also investigated. In this case the time step size $\Delta t = 0.0005[\mathrm{R/U_\infty}]$, because the rotational speed of the propeller is twice of that at $J = 0.6$. A slightly bigger computational domain, which has 25 layers of cells in the normal direction is adopted, since the tip vortex at $J = 0.3$ is larger than that at $J = 0.6$. Figure 4.45 shows the LEV and the tip vortex at the 150th time step from different perspectives. Clearly the LEV becomes more three-dimensional — it has strong components not only in the spanwise cutting sections, but also in the chordwise cutting sections.

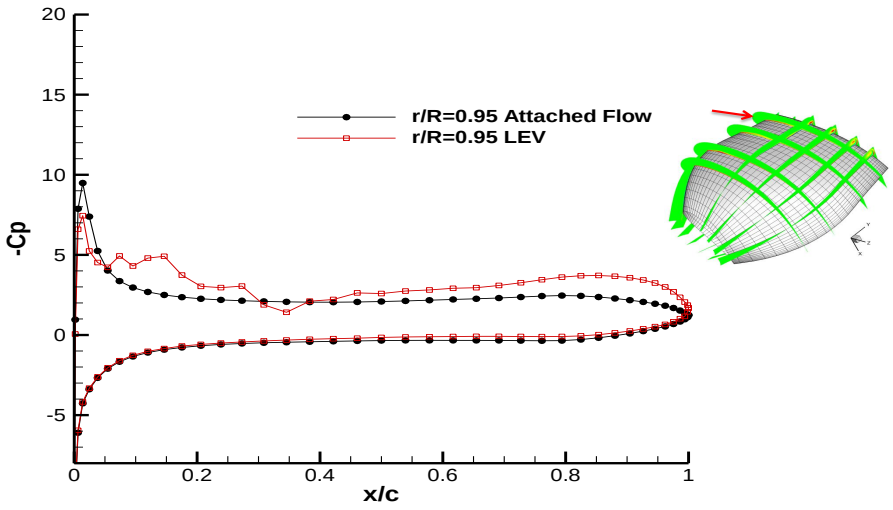

Figure 4.44: Effect of the LEV on the pressure distribution, $J = 0.6$, $r/R = 0.95$, $C_p = \frac{P-P_0}{0.5\rho n^2 D^2}$.

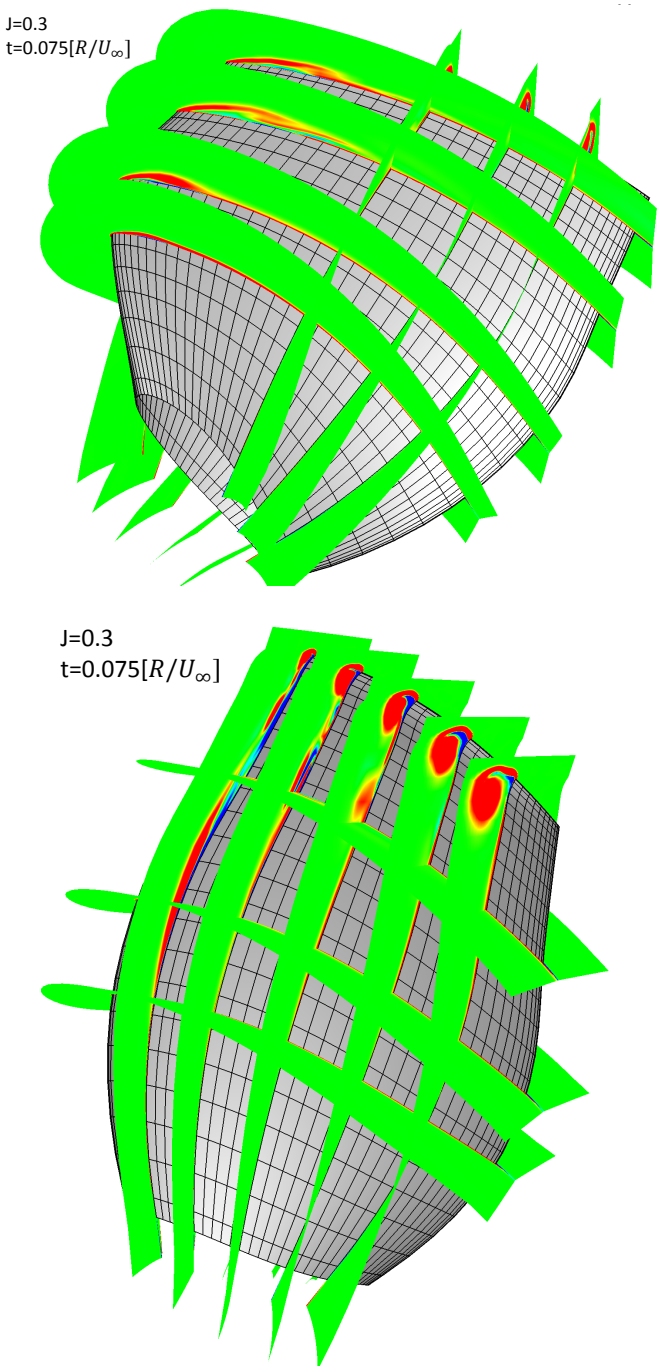

Figure 4.45: Predicted vorticity around the propeller blade, shown from different perspectives, $J = 0.3$, $t = 0.075[\mathrm{R/U_\infty}]$.

Chapter 5

Conclusions and Recommendations

5.1 Conclusions and Contributions

In this dissertation, different numerical methods for modelling the Leading Edge Vortex (LEV) and its effect on propeller performance were proposed and implemented.

The distinct thin shear layer LEV model was presented first. In 2D, the model functions reasonably well on simulating the inviscid behavior of the LEV of a biconvex foil with sharp leading edge. The 3D extension of the model was applied to simulate the LEV of delta wings having sharp leading edges. With the pseudo-unsteady alignment scheme, the LEV model was able to capture the major flow characteristics including the roll-up of the LEV and the low pressure peak on the wing. But quantitative check on the pressure distributions indicated that there were missing physics in the model. Applications of the distinct thin shear layer model to simulate the trailing edge wakes of a propeller were considerably successful. The fully aligned wake significantly improved the predicted off-design performance of propellers. However, further modeling of the LEV shed from the propeller blade using the same method was not satisfactory.

The numerical difficulties of the thin LEV model were then analyzed. Realizing the drawbacks of the thin LEV model, a numerical method which solves the VIScous Vorticity Equation (VISVE) was proposed and developed. The spatial concentration of the vorticity is exploited in the method, which is designed to be spatially compact and numerically efficient, in the meantime, capable of modeling complicated vorticity/solid boundary interaction in 2D and 3D. Detailed solving techniques of the VISVE were discussed.

In 2D, the method was validated against a commercial NS solver in the case of a hydrofoil at high angle of attack. In 3D, preliminary validation of the VISVE method with the conventional NS solver was performed in the case of a thin swept wing at moderate angle of attack. Great similarities between the results from the VISVE and the N-S methods were observed in both 2D and 3D cases.

The VISVE method was eventually applied in the case of a model propeller at low advance ratios. The method was able to predict all the essential characteristics of the flow (Leading edge vortex, tip vortex). The low pressure plateau and the increased thrust and torque due to the presence of the LEV were well predicted.

The main contributions of the present work are:

1. A new general way to greatly extend the applicability of the traditional Boundary Element Method (BEM), which is usually considered to be only useful for inviscid fluid flow. Via the VISVE method, BEM can

handle viscous, separated flow.

2. The vorticity equation was often used in 2D, but rarely found in 3D applications for complex geometries. Several new numerical techniques were developed on solving the 3D vorticity equation. The solving algorithm of the VISVE was carefully designed to ensure the divergence free of the vorticity field. An implicit time marching scheme was also constructed. The scheme not only greatly improves the numerical stability of the method, but more important, is fully parallelizable.

3. The VISVE method takes advantage of the spatial concentration of the vorticity. With a much smaller computational domain, the VISVE method is more computationally efficient than Navier-Stokes Solvers. The author believes that the fully optimized VISVE solver can be routinely used in the design stage of propellers. The spatial compactness of the method also benefits the automation of the grid generation process, because meshing only the proximity of the body is much easier than meshing the whole, unbounded computational domain. The former merely requires normal extrusion of the surface panel on the body. The latter has to compromise more between the grid quality and the topological connectivity of cells.

4. The method is built on an existing BEM solver. With the help of the VISVE method, many problems even difficult for the full-blown RANS simulation, such as the bollard pull performance of propellers, now

become tangible for the old BEM code.

5.2 Recommendations for Future Work

As a prototype of the LEV model, the VISVE method presented in this dissertation is well-established for laminar flows. However, the follows may be included to improve the method and make it a practically useful tool.

5.2.1 Fast evaluation of the volume integral of the point source kernel and the Biot-Savart Kernal

Currently the bottleneck of the VISVE method is the inner and outer solution matching procedures. In order to calculate the free space velocity on the boundaries of the computational domain, volume integral with the point source kernal is performed. The computational complexity of this procedure is about $O(n^{5/3})$. The Fast Multipole Methods (FMM), introduced by Greengard and Rohklin (1987)[12] can significantly accelerate this type of integration to $O(n)$. The FMM is the foundation of modern vortex particle methods in 3D. When using FMM in 3D, a tree code (usually octree) must be developed to subdivide the computational domain hierarchically. Algorithms for both point source kernel $(1/r)$ and the Biot-Savart kernel $(\times\mathbf{r}/r^3)$ are available. The only problem is that these algorithms are mainly for box shaped domains. Voxelization, which can be quite costly, is usually needed to handle complex geometries. In order maximize the computational efficiency of the method, it is better to develop a tree code for body fitted domains.

5.2.2 Localization of the computational domain

The objective of the study in this dissertation is to construct a local model for the LEV. The current VISVE method, although has already reduced the computational domain significantly compared with the conventional N-S solver, still covers regions of attached flow, for example, the region underneath the pressure side of the blade and the region close to the hub. The computational grids in these regions are not necessary and can be removed from the computational domain. The influence from the wall contained in these regions to the LEV formation is merely potential, and can be absorbed to the Neumann boundary conditions of the velocity Poisson solver.

5.2.3 Effects of turbulence

The current VISVE method uses a constant kinematic viscosity. Thus the method is only applicable to laminar flows. At high Reynolds numbers, computational grids are usually way too coarse to resolve the small scale structures in the flow, therefore rapid oscillatory solutions could be developed. A Reynolds averaging, or a filtering of the flow field can effectively stabilize the solution and avoid spurious pressure distribution on the wall. The kinematic viscosity may be replace by an eddy viscosity so that some effects of turbulence can be included. The first try can be an algebraic eddy viscosity model (mixing length model, for instance), whose modeling coefficients can be calibrated with the results of RANS simulation. One may also start from scratch, perform Reynolds averaging on the VISVE. Conceivably, there are

going to be terms like $\overline{u_i\omega_j}$. In fact, the derivation of certain theories for turbulent flows (such as the Rapid Distortion Theory, See Pope 2000 [34]) make use of vorticity. A review of those theories may shed some light on making up a model for the $\overline{u_i\omega_j}$ terms.

5.2.4 On the robustness of the numerical code

The current numerical implementation of the VISVE method is finicky on the orthogonality of the grid. As mentioned in Section 4.5.6, the non-orthogonality of the grids is handled through the deferred-correction technique. However, for highly skewed cells, the matrix of the velocity Poisson solver may not be diagonal dominant. Thus the iterative treatment of the mixed derivatives due to the grid skewness may lead to divergence of the results. It may be worthwhile to include the grid skewness also into the LHS of the velocity Poisson's equation. This could improve the robustness of the numerical code.

5.2.5 Parallelization of the code

The VISVE method can be fully parallelized. Parallelization of the code can significantly shorten the computational time experienced by end-users.

Appendices

Appendix A

Free space stream function due to a cell with constant vorticity distribution

In the VISVE method, the free space stream function due to a cell with constant vorticity distribution is used to calculate the velocity flux across a cell face. This stream function is evaluated analytically in 2D, and approximately in 3D.

A.1 Free space stream function in 2D

Consider the polygonal cell shown in Figure A.1. The free space stream function due to the cell can be calculated through following integration:

$$\psi = -\frac{\omega}{2\pi} \iint_A \ln r \, \mathrm{d}A \tag{A.1}$$

where $r = \sqrt{x^2 + y^2}$. It is conventient to use the following relation:

$$\frac{1}{4} \nabla \cdot \left(x \ln r^2 - 1, y \ln r^2 - 1 \right) = \ln r \tag{A.2}$$

(A.1) can then be evaluated using the divergence theorem:

$$\psi = -\frac{\omega}{8\pi} \int_{\partial A} (x \ln r^2 - 1) \, \mathrm{d}y - (y \ln r^2 - 1) \, \mathrm{d}x \tag{A.3}$$

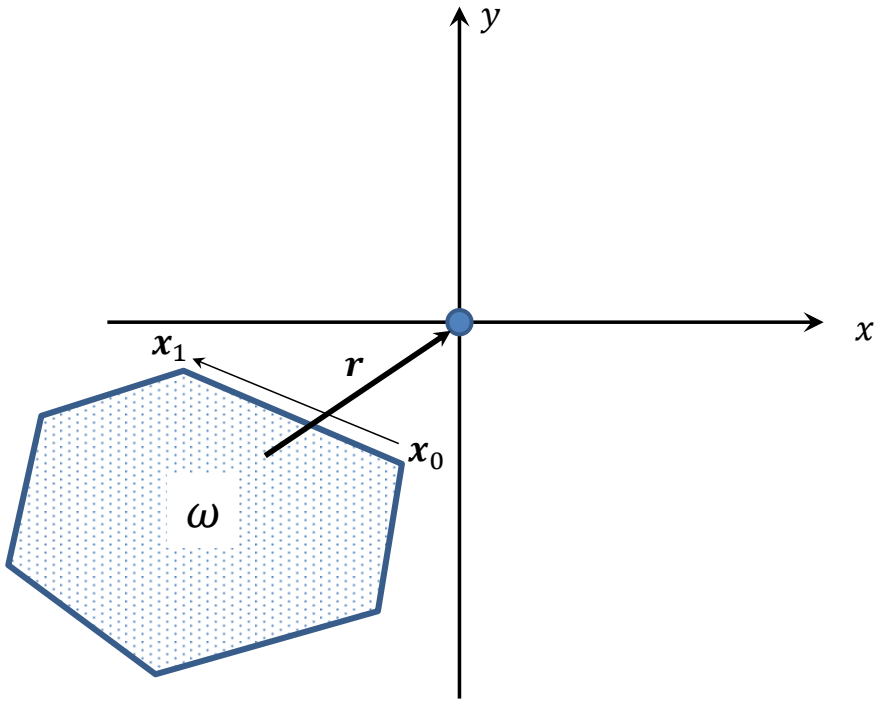

Figure A.1: Evaluation of the free space stream function due to a polygonal cell in 2D

Consider (A.3) along a straight line $\mathbf{x}_0 : (x_0, y_0)$-$\mathbf{x}_1 : (x_1, y_1)$,

$$\begin{aligned} x &= a_x s + x_0 \\ y &= a_y s + y_0 \end{aligned} \tag{A.4}$$

where

$$\begin{aligned} a_x &= \frac{x_1 - x_0}{\sqrt{(x_1 - x_0)^2 + (y_1 - y_0)^2}} \\ a_y &= \frac{y_1 - y_0}{\sqrt{(x_1 - x_0)^2 + (y_1 - y_0)^2}} \end{aligned} \tag{A.5}$$

Since

$$
\begin{aligned}
&\int_{\mathbf{x}_0}^{\mathbf{x}_1} (x \ln r^2 - 1)\,\mathrm{d}y - (y \ln r^2 - 1)\,\mathrm{d}x \\
=&\int_0^{s_{\max}} a_y(x \ln r^2 - 1) - a_x(y \ln r^2 - 1)\,\mathrm{d}s \\
=&\int_0^{s_{\max}} (a_y x - a_x y) \ln r^2 - a_y + a_x\,\mathrm{d}s \\
=&\int_0^{s_{\max}} (a_y x_0 - a_x y_0) \ln r^2 - (a_y - a_x)\,\mathrm{d}s \\
=&(a_y x_0 - a_x y_0)\Big[(-2s + 2(y_0 a_x - x_0 a_y) \arctan \frac{a_y x_0 - a_x y_0}{a_x x_0 + a_y y_0 + s} \\
&+ (a_x x_0 + a_y y_0 + s) \ln r^2\Big]_0^{s_{\max}} - (a_y - a_x) s_{\max}
\end{aligned}
\tag{A.6}
$$

Applying (A.6) over all the edges of a cell gives the value of ψ. Notice that the arctan function appears in (A.6), special care must be taken in order to select the correct solution branch of arctan.

A.2 Free space stream function in 3D

In 3D, the free space stream function due to the shown cell in Figure A.2 can be calculated through following volume integration:

$$\boldsymbol{\psi} = \frac{\boldsymbol{\omega}}{4\pi} \iiint_V 1/r\,\mathrm{d}V \tag{A.7}$$

The volume integration for a general hexahedral cell, however , is difficult to be evaluated analytically. In the VISVE method, the integration is calculated approximately using the induced potential due to a source panel, as shown in Figure A.2.

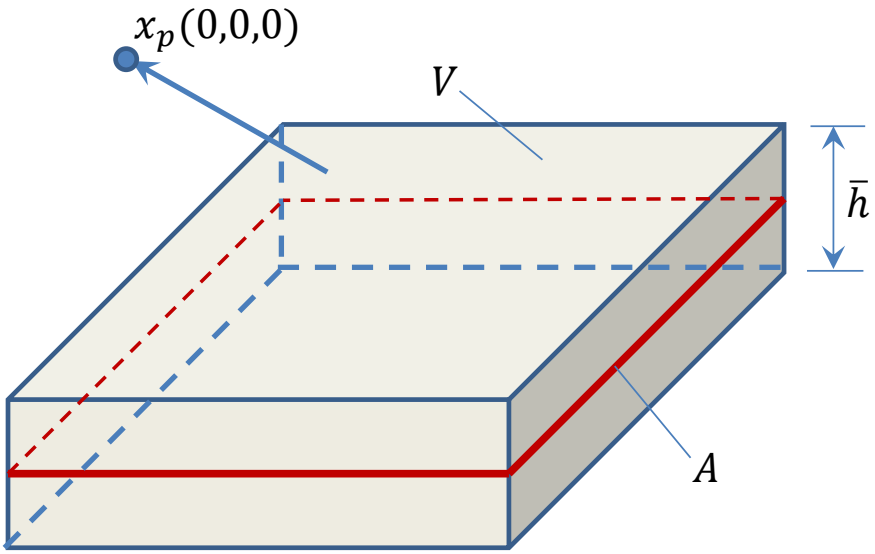

Figure A.2: Evaluation of the free space stream function due to a hexahedral cell in 3D.

The integral in (A.7) can be evaluated approximately as follows:

$$\iiint_V 1/r \, \mathrm{d}V \approx \bar{h} \iint_A \frac{1}{r} \, \mathrm{d}A \tag{A.8}$$

where $\bar{h} = V/A$ is the averaged height of the cell. The integratal in the RHS of (A.8) is the induced potential due to constant source distribution on A. The potential can be evaluated analytically, following the formula by Newman (1986)[29].

Appendix B

Propeller Geometry

This appendix contains the propeller geometry used in Section 4.5.12.

Table B.1: Geometry of the model propeller used in Section 4.5.12

Number of Blade(s)=1						
r/R	P/D	x_m/D	θ_m	C/D	f_{max}/C	t_{max}/D
0.2000	1.3100	0.0000	0.0000	0.1740	0.0352	0.0434
0.3000	1.3448	0.0000	0.0000	0.2290	0.0368	0.0358
0.4000	1.3580	0.0000	0.0000	0.2750	0.0348	0.0294
0.5000	1.3361	0.0000	0.0000	0.3120	0.0307	0.0240
0.6000	1.2797	0.0000	0.0000	0.3370	0.0245	0.0191
0.7000	1.2099	0.0000	0.0000	0.3470	0.0191	0.0146
0.8000	1.1366	0.0000	0.0000	0.3340	0.0148	0.0105
0.9000	1.0660	0.0000	0.0000	0.3210	0.0123	0.0067
0.9544	1.0294	0.0000	0.0000	0.3139	0.0122	0.0048
0.9849	1.0096	0.0000	0.0000	0.3100	0.0126	0.0031
1.0000	1.0000	0.0000	0.0000	0.3080	0.0000	0.0000

Bibliography

[1] W. T. Ashurst and E. Meiburg. Three-dimensional shear layers via vortex dynamics. *Journal of Fluid Mechanics*, 189:87–116, 1988.

[2] R.J. Boswell. *Design, Cavitation Performance, and Open-Water Performance of A Series of Research Skewed Propellers.* Naval Ship Research and Development Center. Department of the Navy, 1971.

[3] A. J. Chorin and P.S. Bernard. Discretization of a vortex sheet with an example of roll-up. *Journal of Computational Physics*, 13:423–429, 1973.

[4] R. Clements. An inviscid model of two-dimensional vortex shedding. *Journal of Fluid Mechanics*, 57:321–336, 1973.

[5] Weinan E and Jian-Guo Liu. Finite difference methods for 3d viscous incompressible flows in the vorticityvector potential formulation on non-staggered grids. *Journal of Computational Physics*, 138:57–82, 1997.

[6] A.M. Elshabka and T.J. Chung. Numerical solution of three-dimensional stream function vector components of vorticity transport equations. *Comput. Methods Appl. Mech. Engrg.*, 170:131–153, 1999.

[7] E. Erturk, T.C. Corke, and C. Gökçöl. Numerical solutions of 2-d steady incompressible driven cavity flow at high reynolds numbers. *International Journal for Numerical Methods in Fluids*, 48:747–774, 2005.

[8] J.H. Ferziger and Perić M. *Computational Methods for Fluid Dynamics*. Springer, 2002.

[9] R. Gordon and J. Rom. Calculation of non-linear subsonic characteristics of wings with thickness and camber at high incidence. *AIAA JOURNAL*, 23, No. 6:817–825, 1985.

[10] David S. Greeley. *Marine propeller blade tip flows*. PhD thesis, MIT, 1982.

[11] D.S. Greeley and J.E. Kerwin. Numerical methods for propeller design and analysis in steady flow. *Transactions of Society of Naval Architects & Marine Engineers*, 90:415C453, 1982.

[12] L. Greengard and V. Rohklin. A fast algorithm for particle simulations. *Journal of Computational Physics*, 73:325, 1987.

[13] M.O.L. Hansen, J.N. Sørensen, and W.Z. Shen. Vorticity-velocity formulation of the 3d navierstokes equations in cylindrical co-ordinates. *International Journal for Numerical Methods in Fluids*, 41:29–45, 2003.

[14] L. He. *Numerical Simulation of Unsteady Rotor/Stator Interaction and Application to Propeller/Rudder Combination*. PhD thesis, UT Austin, 2010.

[15] F. T. Johnson, P. Lu, and E. N. Tinoco. An improved panel method for the solution of three-dimensional leading-edge vortex flows. volume 1: Theory document. *NASA-CR-3278*, 1980.

[16] J. Katz. A discrete vortex method for the non-steady separated flow over an airfoil. *Journal of Fluid Mechanics*, 102:315–328, 1981.

[17] Omar M Knio and Ahmed F Ghoniem. Numerical study of a three-dimensional vortex method. *Journal of Computational Physics*, 86:75–106, 1990.

[18] P. Koumoutasakos and A. Leonard. High-resolution simulations of the flow around an impulsively started cylinder using vortex methods. *Journal of Fluid Mechanics*, 296:1–38, 1995.

[19] R. Krasny. Computation of vortex sheet roll-up in the trefftz plane. *Journal of Fluid Mechanics*, 184:123–155, 1987.

[20] R. Krasny. *Vortex Dynamics and Vortex Methods*, chapter Vortex Sheet Computations:Roll-Up, Wakes, Separation, pages 385–402. American Mathematical Society, 1991.

[21] H.S. Lee. *Modeling of unsteady wake alignment and developed tip vortex cavitation*. PhD thesis, UT Austin, 2002.

[22] H.S Lee and S. A. Kinnas. Application of boundary element method in the prediction of unsteady blade sheet and developed tip vortex cavitation on marine propellers. *Journal of Ship Research*, 48(1):14–30, 2004.

[23] A. Leonard. Vortex methods for flow simulation. *Journal of Computational Physics*, 37:289–335, 1980.

[24] A. Leonard. Computing three-dimensional incompressible flows with vortex elements. *Annu. Rev. Fluid Mech.*, 17:523–559, 1985.

[25] B.P. Leonard. A stable and accurate convective modelling procedure based on quadratic upstream interpolation. *Computer Methods in Applied Mechanics and Engineering*, 19:59–98, 1979.

[26] R. I. Lewis. *Vortex Element Methods for Fluid Dynamic Analysis of Engineering System.* Cambridge Univ Press, 1991.

[27] K. Lindsay and R. Krasny. A particle method and adaptive treecode for vortex sheet motion in three-dimensional flow. *Journal of Computational Physics*, 172:879–907, 2001.

[28] D. C. Lo, K. Murugesan, and Young D. L. Numerical solution of three-dimensional velocityvorticity navierstokes equations by finite difference method. *International Journal for Numerical Methods in Fluids*, 47:1467–1487, 2005.

[29] J. N. NEWMAN. Distributions of sources and normal dipoles over a quadrilateral panel. *Journal of Engineering Mathematics*, 20(2):113–126, 1986.

[30] D.T. Mook O.A. Kandil and A.H. Nayfeh. Nonlinear predictiona of aerodynamics loads on lifting surfaces. *Journal of Aircraft*, 13, 1976.

[31] Y. Pan and S.A. Kinnas. A viscous/inviscid interactive approach for the prediction of performance of hydrofoils and propellers with non-zero trailing edge thickness. *Journal of Ship Research*, 55(1):45–63, 2011.

[32] D.W. Peaceman and H.H. Rachford Jr. he numerical solution of parabolic and elliptic differential equations. *Journal of the Society for Industrial and Applied Mathematics*, 3(1):28–41, 1955.

[33] P. Ploumhans, G. S. Winckelmans, J. K. Salmon, A. Leonard, and M. S. Warren. Vortex methods for direct numerical simulation of three-dimensional bluff body flows: Application to the sphere at re = 300, 500, and 1000. *Journal of Computational Physics*, 178:427–463, 2002.

[34] S. Pope. *Turbulent Flows*. Cambridge University Press, 2000.

[35] W.D. Ramsey. *Boundary integral methods for lifting bodies with vortex wakes*. PhD thesis, Massachusetts Institute of Technology, 1996.

[36] T Sarpkaya. An inviscid model of two-dimensional vortex shedding for transient and asymptotically steady separated flow over an inclined plate. *Journal of Fluid Mechanics*, 68:109–128, 1975.

[37] S. Singh. Viscous/inviscid flow around 2-d and 3-d hydrofoils with emphasis on leading edge flow separation. Master's thesis, UT Austin, 2009.

[38] P. R. Spalart and A. Leonard. Computation of separated flows by a vortex tracing algorithm. In *AIAA 14th Fluid and Plasma Dynamics Conference.*, Palo Alto, CA., 1981.

[39] A. Thom. Flow past circular cylinders at low speeds. *Proc. R. Soc. London Ser. A*, 141:651–669, 1933.

[40] Ye Tian and S.A. Kinnas. Modeling of leading edge vortex and its effects on propeller performance. In *Second International Symposium on Marine Propulsors*, 2011.

[41] Ye Tian and Spyros. A. Kinnas. A wake model for the prediction of propeller performance at low advance ratios. *International Journal of Rotating Machinery*, 2012.

[42] M. Van Dyke. *An Album of Fluid Motion.* Parabolic Press, Inc., 1982.

[43] Frank M. White. *Viscous Fluid Flow, 3rd Edition.* Mc Craw-Hill, 2006.

[44] G.S. Winckelmans and A. Leonard. Contributions to vortex particle methods for the computation of three-dimensional incompressible unsteady flows. *Journal of Computational Physics*, 109:247–273, 1993.

[45] P.L. Woodfield, K. Suzuki, and K. Nakabe. A simple strategy for constructing bounded convection schemes for unstructured grids. *International Journal for Numerical Methods in Fluids*, 46:1007–1024, 2004.

[46] X.H. Wu, J.Z. Wu, and J.M. Wu. Effective vorticity-velocity formulations for the three-dimensional incompressible viscous flows. *Journal of Computational Physics*, 122:68–82, 1995.